UiT
THE ARCTIC UNIVERSITY OF NORWAY

Faculty of Science and Technology
Department of Physics and Technology

Spatial extent of solar proton impact in the Earth's atmosphere

Observations and modeling

—

Erkka Heino

A dissertation for the degree of Philosophiae Doctor – October 2019

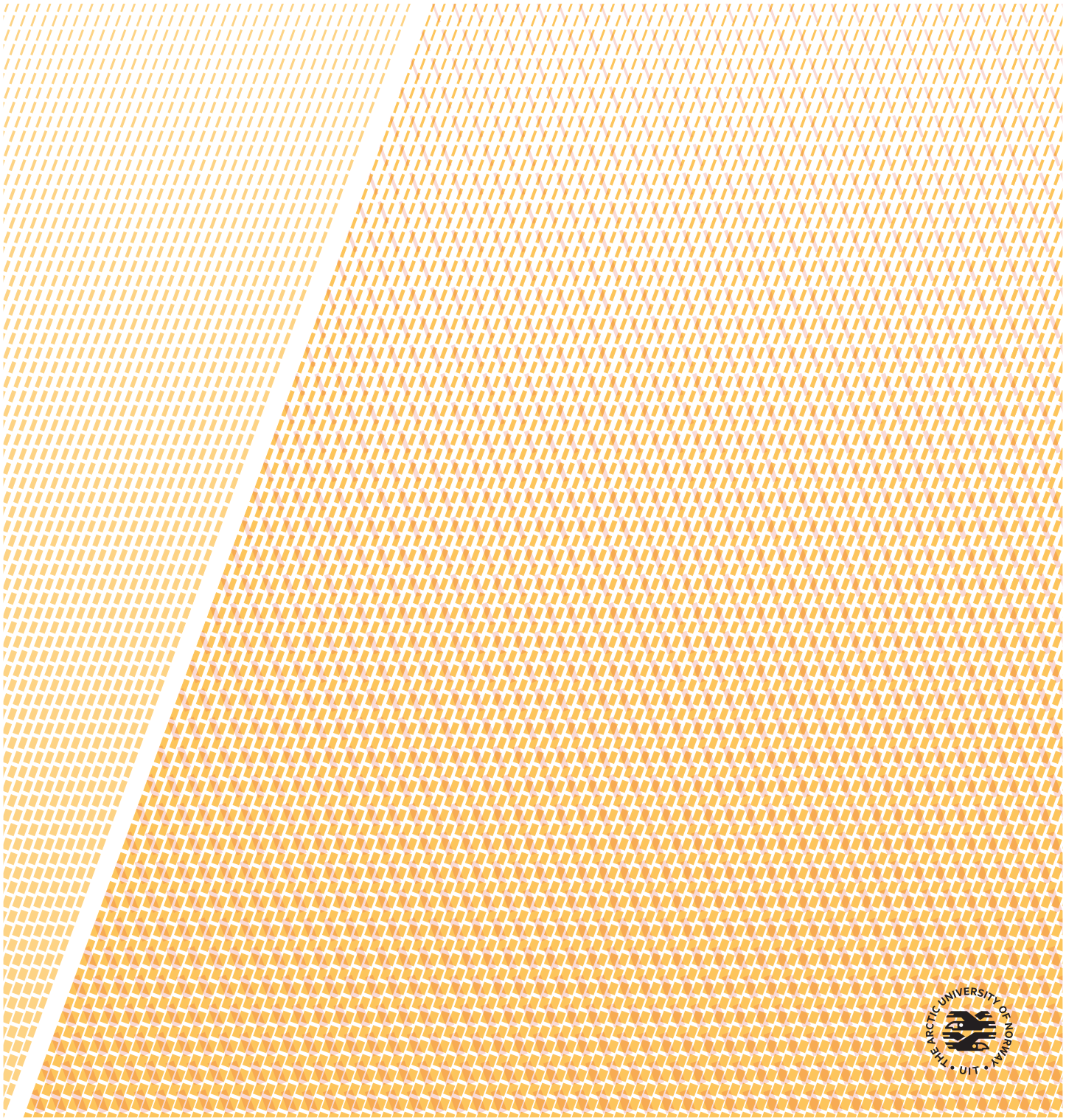

Spatial extent of solar proton impact in the Earth's atmosphere – Observations and modeling

Erkka Heino

A dissertation for the degree of Philosophiae Doctor

Department of Physics and Technology,

Faculty of Science and Technology,

University of Tromsø – The Arctic University of Norway

in cooperation with

UNIS

The University Centre in Svalbard

Department of Arctic Geophysics,

The University Centre in Svalbard

October 2019

Abstract

Solar proton events cause large-scale ionization in the Earth's middle atmosphere leading to chemical changes, changes in the energy budget of the middle atmosphere, and radio wave absorption. The accurate implementation of the spatial impact of solar protons and other particle ionization sources in climate models is necessary to understand the role of energetic particle precipitation in natural climate variability. The access of solar energetic particles into the Earth's atmosphere is limited in geomagnetic latitude by the particles' rigidity, the varying conditions of the interplanetary magnetic field and the solar wind, and the distortion of the Earth's magnetic field. The lowest geomagnetic latitude a particle of a given rigidity can access is the cutoff latitude for that rigidity. Proton precipitation in climate models is typically implemented as uniform precipitation poleward of a static latitude limit and cutoff latitudes are not included.

The spatial impact of solar proton events in the Earth's atmosphere is studied in this thesis by comparing the results of a chemistry-climate model to observations of cosmic noise absorption (CNA), testing two cutoff latitude models with CNA observations and modeled CNA, and employing a new approach of using routine background radio noise measurements from ionospheric high frequency radars. A correction method for the nonlinearity of riometers to high levels of CNA is also presented.

Based on the research presented in this thesis, the current proton forcing in climate models significantly overestimates the impact area of solar proton events. The implementation of a cutoff latitude model into the proton forcing is therefore recommended for future studies of solar proton event impact on the atmosphere and natural climate variability.

Contents

"I'm being quoted to introduce something, but I have no idea what it is and certainly don't endorse it."

Randall Munroe

Preface

This dissertation is submitted in partial fulfillment of the requirements for the degree of Philosophiae Doctor (PhD) in Science at the University of Tromsø – The Arctic University of Norway (UiT). The work and research presented in this thesis were conducted at the University Centre in Svalbard (UNIS), and funded by UNIS, the Academy of Finland (project 276926), and the Research Council of Norway (project 287427). The three year project was supervised by Associate Professor Noora Partamies (UNIS), Associate Professor Lisa Baddeley (UNIS), and Professor Chris Hall (UiT/Tromsø Geophysical Observatory). As a part of the requirements for the degree, I have completed course work at UNIS, UiT, the University of Bergen, and the University of Oslo. Parts of the results presented in this thesis have been presented in international conferences and workshops. In addition to research presented in the thesis, I have contributed to two other published articles as a co-author during the PhD project.

I am pleased to acknowledge everyone who supported this PhD project and helped me through it. First and foremost, I would like to thank my supervisors Noora, Lisa, and Chris for their guidance and support. Thank you, Noora, for guiding me through this project and being always available for questions and discussions. Thank you, Lisa, for your advice and quality coffee corner banter. Sorry for veering off the EISCAT path. Thank you, Chris, for your enthusiasm for my research and your lightning fast responses whenever I've had questions. I am very happy that I had you as my supervisors.

I would also like to thank UNIS, the Research Council of Norway, and the Academy of Finland for funding my PhD position. I thank my co-authors for their hard work, and my fellow members of the CHAMOS collaboration for interesting and inspiring research discussions. I would like to acknowledge the editors and reviewers of my publications for their work and helpful suggestions. I also acknowledge the data providers, whose data made this project possible.

I thank my past and present co-workers at UNIS for making this a great place to work at. I am especially grateful for my fellow staff at the Department of Arctic Geophysics. Thank you for your support and company during these three years. I am looking forward to sharing many more coffee breaks and work days with you.

I am grateful for my friends in Finland, Longyearbyen, and all over the world. Thank you for sharing your lives with me. I would especially like to thank the boys of Tukikohta and Turun lauantai. Kiitti, poja!

I thank my family for their love, support, and encouragement through the years. Thank you for encouraging me to find my own path and supporting me along the way.

Finally, a special thanks to P. Jeg er glad i deg.

Erkka Heino

Longyearbyen, October 2019

List of publications

This doctoral thesis consists of the introduction to the subject matter and the following peer-reviewed or submitted scientific articles:

I Bland, E. C., **Heino, E.**, Kosch, M. J., & Partamies, N. (2018). SuperDARN radar-derived HF radio attenuation during the September 2017 solar proton events. *Space Weather*, 16(10), 1,455–1,469. https://doi.org/10.1029/2018SW001916

II **Heino, E.**, Verronen, P. T., Kero, A., Kalakoski, N., & Partamies, N. (2019). Cosmic noise absorption during solar proton events in WACCM-D and riometer observations. *Journal of Geophysical Research: Space Physics*, 124(2), 1,361–1,376. https://doi.org/10.1029/2018JA026192

III **Heino, E.** and Partamies, N. Observational validation of cutoff models as boundaries of solar proton event impact area. *Under review in Journal of Geophysical Research: Space Physics*

The publications are referred to by their Roman numerals in the rest of the thesis.

E.H. contributed to the initial concept of Paper I, ran supplementary simulations, advised on topics related to riometry and QDC determination, took part in discussions regarding radio wave attenuation and HF noise, and commented on the initial draft and all revisions.
E.H. performed all data analyses and wrote Papers II and III. The initial concept for Paper II was formed in collaboration with P.T.V. and N.P., and the initial concept for Paper III was formed in collaboration with N.P.

1

Introduction

High-energy particles, mostly protons and electrons, are emitted from the Sun during solar proton events (SPEs). Particles that have entered the Earth's magnetosphere are partially guided by the Earth's magnetic field, and some of them are able to access the atmosphere. Due to the structure of the Earth's magnetic field, the particles cannot precipitate into the atmosphere uniformly, but are guided towards the polar regions.

A particle of a given rigidity can only precipitate to geomagnetic latitudes poleward of the particle's cutoff latitude. These cutoff latitudes are not static, or even uniform with magnetic local time (MLT), but move in geomagnetic latitude with the conditions of the interplanetary magnetic field (IMF) and the solar wind, the distortion of the Earth's magnetic field, and the intensities of magnetospheric currents. As the particles precipitate into the atmosphere, they collide with, and ionize, atmospheric gasses.

The increased ionization in the Earth's middle atmosphere leads to formation of odd hydrogen and odd nitrogen species, which are efficient in destroying ozone. As ozone has a major role in the heat balance of the middle atmosphere, changes in ozone concentrations lead to changes in the heating and cooling rates of the middle atmosphere. These changes can affect the dynamics of the middle atmosphere, which are in turn coupled to the dynamics of the troposphere. The effects of energetic particle precipitation (EPP) into the middle atmosphere can therefore propagate down into the troposphere and cause regional variations in ground-level air temperature and pressure. The role of EPP as a source of natural regional climate variability

has been recognized, but the the exact mechanisms of the EPP-climate coupling are not yet fully understood. In addition to SPEs, EPP also includes energetic electron precipitation (EEP), which can produce a similar effect in the Earth's atmosphere.

The increased ionization caused by SPEs can be observed indirectly from the ground by studying the increased absorption of radio waves that propagate through the Earth's lower ionosphere. Riometers are passive instruments that measure the level of cosmic radio noise continuously, and the amount of radio wave absorption is determined by calculating the difference between the measured noise power and the expected noise power without absorption. In the case of riometers, the level of radio wave absorption is called cosmic noise absorption (CNA). A similar approach to determine the level of absorption caused by SPEs can be used with other radio instruments as well, such as the Super Dual Auroral Radar Network (SuperDARN) radars.

Models of varying complexity are used to model both CNA and the atmospheric effects of EPP. CNA can be modeled by using an empirical relationship between CNA and particle flux, like in the case of the *D* Region Absorption Prediction (DRAP) model, or by calculating CNA from a modeled atmosphere. The atmosphere for the CNA calculation can be modeled with a chemistry-climate model, such as the Whole Atmosphere Community Climate Model with added *D* region ion chemistry (WACCM-D). Chemistry-climate models are also commonly used to model the effects of EPP on the atmosphere and the climate. In order to model either CNA or the atmospheric effects of EPP accurately, the spatial extent and fluxes of precipitating particles need to be implemented accurately.

The spatial extent of SPE impact in the Earth's atmosphere is studied in this thesis by using a combination of ground-based observations and modeling. The introductory part of this thesis consists of this introduction chapter followed by five chapters describing the necessary background for the three included publications and their results. The order of the chapters follows the same "source to effect" order as the beginning of this introduction. The results from the publications are presented among the relevant background information.

A short summary of the Earth's middle atmosphere and the ionospheric *D* region is given in Chapter 2. SPEs, the access of charged particles into the atmosphere, and the atmospheric effects of EPP are described in Chapter 3. Chapter 4 focuses on riome-

ters and SuperDARN radars, and how they are used to observe radio wave absorption. Modeling of the atmospheric effects of SPEs is discussed in Chapter 5, with a focus on CNA modeling. Spatial estimation of SPE impact based on modeling and observations, and the implementation of SPE forcing in chemistry-climate models are discussed in Section 5.2. Chapter 6 summarizes the results of the thesis and possible topics for future study.

Paper I presents a novel method for estimating high frequency (HF, 3–30 MHz) attenuation using SuperDARN background radio noise measurements and results of using this method for two SPEs in September 2017. The method and results of Paper I are described in Section 4.2. The spatial and temporal extent of CNA during 62 SPEs from 2000 to 2005 are studied in Paper II with the WACCM-D model and 16 riometers. The results are described in Section 5.1. A correction method for the non-linearity of riometers to high levels of CNA is also presented in Paper II and described briefly in Section 4.1. Two cutoff latitude models are compared in Paper III, using observations from 13 riometers and the DRAP model during 73 SPEs from 1997 to 2010. The average spatial extent of the SPE impact area is also estimated using one of the cutoff models. The results of the cutoff latitude model comparison are described in Sections 3.2 and 5.1, and the spatial extent estimation in Section 5.2.

2

Middle atmosphere and the D region ionosphere

Key features of the Earth's middle atmosphere and the innermost region of the Earth's ionosphere, the *D* region, are described in this chapter. These parts of the Earth's atmosphere and ionosphere provide the backdrop for the phenomena discussed in the rest of the thesis. The description of the middle atmosphere is based on *Brasseur and Solomon* (2006) and *Lilensten et al.* (2015, ch. 1.1).

2.1 Middle atmosphere

The Earth's atmosphere extends from the Earth's surface to approximately 500–1,000 km altitude, excluding the exosphere. The vertical structure of the atmosphere can be divided to layers in multiple ways depending on the approach taken. While pressure and density generally decrease in the atmosphere with altitude, temperature has a more complex behavior with altitude and serves as a useful way to distinguish between the different atmospheric layers. The temperature profile of the atmosphere during summer and winter, and the different atmospheric layers based on their thermal characteristics are shown in Figure 2.1. The temperature profiles were calculated with the MSIS-E-90 atmosphere model (*Hedin*, 1991) for 50°N.

The lowest atmospheric layer is the troposphere which extends from the Earth's

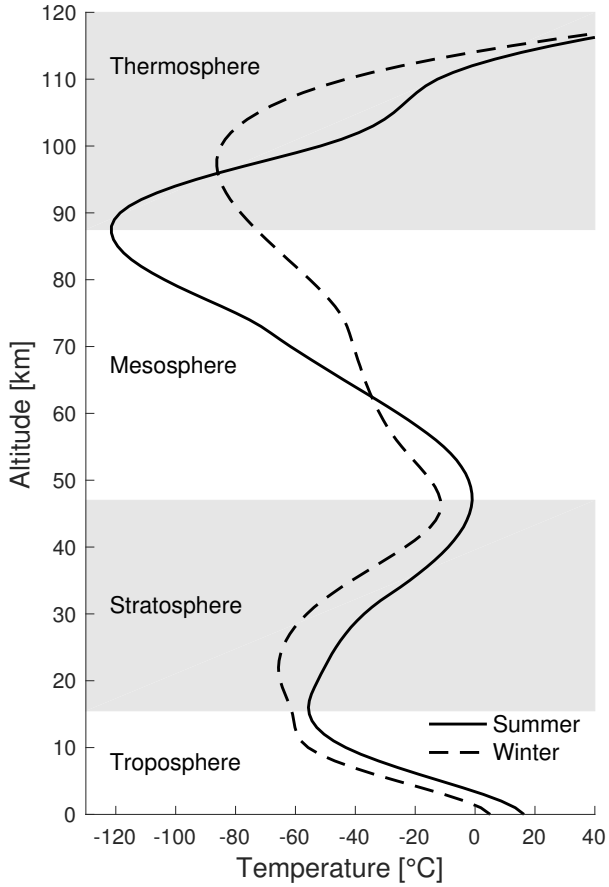

Figure 2.1: Atmospheric layers based on the atmosphere's thermal characteristics (using the summer temperature profile) and the temperature profile of the atmosphere during summer (solid line) and winter (dashed line) at 50°N.

surface to the tropopause at about 7 to 20 km altitude depending on the season, latitude, and diurnal cycle. As the troposhere is mainly heated by the Earth's surface, which in turn is heated by solar radiation, the temperature decreases with altitude up to the tropopause. Above the tropopause, temperature begins to increase gradually with altitude up to the stratopause at approximately 50 km. This atmospheric layer is called the stratosphere. The mesosphere lies between the stratopause and the mesopause and is characterized by a decrease in temperature with altitude. The mesopause is the altitude at which temperature reaches its minimum with an average temperature of about -90 °C. The altitude of the mesopause varies substantially with season and latitude, and is located between about 85 and 100 km altitude, as seen in Figure 2.1. The stratosphere and the mesosphere together are referred to as the middle atmosphere. The thermosphere extends from the mesopause to the thermopause at about 500–1,000 km altitude. Temperature in the thermosphere increases rapidly with altitude. The major constituents in the troposhere, stratosphere,

and mesosphere are molecular nitrogen (N_2) and molecular oxygen (O_2), which make up about 80% and 20% of the total number density, respectively. The mean molecular weight in these three layers is approximately stable and these layers are collectively called the homosphere. The composition of the thermosphere differs significantly from the homosphere due to diffusive separation of light and heavier compounds. This results in the mean molecular weight of air decreasing with altitude in the thermosphere. The region above 100 km altitude is thus referred to as the heterosphere.

Heating in the middle atmosphere occurs internally, mainly from the absorption of solar ultra violet (UV) radiation. The main absorber in the stratosphere is ozone. Most of the ozone in the atmosphere is located in the so-called ozone layer between approximately 15 and 35 km altitude with peak concentrations at higher altitudes in the tropics than at the poles. Ozone concentration also has a secondary maximum in the mesopause region around 90 km altitude. O_2 is less important as an absorber of solar UV radiation in the stratosphere than ozone, but important as a source of ozone through an exothermic reaction with atomic oxygen that provides additional heating in the stratosphere. Most of the heating in the stratosphere occurs in the sunlit atmosphere, but some additional heating occurs in the polar night due to adiabatic heating caused by wave-driven circulation. As ozone is the dominant absorber of solar UV radiation in the stratosphere, solar-induced variations of ozone concentration affect the radiative balance directly and the flow patterns indirectly. Cooling in the stratosphere occurs at all local times and latitudes, mainly due to infrared emission by CO_2. The main absorber of solar UV radiation in the mesosphere is O_2, which can be excited leading to a delay in the availability of absorbed energy as heat. The excited molecules can be transported significant distances in the upper mesosphere before the absorbed energy is released as heat, leading to heating during nighttime and damping of the diurnal cycle of heating by solar UV radiation. Additional contributions to the energy budget of the mesosphere are the emission of infrared radiation by CO_2, absorption of solar UV radiation by ozone, dissipative processes due to interactions with gravity waves, and the transport of heat through advection.

Latitudinal temperature gradients in the middle atmosphere drive zonal winds (winds in the east-west direction) which mix the atmospheric species leading to small variations of atmospheric quantities in the zonal direction compared to the variations

with altitude and latitude. The mean zonal winds are directed eastward (westerly winds) during winter and westward (easterly winds) during summer in the stratosphere and mesosphere, and are strongly influenced by seasonal variations in solar heating. In the winter polar stratosphere, at about 60° latitude and above about 16 km altitude, strong westerly zonal winds form a large-scale cyclone called the polar night jet that partially isolates the polar cap air mass from the lower latitudes. The geopotential structure bound by the polar night jet is called the polar vortex. Planetary-scale waves can decelerate the zonal flow and disturb the vortex, or in the case of particularly strong wave activity, reverse the direction of the zonal flow and break the vortex. The breaking of the vortex leads to a strong downward motion of the air mass and sudden stratospheric warming due to adiabatic compression. Sudden stratospheric warmings are almost exclusively a Northern Hemispheric phenomenon, as the majority of planetary waves are produced, and forced to propagate into the middle atmosphere, in the Northern Hemisphere.

Circulation in the meridional direction is driven by dissipating and breaking gravity and planetary waves propagating from the troposphere. This wave-driven circulation in the stratosphere is called the Brewer-Dobson circulation and is characterized by meridional flow from the equator to the poles. In the upper stratosphere and mesosphere, the meridional flow is a single-cell circulation from the summer pole to the winter pole. The Brewer-Dobson circulation is driven mainly by planetary waves, while the single-cell circulation is driven by gravity waves.

2.2 D region ionosphere

The ionosphere is the ionized part of the atmosphere that consists of approximately equal numbers of positive ions and free electrons alongside the neutral atmospheric gasses. Even though the amount of neutral particles in the ionosphere is multiple orders of magnitude greater than the amount of charged particles, charged particles have a great influence on the electrical properties of the surrounding neutral gasses (*Hunsucker and Hargreaves*, 2002, pp. 1). The shape and intensity of the ionosphere, i.e., electron density profile with altitude, is governed by the rate of electron production due to different ionization sources and the loss rate of free electrons due

to chemical recombination with positive ions and the attachment of electrons to neutral particles. The relative importance of different electron production and loss reactions varies in the different parts of the atmosphere. The vertical structure and idealized electron density profiles of the ionosphere for day and night are shown in Figure 2.2, and the average characteristics of the ionospheric regions are listed in Table 2.1. The different ionospheric regions display large variations, especially diurnally. The ionosphere is mainly ionized by solar electromagnetic radiation with different wavelengths of the solar spectrum being responsible for ionization in the different regions. Particle precipitation provides an additional ionization source at high latitudes.

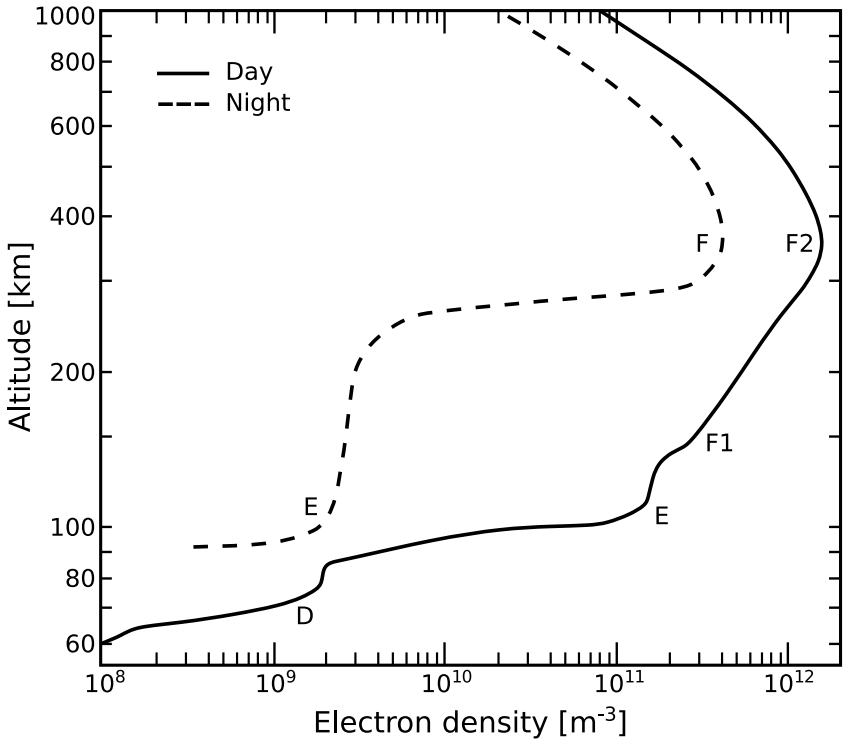

Figure 2.2: Idealized electron density profiles of the ionosphere at solar maximum during day (solid line) and night (dashed line) and the different ionospheric regions. Figure based on *Evans and Hagfors* (1968).

The *D* region of the ionosphere is located between about 60 to 95 km altitude. The upper parts of the *D* region are ionized by the Lyman α line of the solar spectrum with smaller contributions from the extreme ultra violet (EUV) and X-ray parts of the solar spectrum. The solar Lyman α flux varies with the 11-year solar cycle and the 27-day rotational period of the Sun, although these variations are small compared to the variability of the solar X-ray flux (*Brasseur and Solomon*, 2006, pp. 552). Due to the large

Table 2.1: Approximate daytime characteristics and main ionization sources of the ionospheric regions (*Aggarwal et al.*, 1979; *Hunsucker and Hargreaves*, 2002, pp. 13–14).

Region	Altitude (km)	Electron density (m^{-3})	Collision frequency (s^{-1})	Main ionization source
F2	$\sim$300[a]	10^{12}	10^{3}	EUV
F1	160–180	10^{11}–10^{12}	10^{3}	EUV
E	105–160	10^{11}	10^{4}–10^{3}	X-rays/Lyman β
D	60–90	10^{8}–10^{10}	10^{7}–10^{5}	Lyman α/GCR

[a]Altitude of maximum electron density.

variability of solar X-ray emission, the role of X-rays varies from only a minor source of ionization during normal conditions to a major one during high solar activity. Galactic cosmic rays (GCRs) are the dominant ionization source below approximately 65 km altitude with up to an order of magnitude variation of flux with the solar cycle. The diurnal variation of the *D* region is large and without direct solar radiation the main ionization sources are diffuse Lyman α, precipitating electrons and protons, and GCR. During high solar activity, sporadic ionization sources such as increased X-ray flux (especially during solar flares), relativistic electron precipitation from the radiation belts, or proton precipitation during SPEs can increase the ionization rates in the *D* region to far higher levels than during quiet conditions.

The *D* region is chemically the most complex region of the ionosphere due to the higher concentrations of minor and major species that significantly participate in photochemical reactions, and due to the different ionization sources and their large variability. Unlike in the upper ionospheric regions, negative ions hold a substantial portion of negative charge in the *D* region. Negative ions are present at altitudes below approximately 80 km, where the atmospheric density is high enough to enable the attachment of free electrons to O_2 (*Brasseur and Solomon*, 2006, pp. 570). As the reactions balancing the amount of negative ions and electrons depend on solar radiation, the carrier of negative charge changes from free electrons to negative ions during sunset and back to free electrons during sunrise (*Verronen et al.*, 2006a). Due to the change of the negative charge carrier, free electrons disappear almost completely from altitudes below 80 km at night. During the day, free electrons are nearly absent below altitudes from 65 to 70 km (*Brasseur and Solomon*, 2006, pp. 571).

3

Solar proton events and their atmospheric effects

The pathway coupling SPEs to the Earth's atmosphere and climate variability is described briefly in this chapter, from the acceleration of particles near the sun through access of solar energetic particles to the Earth's atmosphere and finally their effect on the atmosphere. For reviews of EPP impact on the atmosphere and climate, see *Gray et al.* (2010); *Rozanov et al.* (2012); *Sinnhuber et al.* (2012).

3.1 Solar proton events

SPEs, or solar energetic particle (SEP) events, are large eruptions of high-energy particles from the Sun. The emitted particles are electrons and ions, with protons being the dominant ion species (>90%). Based on current understanding, the two mechanism of particle acceleration behind SPEs are resonant stochastic acceleration related to magnetic reconnection of open field lines in solar flares and acceleration by shock waves driven by coronal mass ejections (CMEs) (e.g., *Reames*, 2013). The two acceleration mechanisms are not mutually exclusive and both mechanisms can accelerate particles during a single SPE. The durations of SPEs vary from a few hours to a few days, during which the flux of high-energy particles is elevated to multiple orders of magnitude above the quiet-time level. The energies of the accelerated particles range

from some 10 keV/nucl to multiple GeV/nucl (*Kallenrode*, 2003). The fluxes of protons during SPEs are typically monitored with geostationary satellites, such as the Geostationary Operational Environmental Satellites (GOES) operated by the National Oceanic and Atmospheric Administration (NOAA). Earth-directed SPEs are defined as periods where the >10 MeV integral proton flux measured by a geostationary satellite exceeds 10 pfu (particle flux unit, 1 cm^{-2} s^{-1} sr^{-1}). Example integral proton fluxes measured by the GOES-8 satellite[1] during an SPE in September 1998 are shown in Figure 3.1. As seen in Figure 3.1, the fluxes of >5 MeV protons increase abruptly by multiple orders of magnitude at the start of the event at 15:20 UT on 30 September. The event reaches its maximum (>10 MeV integral proton flux of 1,200 pfu) at 00:25 UT on 01 October after which the fluxes decrease gradually back to their quiet-time levels.

As the acceleration of particles in SPEs requires either solar flares or CMEs, SPEs are more common during solar maxima than during solar minima. SPEs typically occur in bursts, as they are usually caused by the same active region of the Sun. All SPEs affecting the near-Earth environment from January 1976 to the end of August 2019 are shown in Figure 3.2 together with the solar F10.7 index, which is used as a proxy for solar activity. The start times of the SPEs are shown with gray vertical lines and the F10.7 index is shown in black[2].

Although protons are the dominant source of EPP ionization during SPEs, additional ionization is produced by alpha particles and electrons. The ionization from alpha particles is small or negligible compared to protons (*Baker et al.*, 1973; *Potemra and Zmuda*, 1972). The contribution of electrons during SPEs is not well-known, but they can be a significant, if not even the dominant ionization source in the upper mesosphere-lower thermosphere region, especially during moderate or weak proton forcing (*Baker et al.*, 1973; *Potemra and Zmuda*, 1972; *Verronen et al.*, 2015).

[1] GOES satellite data are available at `https://www.ngdc.noaa.gov/stp/satellite/goes/dataaccess.html`

[2] Occurrence times of SPEs in Figure 3.2 are from `ftp://ftp.swpc.noaa.gov/pub/indices/SPE.txt` and the F10.7 index data were obtained from the GSFC/SPDF OMNIWeb interface at `https://omniweb.gsfc.nasa.gov`

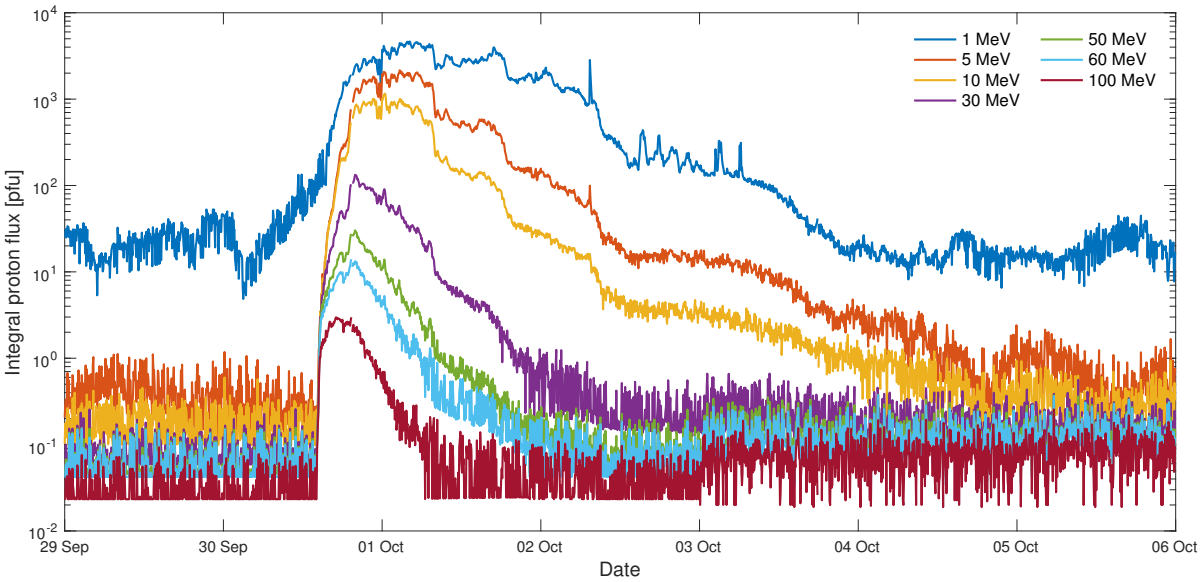

Figure 3.1: Integral proton flux of a solar proton event at different threshold energies measured by the GOES-8 satellite. The event started at 15:20 UT on 30 September 1998 and the maximum >10 MeV integral flux of the event was 1,200 pfu.

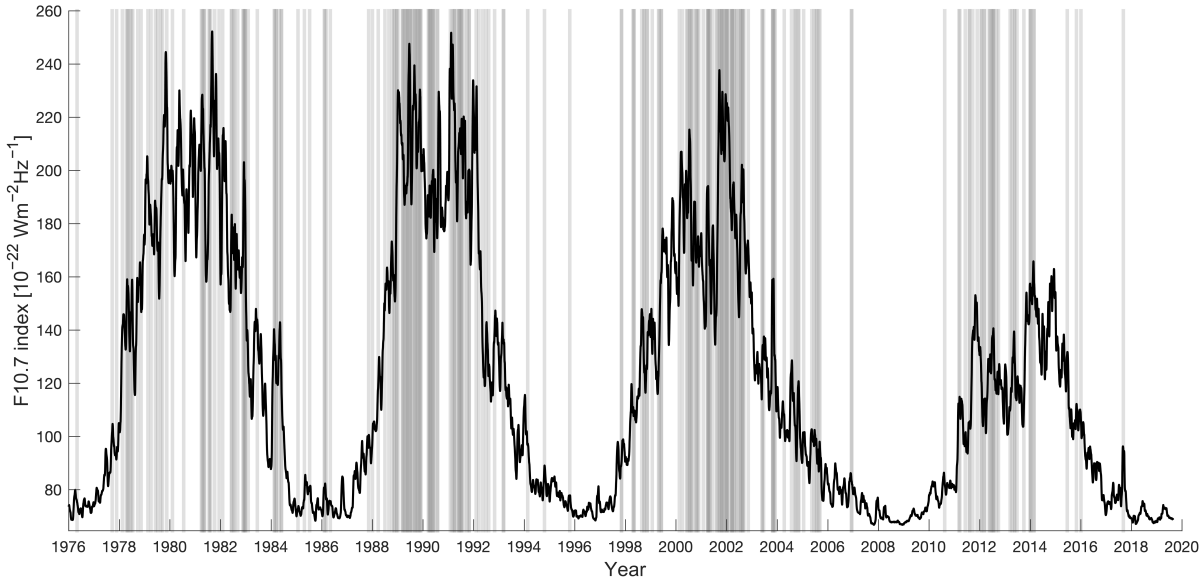

Figure 3.2: Solar proton events affecting the near-Earth environment from the beginning of January 1976 to end of August 2019 and the F10.7 index. The start times of the solar proton events are shown as gray vertical lines and the F10.7 index in black.

3.2 Access of charged particles into the atmosphere

Solar energetic particles gyrate around the magnetic field lines of the IMF as they travel out from the Sun. When the particles are emitted towards the Earth, they penetrate into space dominated by the Earth's magnetic field, the magnetosphere. Inside the magnetosphere, the particles travel along complex trajectories and some of them are able to access the Earth's atmosphere. Due to the partial guiding of particles by the Earth's magnetic field, the particles cannot enter the global atmosphere uniformly, but have easier access to the polar regions.

The access of particles into the Earth's magnetosphere is controlled in geomagnetic latitude by the particles' rigidity (*Størmer*, 1955). Rigidity is the basic parameter of adiabatic charged particle motion in a magnetic field. All charged particles with the same rigidity, charge sign, and initial conditions will have identical trajectories in a magnetic field. For a singly charged particle, rigidity in MV is defined as:

$$R = \sqrt{E^2 + 2E_0E}, \tag{3.2.0.1}$$

where E and E_0 are the kinetic energy and rest mass of the particle, both expressed in MeV. *Størmer* (1955) introduced the concept of cutoff rigidity, which is the minimum rigidity a particle must have in order to penetrate to a given geomagnetic latitude. Higher rigidities are needed for a particle to access lower geomagnetic latitudes. The cutoff rigidities can be converted to cutoff energies separately for different particle species. A cutoff latitude is the lowest geomagnetic latitude a particle of corresponding cutoff energy (rigidity) can access. In the *Størmer* (1955) formulation, the Earth's magnetic field is approximated as a static dipole field, but in reality cutoff latitudes and the Earth's magnetosphere are more complex and dynamic.

The Earth's magnetic field is affected by the solar wind and the IMF, and is compressed on the dayside and stretched on the nightside. This compression and stretching leads to day-night asymmetry of cutoff latitudes depending on MLT, so that the dayside (nightside) cutoff latitudes are poleward (equatorward) of the cutoff latitudes calculated for a dipole field (e.g., *Fanselow and Stone*, 1972). The locations of cutoff latitudes are also affected during geomagnetic storms, when the Earth's magnetic field is distorted and the intensities of the magnetospheric current systems, such as the

ring current, change (e.g., *Nesse Tyssøy and Stadsnes*, 2015). Due to the variations of the solar wind, IMF, geomagnetic activity, and magnetospheric currents, the cutoff latitudes are not static, but vary in times scales of minutes to hours. An example of cutoff latitude variations during a SPE is shown in Figure 3.3. The two polar maps in the figure depict cutoff latitudes based on particle measurements on board polar orbiting satellites for five proton energies at two selected times during a SPE in January 2012 (*Nesse Tyssøy et al.*, 2013). The left panel is representative of the general cutoff latitude distribution in the Northern Hemisphere during the SPE. The dayside cutoff latitudes for 1–16 MeV protons are poleward of the nightside cutoff latitudes, and the dayside cutoff latitudes show larger latitudinal variation between the cutoff energies than the nightside cutoff latitudes. The time period shown in the right panel coincides with the *Dst* index turning from negative to positive leading to an abrupt poleward shift of the dayside cutoff latitudes. The *Dst* index expresses the disturbance of the magnetic field at the dipole equator. Decreases in the index are caused mainly by the strengthening of the ring current with a small contribution by the cross-tail current. Increases in the index are mostly caused by the compression of the dayside magnetosphere by solar wind ram pressure increases.

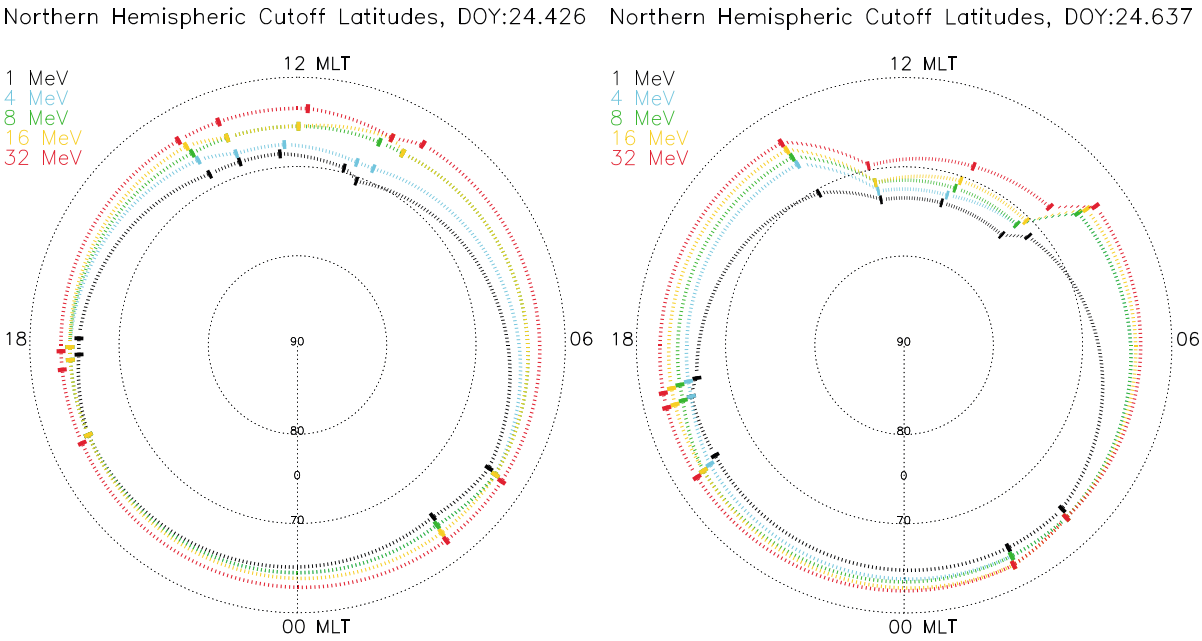

Figure 3.3: Polar maps of Northern Hemispheric cutoff latitudes based on particle measurements on polar orbiting satellites for five proton energies at two selected times during a solar proton event in January 2012. Figure from *Nesse Tyssøy et al.* (2013).

The equatorward movement of cutoff latitudes due to geomagentic activity, com-

pression of the magnetosphere, and intensification of the ring current were first observed in the late 1950s and early 1960s using balloon-borne instruments (*Freier et al.*, 1959; *Winckler and Bhavsar*, 1960; *Winckler et al.*, 1961), ionosondes (*Obayashi and Hakura*, 1960), and riometers (*Reid and Leinbach*, 1961). The first satellite observations were reported by *Axford and Reid* (1963). The movement of cutoff latitudes has since been studied and connected to geomagnetic indices *Kp*, *Dst*, and SYM-H (e.g., *Birch et al.*, 2005; *Leske et al.*, 2001; *Neal et al.*, 2013). The *Kp* index expresses the global geomagnetic field disturbance, while the SYM-H is similar to the *Dst* index, but with a higher time resolution. The day-night asymmetry of proton cutoff latitudes has been observed in multiple studies with polar orbiting satellites (*Birch et al.*, 2005; *Dmitriev et al.*, 2010; *Fanselow and Stone*, 1972; *Nesse Tyssøy et al.*, 2013). Another approach has been to use different iterations of the Tsyganenko magnetospheric field models (*Tsyganenko*, 1989, and later model versions) or global magnetohydrodynamic models to study and calculate cutoff latitudes for solar protons, and compare them to observed cutoff latitudes (e.g., *Birch et al.*, 2005; *Blake et al.*, 2001; *Kress et al.*, 2010; *Smart and Shea*, 2001, 2003). In this approach, the trajectories of particles are followed in the magnetosphere to determine their cutoff latitudes. In general, the proton cutoff latitudes from these model calculations are systematically poleward compared to observed cutoff latitudes from polar orbiting satellites and discrepancies become larger with increased geomagnetic activity (*Dmitriev et al.*, 2010, and references therein). In addition to satellite observations, riometers have been used to test the modeled cutoff latitudes from Tsyganenko-based parametrizations (e.g., *Clilverd et al.*, 2007; *Rodger et al.*, 2006; *Rogers and Honary*, 2015). The Tsyganenko-based cutoff latitudes have been found to agree reasonably well with riometer observations when shifted equatorward by a few degrees and when their dependence on the *Kp* index has been modified. *Rogers and Honary* (2015) also tested the cutoff latitude model by *Dmitriev et al.* (2010), which performed better than the Tsyganenko-based parametrization by *Smart* (1999).

Multiple models that estimate the locations of the proton cutoff latitudes have been published since the original formulation by *Størmer* (1955). These cutoff latitude models have been constructed either numerically, by tracing the trajectories of particles in the Tsyganenko models to determine their cutoff latitudes (e.g., *Smart and Shea*,

2001, 2003), or with empirical approaches using observed cutoff latitudes from polar orbiting satellites (*Dmitriev et al.*, 2010; *Neal et al.*, 2013; *Nesse Tyssøy and Stadsnes*, 2015; *Ogliore et al.*, 2001). A parametrization is formulated for the cutoff latitudes in both approaches with, or without, a dependence on geomagnetic indices, solar wind parameters, or MLT.

The cutoff latitude models by *Dmitriev et al.* (2010) and *Nesse Tyssøy and Stadsnes* (2015) are tested statistically in Paper III using observations from 13 riometer stations and the DRAP model during 73 SPEs between 1997 and 2010. These two cutoff latitude models were chosen, as their parametrizations of cutoff latitudes include the day-night asymmetry and geomagnetic activity, as well as the cutoffs of low to medium-energy protons (<20 MeV). The inclusion of lower energy protons is important, as lower energy protons produce odd nitrogen and odd hydrogen in the mesosphere (see Section 3.3), and their day-night asymmetry is more pronounced compared to protons with higher energies. Both of the tested cutoff latitude models are based on cutoff latitudes observed with instruments on board Polar Operational Environmental Satellites (POES) operated by NOAA. The parametrization in the *Dmitriev et al.* (2010) model is based on fitting ellipses to the observed data with multiple linear regression using rigidity, the *Kp* index, the *Dst* index, the geodipole tilt angle, and MLT as the explanatory variables. The *Nesse Tyssøy and Stadsnes* (2015) model uses multiple linear regression to fit separate dayside and nightside cutoff latitudes to observed cutoff latitudes at fixed energies. The explanatory variables are the *Dst* index and the B_z component of the IMF for the dayside cutoff latitudes, and the *Dst* index and third root of the solar wind ram pressure for the nightside cutoff latitudes. Due to the different parametrization approaches, the *Dmitriev et al.* (2010) model is continuous with MLT and energy, while the *Nesse Tyssøy and Stadsnes* (2015) model provides cutoff latitude estimates only for discrete energies and no cutoff latitudes for dawn and dusk.

The two cutoff latitude models were tested by dividing the riometer observations to cut and not cut observations based on the model predictions, and by comparing modeled CNA from DRAP with each cutoff model to observations. Based on the analyses presented in Paper III, the *Dmitriev et al.* (2010) model performs slightly better statistically than the model by *Nesse Tyssøy and Stadsnes* (2015), and is more suited for

use in atmospheric and climate modeling due to its continuity with energy and MLT. The effect of geomagnetic cutoff was clearly visible in the comparison of modeled and observed CNA equatorward of 66° geomagnetic latitude in sunlit conditions. The analyses in Paper III also revealed that the *Dmitriev et al.* (2010) model produces unrealistically low cutoff latitudes when the the *Kp* and *Dst* indices have extreme values, and that during these conditions, the lower energy cutoff latitudes are equatorward of the higher energy cutoff latitudes. This unrealistic behavior needs to be taken into account when using the *Dmitriev et al.* (2010) model by limiting the produced cutoff latitudes to a more realistic range or by modifying the parametrization. The extremely low cutoff latitude values from the *Dmitriev et al.* (2010) model could not be studied in Paper III, as the locations of the riometers are limited to high latitudes. The new method, presented in Paper I (see Section 4.2), of using SuperDARN radars to estimate HF radio wave absorption could possibly be used in the future to test the extreme extent of the cutoff latitudes predicted by the *Dmitriev et al.* (2010) model.

3.3 Atmospheric effects of energetic particle precipitation

As energetic particles move in the atmosphere they lose energy through collisions with atmospheric gases. The neutral atmospheric molecules are ionized in these collisions and ion-electron pairs are formed. The average energy needed to form an ion pair is approximately 35 eV (e.g., *Porter et al.*, 1976). As the protons penetrate deeper into the atmosphere, they keep losing energy and forming ion pairs along their path, so that, for example, a 5 MeV proton can form up to about 143,000 ion pairs along its path before stopping. The altitudes affected by energetic particles are therefore dependent on particle energy. The ionization rate profiles of protons with different energies are shown in Figure 3.4. The ionization rates are calculated for monoenergetic proton beams with a flux of 1 pfu (*Turunen et al.*, 2009). Protons with energies between about 2 and 40 MeV can penetrate down to the mesosphere, and protons with energies >40 MeV can penetrate down to the stratosphere. As seen from Figure 3.4, the energy loss of protons is largest near their stopping height. The ionization caused by SPEs leads to production of odd nitrogen (NO_x) and odd hydrogen (HO_x)

species. The odd nitrogen family consist of atomic nitrogen (N), nitric oxide (NO), and nitrogen dioxide (NO_2), and the odd hydrogen family of atomic hydrogen (H), hydroxyl (OH), and hydroperoxyl (HO_2).

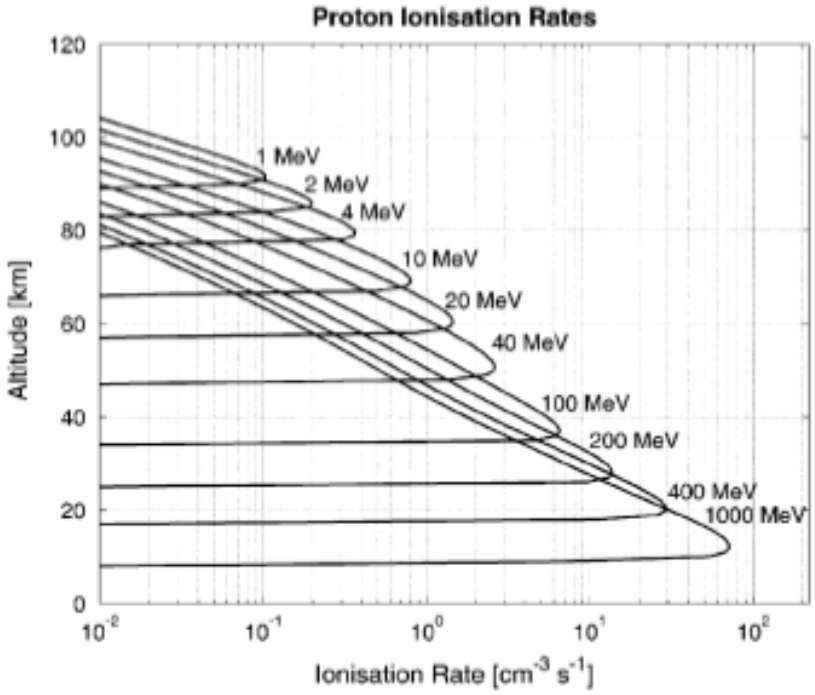

Figure 3.4: Ionization rate profiles for monoenergetic beams of 1–1,000 MeV protons.[3]

NO_x is produced in the stratosphere mainly by oxidation of nitrous oxide (N_2O) (*Brasseur and Solomon*, 2006, pp. 328–333) and by dissociation of N_2 due to solar radiation or energetic particles in the mesosphere and thermosphere (*Brasseur and Solomon*, 2006, pp. 351–353). During SPEs, energetic protons provide an additional source of NO_x, as the ionization and dissociation of atmospheric gasses lead to increased production of N^+, N_2^+, O^+, and O_2^+, which produce NO_x species in further reactions (*Sinnhuber et al.*, 2012). Large SPEs can increase the NO_x concentrations significantly above the background level, especially in the stratopause to middle mesosphere region, where the quiet-time concentration is low. Up to order-of-magnitude increases have been observed in these regions compared to the background level after large SPEs (e.g., *Jackman et al.*, 2001). NO_x is destroyed in the middle atmosphere by photodissociation of NO, which is followed by a cannibalistic reaction (reaction involving two NO_x molecules

[3]Reprinted from Journal of Atmospheric and Solar-Terrestrial Physics, 71, Esa Turunen, Pekka T. Verronen, Annika Seppälä, Craig J. Rodger, Mark A. Clilverd, Johanna Tamminen, Carl-Fredrik Enell, Thomas Ulich, Impact of different energies of precipitating particles on NO_x generation in the middle and upper atmosphere during geomagnetic storms, 1,176–1,189, Crown copyright (2008), with permission from Elsevier.

that are both destroyed) with the produced ground state atomic nitrogen (*Brasseur and Solomon*, 2006, pp. 353). The loss rate of NO_x is therefore dependent on the level of solar illumination. The photochemical lifetime of NO_x in sunlit conditions is about one day in the mesosphere and lower thermosphere, and from days to months in the stratosphere. In the absence of solar illumination, for example during polar night, the lifetime of NO_x is of the order of months in the middle atmosphere (*Brasseur and Solomon*, 2006, pp. 342–344).

The main sources of HO_x production are oxidation of water vapor in the stratosphere and lower mesosphere, and photodissociation of water vapor in the upper mesosphere and thermosphere (*Solomon et al.*, 1981). Additional HO_x is produced by SPEs, but the production process is far more complex than that of NO_x, and involves water cluster ions and negative ions. For a thorough discussion of HO_x ion chemistry, see *Solomon et al.* (1981). Large SPEs have been modeled and observed to cause order-of-magnitude increases in HO_x concentrations (*Verronen et al.*, 2006b). The main loss mechanisms of HO_x in the middle atmosphere are reactions with atomic oxygen and cannibalistic reactions. The photochemical lifetime of HO_x is of the order of minutes in the stratosphere and from hours to a day in the mesosphere (*Brasseur and Solomon*, 2006, pp. 321–322).

The significant production of NO_x and HO_x species during EPP can enhance ozone depletion in the middle atmosphere, as both species are able to efficiently destroy ozone in catalytic reactions (*Bates and Nicolet*, 1950; *Lary*, 1997; *Brasseur and Solomon*, 2006, pp. 401–416). Ozone is depleted in these catalytic chemical cycles, while the catalyst, NO_x or HO_x, is not destroyed and can continue destroying ozone throughout its lifetime. NO_x dominates the catalytic cycles in the stratosphere, while HO_x is the dominant catalyst in the mesosphere (*Lary*, 1997). Ozone depletion by HO_x remains local to the altitudes of HO_x production and the duration of ozone depletion is short due to the short lifetime of HO_x. This form of ozone loss in the mesosphere, dominated by HO_x, is called instantaneous ozone loss. The lifetime of NO_x is long enough, especially in low illumination conditions, to be affected by atmospheric transport. NO_x can be transported tens of kilometers downwards from where it was produced (e.g., *Funke et al.*, 2014), and the ozone depletion by NO_x enhancements can reach the lower stratosphere (e.g., *Crutzen et al.*, 1975; *Funke et al.*, 2014; *Jackman et al.*, 2000) and per-

sists for months (*Randall et al.*, 2001; *Seppälä et al.*, 2004). This downwards transport of NO_x and the following ozone depletion is especially pronounced inside the polar vortex. *Denton et al.* (2018) analyzed balloon-borne ozone measurements at 10–35 km altitudes for 191 SPEs between 1989 and 2016, and concluded that no ozone loss was observed at sites completely outside the polar vortex. Ozone loss due to the descent of NO_x into the stratosphere from the mesosphere and lower thermosphere is referred to as the EPP indirect effect. Ozone loss in the stratosphere due to NO_x produced in-situ is referred to as the EPP direct effect (*Randall et al.*, 2007).

EPP can affect the heating and cooling rates in the atmosphere in multiple ways: directly due to Joule heating and particle heating, and indirectly due to chemical changes leading to exothermic reactions, i.e., chemical heating, and changes to radiative heating and cooling rates. The contribution of Joule and particle heating on the heating and cooling rates of the middle atmosphere due to EPP are negligible (*Jackman et al.*, 2007; *Sinnhuber et al.*, 2012). The effect of EPP on chemical heating rates is not clear, but chemical heating has been discussed as a significant source of heat in the mesopause region, at least in the absence of EPP (*Sinnhuber et al.*, 2012). As discussed in Section 2.1, radiative heating due to absorption by ozone and O_2 is the main heating mechanism in the middle atmosphere, and ozone losses due to EPP lead to changes in the heating and cooling of middle atmosphere. Changes in the heating and cooling rates of the middle atmosphere can then cause changes in atmospheric dynamics, including interactions between gravity wave propagation and breaking, and mean zonal winds (*Seppälä et al.*, 2013; *Sinnhuber et al.*, 2012). Changes in middle atmospheric dynamics can propagate down into the troposphere causing regional surface air temperature anomalies during the winter season (*Arsenovic et al.*, 2016; *Baumgaertner et al.*, 2011; *Rozanov et al.*, 2005; *Seppälä et al.*, 2009). While the exact mechanisms of this coupling between solar activity and the climate system are not yet clearly understood, EPP seems to be a source of natural climate variability (*Andersson et al.*, 2014; *Gray et al.*, 2010; *Rozanov et al.*, 2012). Due to its complexity and the lack of long-term observations, the coupling between solar activity and the climate system is studied with chemistry and climate models. The use of these models to study the atmospheric effects of EPP and the solar-climate coupling is described briefly in Chapter 5.

Increased electron densities in the *D* region cause absorption of radio waves, and large SPEs can cause complete HF radio blackouts in the polar regions that persist for the duration of the SPE. The absorption of radio waves is used to study EPP fluxes, and the spatial and temporal behavior of EPP. HF radio waves are also important for long-distance radio communication and aircraft communication in polar routes (*Neal et al.*, 2013), providing an operational motivation for the study and modeling of radio wave absorption caused by EPP. The use of radio wave absorption and CNA to study the atmospheric effects of EPP is discussed in Chapter 4, and the modeling of CNA is discussed in Section 5.1.

4

Ground-based observation of atmospheric effects of solar proton events

The first SPEs were reported by *Forbush* (1946) as sudden increases in intensity in ground-level ion chambers. The ionospheric effects of SPEs were first observed in very high frequency (30–300 MHz) communication links during the 23 February 1956 event as large increases in absorption that could not be regarded as a special case of auroral absorption (*Bailey*, 1957). In the following couple of years, other absorption events were observed with no associated ground-level enhancements, indicating that the Sun can release particles with enough energy to cause radio wave absorption, but not reach the surface of the Earth (*Bailey*, 1964). These events were characterized by large scale absorption that gradually reduced during the next few days and had a strong diurnal variation. As the absorption was limited to the polar cap, the name polar cap absorption (PCA) was coined for the phenomenon.

The ionization caused by SPEs can be observed and studied with, for example, incoherent scattering radars, very low frequency receivers (3–30 kHz), and riometers. Riometers and CNA are used in all papers included in this thesis, and both are described in Section 4.1. A new method for the observation of radio wave absorption caused by SPEs with the SuperDARN radars is presented in Paper I, and SuperDARN and the method are both described in Section 4.2.

4.1 Riometers and cosmic noise absorption

A riometer (Relative Ionospheric Opacity Meter, Extra-Terrestrial Electromagnetic Radiation; *Little and Leinbach*, 1959) is a stable receiver with a known pointing direction and beam pattern. The operating frequency of a riometer has to be greater than the penetration frequency of the ionosphere in order to receive the signal, i.e., cosmic noise, from outer space. Operating frequencies of riometers are typically between 30 and 40 MHz.

Cosmic noise can be assumed to be constant with time at a fixed point in the radio sky, so a reduction in the received intensity is caused by absorption of the signal in the ionosphere and not by variation of the cosmic noise source. Despite being constant over time, cosmic noise varies over the radio sky due to the distribution of extra-terrestrial radio sources. As a riometer is pointed to a fixed direction, typically to the local zenith, the pointing direction scans the radio sky as the Earth rotates. The riometer will therefore point to the same location in the radio sky every sidereal day, which is four minutes longer than a standard day. In order to measure the amount of absorption due to the ionosphere, the measured cosmic noise signal has to be compared to the estimated intensity of the cosmic noise signal without any ionospheric absorption.

The estimated intensity of the cosmic noise without absorption as a function of sidereal time is called a quiet-day curve (QDC). A QDC is traditionally produced by superimposing measured cosmic noise from a period of time as a function of sidereal time, and determining the upper envelope of the distribution, which is the intensity of cosmic noise without absorption. In principle the idea is very simple, but can be difficult in practice. The possible presence of man-made radio frequency interference or solar radio emissions prevents the direct selection of the upper envelope (*Browne et al.*, 1995), so the upper undisturbed envelope has to be estimated. The QDC can be determined automatically or manually, like in the case of the Longyearbyen imaging riometer (*Stauning and Hisao*, 1995). The automatic determination can be based on, for example, calculating a percentile of the superposed distribution (*Browne et al.*, 1995), fitting a sinusoidal curve to the measurements from previous days (SGO riometers used in Papers II and III), or characterizing the shape of the cosmic noise without fitting a curve to a specific subset of data (GO-Canada riometers used in all papers).

After the QDC has been produced, CNA in decibels, A, can be calculated from

$$A = 10 \log_{10} \left(\frac{P_0}{P} \right), \tag{4.1.0.1}$$

where P_0 is the received power without absorption, i.e., the QDC, and P is the power measured by the riometer (e.g., *Hunsucker and Hargreaves*, 2002, pp. 206). As the level of absorption depends on the operating frequency, it becomes necessary to convert absorption to a common frequency when using data from riometers with different operating frequencies. According to the generalized magnetoionic theory (*Sen and Wyller*, 1960) the absorption varies as the inverse square of the frequency, so the absorption in the wanted common frequency, $A(f)$, is:

$$A(f) = A_0 \left(\frac{f_0}{f} \right)^2, \tag{4.1.0.2}$$

where f is the wanted common frequency and A_0 is the absorption measured at frequency f_0 (e.g., *Rosenberg et al.*, 1991). The frequency dependence deviates from the inverse square relationship at altitudes below about 70 km, where the electron-neutral collision frequency becomes equal to or greater than the effective angular radio frequency (*Rosenberg et al.*, 1991) or when strong spatial gradients are in the riometer beam. Other relationships for the frequency dependence of absorption have been determined empirically. For example, *Patterson et al.* (2001) determined from 20.5 to 51.4 MHz dayside CNA observations that the frequency exponent depends on particle energy during SPEs and varies from -1.2 to -1.8, while *Sauer and Wilkinson* (2008) showed that dayside CNA between 10 and 50 MHz varies with frequency as $f^{-1.5}$.

Most riometers are wide-beam riometers that produce a single wide beam, typically 60° at the full width half maximum point, towards the local zenith. Another major riometer type is the imaging riometer system, which produces multiple narrow beams at different pointing directions. Wide-beam riometers are significantly simpler and cheaper systems compared to imaging riometers, but have poor spatial resolution, as the 60° beam is about 100 km in diameter when projected to the *D* region. The narrow beams of an imaging riometer enable better spatial resolution and the area covered by a imaging riometer in the *D* region is about 250 km by 250 km (*Browne*

et al., 1995; *Stauning and Hisao*, 1995). A disadvantage of all single frequency riometer systems is that the differential absorption from the whole atmospheric column is integrated together into a single CNA value and the measurements contain no altitude information. Other disadvantages of riometers are that they are susceptible to man-made radio frequency interference, solar radio emission, and errors in the QDC determination.

The absorption of radio waves in the ionosphere depends on electron density and the effective collision frequency (*Hunsucker and Hargreaves*, 2002, pp. 151). Electron-neutral collisions are the dominant type of electron collisions below the *F* region ionosphere and therefore the electron-neutral collision frequency is the dominant collision frequency type for CNA (*Aggarwal et al.*, 1979; *Stauning*, 1996). As electron density increases rapidly with altitude, while the electron-neutral collision frequency decreases exponentially (see Table 2.1), most absorption occurs in the *D* region during SPEs. In the *D* region, the ionization (electron density) from proton precipitation is sufficient, and the density of the atmosphere is high enough to ensure high electron-neutral collision frequencies. As CNA is dependent on electron density, and the negative charge in the *D* region transitions from free electrons to negative ions during sunset, CNA has a strong diurnal variation and low values in dark ionospheric conditions. It also follows from the electron density and collision frequency dependence of CNA, that the energy and flux of precipitating energetic protons are related to the amount of CNA produced by particle precipitation.

Potemra (1972) speculated that 15 MeV protons are most responsible for daytime CNA, but could not verify this due to lack of differential flux measurements. Using numerical model results, *Patterson et al.* (2001) determined that both daytime and nighttime maximum CNA occurs for 20 MeV protons. *Kavanagh et al.* (2004) used riometer observations and GOES-8 measurements taken during 51 SPEs from 1995 to 2001, and determined that protons with energies between 15 and 44 MeV were best correlated with daytime CNA. Based on the result of both *Patterson et al.* (2001) and *Kavanagh et al.* (2004), the absorption efficiency of protons decreases at energies higher than about 80 to 100 MeV.

CNA has been determined empirically to be proportional to the square root of integral proton flux, $J(> E_{\mathrm{t}})$ in numerous studies starting from the 1960s (e.g., *Bailey*,

1964; *Potemra*, 1972; *Sellers et al.*, 1977; *Van Allen et al.*, 1964) with different values for the threshold energy E_{t}. *Kavanagh et al.* (2004) found that CNA in sunlit conditions is best correlated with the square root of $>$10 MeV integral flux. Their results also indicated that this relationship is robust and not significantly affected by the hardness of the proton spectrum or geomagnetic activity. The relationship was confirmed by *Rodger et al.* (2006) by using the Sodankylä Ion Chemistry (SIC) model for periods not affected by rigidity cutoffs. *Clilverd et al.* (2007) used the SIC model to study the relationship between integral proton flux and CNA in dark conditions and found that CNA is proportional to $J(> 5\,\mathrm{MeV})^{0.75}$. The approximately linear relationship of CNA and integral proton flux is also the basis for energy threshold CNA models, which are described in Section 5.1.

The noise power available to a riometer during normal conditions with low ionospheric absorption is determined by the radio noise temperature of the sky with negligible contributions from the absorbing region of the ionosphere and losses in the riometer instrumentation (*Little and Leinbach*, 1958). When the ionospheric absorption increases to large values ($\sim$10 dB), these normally negligible sources of noise become significant and the riometer receives additional signals from the absorbing ionosphere and the lossy hardware (*Browne et al.*, 1995; *Hargreaves and Detrick*, 2002). These additional noise sources cause the riometer response to become nonlinear and the measured CNA becomes lower than the true CNA. This nonlinearity also causes the relationship between CNA and integral proton flux to become nonlinear. A correction method for the nonlinearity of riometers is formulated and presented in Paper II. The method is based on fitting a correction function using observed and modeled CNA data. The correction function described in Paper II is:

$$A \;= 10 \cdot \log_{10}\left(\frac{1+1/R}{10^{-A_{\mathrm{s}}/10}+1/R}\right), \tag{4.1.0.3}$$

where A is the observed CNA, A_{s} is the true CNA, and R is the ratio of wanted and unwanted noise. The function is fitted with observed CNA as A, modeled CNA data as the true CNA, and R as a free parameter. CNA was modeled in Paper II with the WACCM-D model (see Section 5.1) and the correction function was fitted for each riometer separately without limiting the data with solar zenith angle. The correction method works well for the northernmost wide-beam riometers used in Paper II, but is

sensitive to data selection. The observed CNA from the more equatorward riometers are affected by geomagnetic cutoffs and electron precipitation leading to poor fits of the correction function. Based on a cursory examination in Paper II, using data only from sunlit ionospheric conditions for the fitting of the correction function improves the fit and is advised in future studies. An additional improvement to the correction method performance should be achieved, if the effects of geomagnetic cutoffs are also implemented when modeling CNA for the correction method fitting.

4.2 SuperDARN

SuperDARN is a global network of HF coherent scatter radars designed to measure large-scale ionospheric plasma convection (*Chisham et al.*, 2007; *Greenwald et al.*, 1995; *Lester*, 2013). As of September 2019, the network consists of 23 radars in the Northern Hemisphere and 13 radars in the Southern Hemisphere. The radars measure backscatter from field-aligned electron density irregularities in *E* and *F* regions of the ionosphere (see Table 2.1). Backscatter from these ionospheric regions is used as a tracer for measuring plasma convection in the *F* region. The radars also detect backscatter from the ground and sea due to total internal ionospheric reflection and from meteor plasma trails at about 90–100 km altitude.

Each of the SuperDARN radars consists of a linear array of log-periodic or twin-terminated folded dipole antennas, which produce a narrow beam that can be steered to either 16 or 24 different azimuthal directions depending on the radar. The radar beam is narrow in the azimuthal direction (about 3.24°), but wide in the vertical elevation, exhibiting significant gain from about 10° to 45° in vertical elevation (e.g., *Milan et al.*, 1997a). The radars are designed to operate at 8–20 MHz frequency range, but most radars operate in the 10–15 MHz range. As the different beam directions are sampled sequentially in the standard operating mode, it takes 1 or 2 minutes to scan all beam directions in the field of view determining the time resolution of the data products.

The standard data products of SuperDARN are power (signal-to-noise ratio), Doppler velocity, and spectral width of the backscatter, which have been used to study a variety of ionospheric phenomena. In addition to the standard data products, the Super-

DARN data files include lower-level data products, such as the background radio noise level at the radar operating frequency (sky noise). The background radio noise level measurements are required to process raw radar data in the SuperDARN data analysis software and determine which range gates (incremental distance along one beam) contain coherent scatter. The background radio noise level is measured for each scan at all range gates and recorded in the SuperDARN data files, but is not normally used for science applications.

A new method for using the routine SuperDARN background radio noise measurements to observe the spatial and temporal evolution of HF radio wave attenuation during SPEs is presented in Paper I. In this method, the measured background radio noise from SuperDARN is analyzed using similar methods to those used in riometry. As with riometers, a QDC needs to be calculated for the background noise in order to estimate the level of attenuation. With SuperDARN, QDCs have to be generated separately for each radar beam and frequency band, as the background noise varies with azimuthal direction and frequency. Unlike the cosmic radio noise measured by riometers, the background radio noise at SuperDARN operating frequencies is dominated by atmospheric radio noise caused by global lightning activity which varies as a function of solar time. Therefore, the SuperDARN QDCs need to be generated as a function of solar time.

This method was used in Paper I to estimate the level of attenuation during two SPEs in September 2017. QDCs were produced for the SuperDARN background radio noise during undisturbed conditions preceding the SPEs and the degree of attenuation was then estimated from the difference between the measured background noise and the QDC. The radar-derived attenuation from the Rankin Inlet SuperDARN radar (62.8°N, 92.1°W) agreed qualitatively with CNA measured by the Taloyoak riometer (69.54°N, 93.56°W) with some differences in amplitude and behavior. Scaling of the attenuation data to a common frequency, the high variability of the atmospheric noise, and the different methods used to produce QDCs for SuperDARN and the riometer are likely the main contributors to the differences between the two instruments. All Northern Hemisphere SuperDARN radars were used to observe the spatial and temporal evolution of the absorption during the two SPEs. The absorption associated with the SPEs was only observed by high-latitude and polar cap radars, but no fur-

ther spatial information of the SPE impact area was obtained due to difficulties with assigning a specific location to the absorption. In Paper I, the measured attenuation was concluded to occur close to the radar site (within a few hundred km) as the spatial extent of proton precipitation is limited to the polar regions, no radar backscatter was detected during the periods of strong attenuation, and the echo returns of the used radars are usually dominated by half-hop ionospheric backscatter (less than 500 km ground distance, *Milan et al.*, 1997b). *Berngardt et al.* (2019) reached a contradicting result and concluded that the daytime background noise attenuation occurs at altitudes of the *D* and *E* regions at the distance of the first hop (about 1,000 km ground distance, *Milan et al.*, 1997b).

This new method can be used to study PCA at middle to polar latitudes and supplement other ground-based data. As SuperDARN consists of a large amount of radars with wide spatial coverage and over 20 years of continuous measurements, the method has great potential for future use. Paper I also highlights the possibility to use routine background radio noise measurements from SuperDARN in science applications. At the time of the publication of Paper I, only two previous studies had used the background radio noise measurements in science applications (*Berngardt et al.*, 2018; *Ponomarenko et al.*, 2016) and, as of September 2019, three other studies have been published (*Berngardt et al.*, 2019; *Bland et al.*, 2019; *Chakraborty et al.*, 2019). *Chakraborty et al.* (2019) used the method presented in Paper I to calculate HF radio wave attenuation estimates.

5

Modeling of atmospheric effects of solar proton events

The link between EPP and regional climate variability has been recognized in multiple studies, but the mechanisms and the contribution of EPP to climate variability are not yet well understood. The current understanding of the effect of EPP on the atmosphere is described briefly in Section 3.3. Different aspects of atmospheric effects of SPEs have been modeled in numerous studies using a variety of models of different complexities (e.g., *Baumgaertner et al.*, 2010; *Jackman et al.*, 2000, 2005, 2007, 2008; *Verronen et al.*, 2006b, 2008). *Funke et al.* (2011) compared the atmospheric chemistry response of nine different atmospheric models and the response in satellite observations to the October-November 2003 SPEs. The models were able to reproduce the main observed features reasonably well, but issues with the used proton forcing ionization rates and the need for additional ion chemistry in the models were identified. The atmospheric effects of SPEs are considered to be more or less well-known by the research community, and the focus has shifted increasingly towards the atmospheric effects of EEP. One reason for this is that SPEs are rare extreme events, while EEP in some form is almost always present. Most modeling studies have focused on intense particle precipitation events (SPEs or strong EEP events) and their short-term effects, as the strong atmospheric response is easier to identify from model results and compare to satellite observations. Due to the complexity of the atmospheric response to

EPP, chemistry-climate models are needed to study the effects of EPP on ozone loss, atmospheric dynamics, and climate, especially at long timescales and global spatial scales. A substantial body of work has been published using chemistry-climate models to study different aspects of the atmospheric effects of SPEs (e.g., *Baumgaertner et al.*, 2010; *Jackman et al.*, 2009; *Pettit et al.*, 2018) and EEP (e.g., *Andersson et al.*, 2018; *Arsenovic et al.*, 2016; *Baumgaertner et al.*, 2011; *Kyrölä et al.*, 2018; *Marsh et al.*, 2007; *Newnham et al.*, 2018; *Smith-Johnsen et al.*, 2018) at varying timescales.

CNA model are used for both operational and scientific purposes. Real-time absorption estimates from CNA models are used by airlines flying on polar routes, as they rely on HF radio communications close to the poles where satellite communications are not available (*Neal et al.*, 2013). As described in Chapter 4, the absorption of radio waves can be used to study EPP and its effects in the atmosphere. CNA models can be used when CNA observations are not available, or to compare the expected level of CNA from models to observations. Comparing modeled and observed CNA enables the study of, for example, the temporal and spatial variations of EPP, the relative strengths of different EPP sources, and the EPP forcing used in models.

CNA modeling and results from Papers II and III are discussed in Section 5.1, and the spatial estimation of the SPE impact area, based on the results of Papers II and III, is discussed in Section 5.2.

5.1 Cosmic noise absorption modeling

CNA models aim to estimate the level of CNA based on observed fluxes of solar protons and other ionization sources. Other sources of EPP or X-rays from solar flares are also included in some models. Two different CNA modeling approaches are presented in this section: 1) empirical energy threshold models and 2) full-profile models. Energy threshold models are based on the empirical relationship between CNA and the square root of the integral proton flux (see Section 4.1). The threshold energy of the integral proton flux and any scaling constants in the model are chosen empirically. In full-profile models, CNA is determined by calculating differential absorption (dB/km), i.e., rate of absorption as a function of altitude, from a modeled atmosphere. The DRAP model (*Akmaev*, 2010; *Sauer and Wilkinson*, 2008) is an example of an empirical

energy threshold model and is used in Paper III. A full-profile approach is used with data from the WACCM-D model (*Verronen et al.*, 2016) in Paper II. Short descriptions of both methods, as used in Papers II and III, are given here as examples of the two CNA modeling approaches.

The modeling of absorption due to solar protons in the DRAP model is based on the empirical relationship between CNA and the square root of integral proton flux:

$$A = m\sqrt{J(> E_{\mathrm{t}})}, \tag{5.1.0.1}$$

where A is CNA at 30 MHz in dB, m is a constant, and E_{t} is the threshold energy of the integral proton flux J. The model uses separate daytime and nighttime empirical values determined by *Sellers et al.* (1977) for m and E_{t}. These values are for fully developed sunlit and dark ionospheric conditions, and the twilight transition is interpolated between the two. In the standard DRAP formulation, twilight CNA is calculated as a bilinear composition of the sunlit and dark CNA values, with twilight solar elevation angle bounds of 10° (80° solar zenith angle) and -10° (100° solar zenith angle):

$$A = A_{\mathrm{d}}(El + 10^{\circ})/20^{\circ} - A_{\mathrm{n}}(El - 10^{\circ})/20^{\circ} \text{ dB}, \tag{5.1.0.2}$$

where El is the solar elevation angle and subscripts d and n denote day and night, respectively. This method results in discontinuities at the twilight bounds, which was addressed by *Rogers et al.* (2016) by formulating a new smooth weighting function, Z_{d}, for the twilight transition using the Gauss error function:

$$Z_{\mathrm{d}}(\chi) = \tfrac{1}{2}\left(1 - \mathrm{erf}\left(\tfrac{\chi - \frac{1}{2}(\chi_{\mathrm{u}} + \chi_{\mathrm{l}})}{\frac{1}{2}(\chi_{\mathrm{u}} - \chi_{\mathrm{l}})}\right)\right), \tag{5.1.0.3}$$

where $\mathrm{erf}()$ is the Gauss error function, χ is the solar zenith angle, and χ_{u} and χ_{l} are the upper and lower solar zenith angle bounds of the twilight transition, respectively. The solar zenith angle bounds of the twilight transition were separately optimized by *Rogers et al.* (2016) for sunrise and sunset, which is required to take into account the asymmetry of CNA between sunrise and sunset. The optimized twilight bounds and the smooth weighting function are used in the DRAP implementation of Paper III. CNA at twilight conditions is then calculated as a linear interpolation using the weighting

function:

$$A \quad = A_{\mathrm{n}}(1 - Z_{\mathrm{d}}) + A_{\mathrm{d}} Z_{\mathrm{d}}. \tag{5.1.0.4}$$

The standard DRAP model uses the cutoff energies calculated by *Smart* (1999) for each model grid point. If the cutoff energy at a model grid point is greater than the threshold energy, the cutoff energy is used as the threshold energy of the integral proton flux. In Paper III, the cutoff latitude models by *Dmitriev et al.* (2010) and *Nesse Tyssøy and Stadsnes* (2015) are used instead of the *Smart* (1999) model and implemented to the model calculations differently.

Full-profile CNA modeling is based on calculating differential absorption (dB/km) as a function of altitude from electron density and electron-neutral altitude profiles. The altitude profiles of electron density and collision frequency are calculated from altitude profiles of atmospheric quantities from a suitable atmospheric model, such as the SIC model (e.g., *Clilverd et al.*, 2007; *Rogers et al.*, 2016; *Verronen et al.*, 2006a), NRL-MSISE-00 (*Rogers and Honary*, 2015), or WACCM-D. The electron density profiles in these models depend on the input particle and radiation forcing, while the electron collision frequencies need to be calculated from the density profiles of electrons and neutral species. The WACCM-D model is used in Paper II to produce the atmospheric conditions that form the basis for the CNA calculations. For a full description of WACCM-D and its lower ionospheric performance, see *Verronen et al.* (2016). For a description of standard WACCM, see *Marsh et al.* (2013).

WACCM-D is a variant of the global global 3-D high-top climate model WACCM, with added *D* region ion chemistry. The addition of *D* region ion chemistry aims to better reproduce the effects of EPP in the mesosphere and upper stratosphere. *Andersson et al.* (2016) compared WACCM-D output and observations from Aura/MLS for a SPE in January 2005, and showed that the addition of ion chemistry significantly improved the modeling of polar HNO_3, HCl, ClO, OH, and NO_x compared to standard WACCM. The ions and ion reaction schemes included in WACCM-D are a subset of ions and reactions from the SIC model. Essential ions and reaction paths from SIC were chosen for inclusion into WACCM-D based on the analysis by *Verronen and Lehmann* (2013) to represent the effect of EPP on HO_x and NO_x. The model includes fully interactive chemistry, radiation, and dynamics, and has a vertical range from the Earth's

surface to the thermosphere (up to $\sim$140 km) with 88 vertical pressure levels. The vertical resolution varies from about 1.1 km in the troposphere to about 3.5 km in the mesosphere and lower thermosphere. The horizontal resolution is 1.9° in latitude and 2.5° in longitude. WACCM-D is run in Paper II with a preconfigured specified dynamics scenario, where the model dynamics are partially driven by meteorological fields. The specified dynamics force the model by 10% at altitudes below 50 km, while the dynamics are fully interactive above 60 km altitude. The forcing transitions linearly from 10% to no forcing between 50 and 60 km altitude.

The ionization sources used in the WACCM-D implementation of Paper II include solar protons, medium-energy electrons (MEE), auroral electrons, GCRs, Lyman α, and solar EUV. The auroral electrons, GCRs, Lyman α, and solar EUV forcing are standard WACCM ionization sources (for descriptions, see *Jackman et al.*, 2016; *Marsh et al.*, 2007; *Smith-Johnsen et al.*, 2018). The ionization rates for MEE are from the model by *van de Kamp et al.* (2016), which is based on electrons measurements from POES satellites and an empirically described structure of the plasmasphere. The model uses the *Dst* or the *Ap* index as an input, and calculates the energy-flux spectrum of precipitating electrons for energies from 30 to 1,000 keV with a time resolution of one day. The electrons from the MEE model precipitate into 16 geomagnetic latitude bins between 45° and 72°. The *Ap*-driven version of the MEE model was used in Paper II. Hourly SPE ionization rates are determined from GOES proton flux measurements using the method by *Vitt and Jackman* (1996). The same calculation method is used for the daily average SPE ionization rates in standard WACCM, as summarized by *Jackman* (2013). The SPE ionization rates are applied uniformly poleward of 60° geomagnetic latitude.

In Paper II, WACCM-D was used to model the atmospheric response to 62 SPEs that occurred between 2000 and 2005. Electron collision frequencies with N_2, O_2, O, and H were calculated from the WACCM-D output following *Banks and Kockarts* (1973, part A, pp.194). Differential CNA were then calculated from WACCM-D electron density and electron-neutral collision frequency with the method by *Sen and Wyller* (1960) for 16 different riometer stations, and integrated over the whole atmospheric column to produce the CNA estimates. The resulting modeled CNA were compared to observations from the riometer stations as a function of solar zenith angle and

geomagnetic latitude statistically, for each station statistically, and for each event and station individually.

The median average errors between WACCM-D and observed CNA over all 62 SPEs studied in Paper II are shown in panel a) of Figure 5.1 as a function of geomagnetic latitude and solar zenith angle. The CNA observations are from the riometer stations marked with the three letter abbreviations (see Paper II) and the field of view of each riometer is assumed to be $\pm 0.5°$ geomagnetic latitude. Overlapping parts of the fields of view are averaged together in the figure. As shown in Paper II and Figure 5.1, WACCM-D can reproduce the observed CNA well in sunlit and dark conditions, poleward of about 66° geomagnetic latitude, i.e., where the geomagnetic cutoff effect is negligible. The average absolute difference between WACCM-D and observations poleward of about 66° geomagnetic latitude is less than 0.5 dB. The differences between WACCM-D and observed CNA increase with decreasing geomagnetic latitude equatorward of 66° due to the lack of cutoffs and the medium-energy electron forcing used in the model. The average differences increase from about 0.5 dB to 1 dB in the geomagnetic latitude range of 66° to 60°. The southernmost station (JYV, 58.77° geomagnetic latitude) in Figure 5.1 is outside the area of proton forcing in the model, and the differences between the model and the observations are small. This indicates that, on average, most proton energies responsible for CNA are cut off at JYV. WACCM-D overestimates the level of CNA in twilight conditions, and the transition between night and day is more abrupt in WACCM-D than in the observations. In Figure 5.1, this is visible as increased median average errors in the solar zenith angle bins centered at 90° and 95°. The reason for the overestimation at twilight is the so called Earth shadow method used in WACCM-D (and other full-profile CNA models). In the Earth shadow method, the transition between night and day is a simple on/off at the solar terminator in the *D* region (at solar zenith angle 97°) that changes the effective recombination rate in the model ionosphere between night and day values. *Rogers et al.* (2016) presented similar results at twilight conditions with the SIC model, and concluded that the Earth shadow method cannot replicate the slowly varying ionospheric composition and temperature changes affecting CNA at presunset and especially postsunrise conditions. WACCM-D generally overestimates CNA compared to observations due to the lack of cutoff latitudes, the use of the daily

average MEE forcing, the Earth shadow method, and the riometer nonlinearity discussed in Section 4.1. This overestimation is easily explained, somewhat expected, and should occur in most or all events. Curiously, WACCM-D was found to underestimate (up to about 1.5 dB) the observed CNA in sunlit conditions in 18 of the 62 events at three or more GO-CANADA riometer stations poleward of 66° geomagnetic latitude. Geomagnetic activity, hardness of the SPE spectrum, season, and consecutively occurring SPEs were briefly examined as possible causes, but no explanation was found for this underestimation by WACCM-D. Further study is required to explain this unexpected result presented in Paper II.

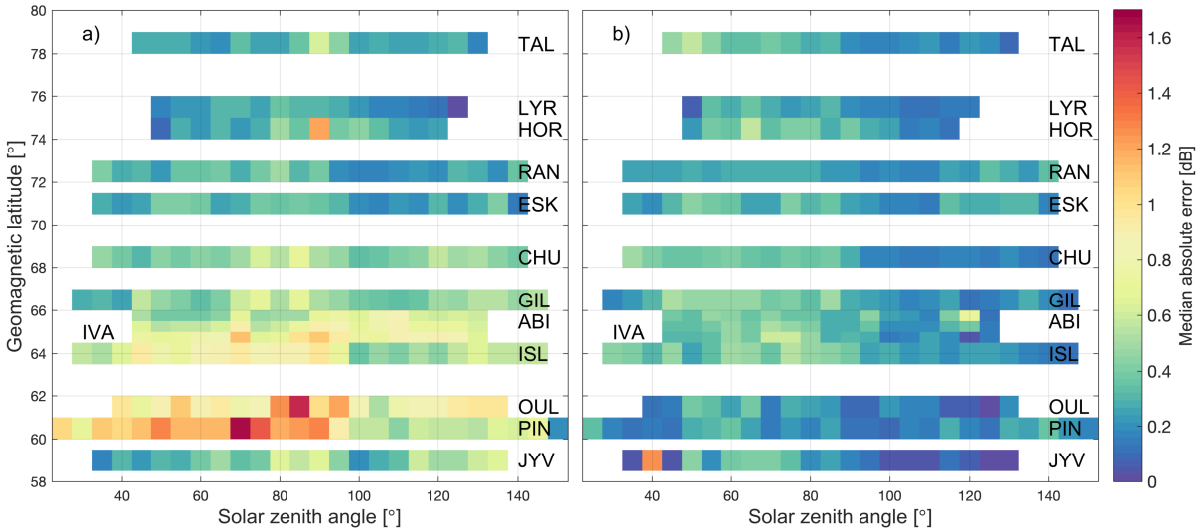

Figure 5.1: Median average errors between modeled and observed cosmic noise absorption over all 62 solar proton events studied in Paper II as a function of geomagnetic latitude and solar zenith angle. The WACCM-D model from Paper II is used in panel a) and the DRAP model with the *Dmitriev et al.* (2010) cutoff latitude model from Paper III is used in panel b). The different riometers are marked as three letter abbreviations next to their respected observations (see Paper II), and the field of view of each riometer is assumed to be $\pm 0.5°$ geomagnetic latitude.

Modeled and observed CNA (data from Papers II and III) at Island Lake (63.8° geomagnetic latitude, ISL in Figure 5.1) for a SPE in April 2002 are shown in Figure 5.2. Observed CNA is plotted in blue, modeled CNA from DRAP with the cutoff model by *Dmitriev et al.* (2010) is shown in orange (DRAP-DMI), modeled CNA from DRAP with the cutoff model by *Nesse Tyssøy and Stadsnes* (2015) is shown in yellow (DRAP-NTS), CNA calculated from the WACCM-D model output is plotted with a solid purple line, and nonlinearity corrected WACCM-D CNA (WACCM-D/NL) is plotted with the dashed purple line. The time resolution of the observations and the two DRAP versions is

five minutes, while the time resolution of the WACCM-D CNA is one hour. From 21 April, the sunrises and sunsets can be clearly seen as abrupt increases and decreases of CNA limiting the sunlit conditions, where the CNA values are far greater than in the dark conditions. The previously discussed overestimation of CNA by WACCM-D is clearly visible before, and through the whole event. The overestimation before the start of the event at 02:25 UT on 21 April 2002 is due to the MEE forcing, while the overestimation during the event is due to a combination of the lack of cutoffs, the used MEE forcing, and to a lesser extent, the nonlinearity at the highest CNA values. The abrupt twilight changes and the resulting CNA overestimation by WACCM-D are also visible at each sunset and sunrise in the figure. The nonlinearity correction was applied to the WACCM-D data by using the fitting parameter obtained for ISL in Paper II. As for most of the stations equatorward of 66° geomagnetic latitude in Paper II, the fit of the nonlinearity correction for ISL is fairly poor when cutoff latitudes and solar zenith angle are not taken into account in the fitting. As the nonlinearity correction was fitted with WACCM-D data without geomagnetic cutoffs, the method tries to correct for the overestimation of CNA by the lack of cutoff latitudes and the nonlinearity of the riometer, instead of just the nonlinearity.

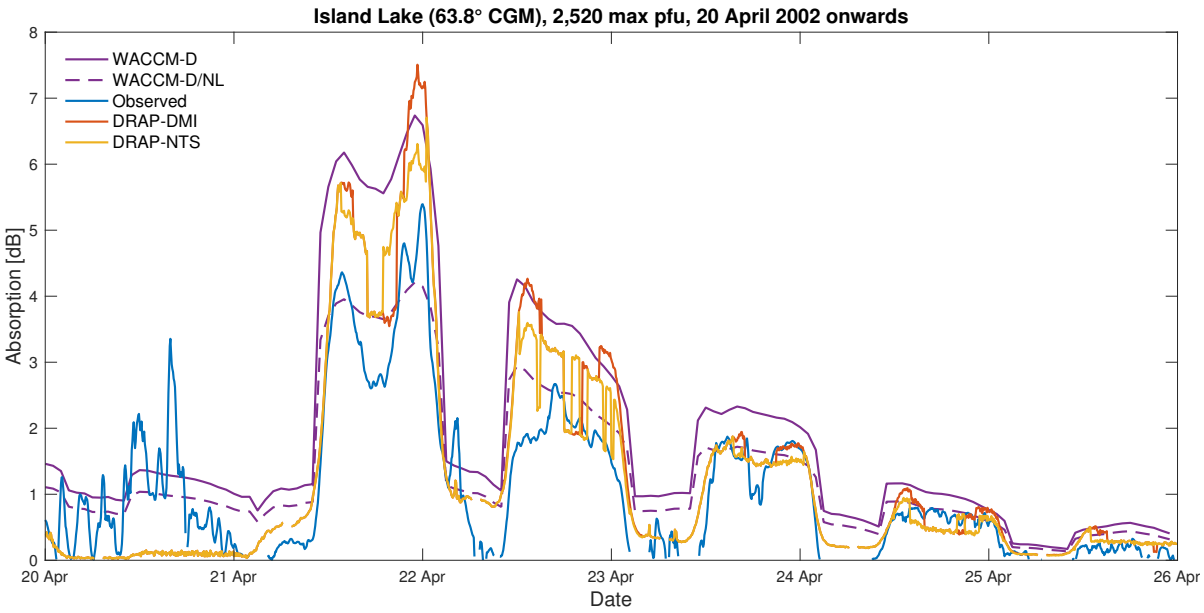

Figure 5.2: Modeled and observed cosmic noise absorption (CNA) at Island Lake during a solar proton event starting at 02:25 UT on 21 April 2002. Observed CNA is shown in blue, DRAP with the cutoff model by *Dmitriev et al.* (2010) is shown in orange, DRAP with the cutoff model by *Nesse Tyssøy and Stadsnes* (2015) is shown in yellow, CNA calculated from WACCM-D is shown in a purple solid line, and nonlinearity corrected from WACCM-D is shown with a purple dashed line.

Modeled CNA using the two cutoff models are almost identical in dark and twilight conditions during the example event shown in Figure 5.2. Differences between the two cutoff models are larger in sunlit conditions, but neither of the models performs systematically better in the example event. During the first day of the event, both cutoff models capture the poleward movement of the cutoff latitudes and reduction in CNA around local midday, although the duration of the reduction is longer with the *Dmitriev et al.* (2010) model. Both models predict reductions of CNA around the local midday that are not present in the observations during the second and fourth day of the event. During the third day, the *Dmitriev et al.* (2010) model predicts a reduction in CNA around local midday that matches the observations in time, while the model by *Nesse Tyssøy and Stadsnes* (2015) predicts no such reduction.

The median average errors between DRAP with the *Dmitriev et al.* (2010) model and observed CNA over all 62 SPEs studied in Paper II are shown in panel b) of Figure 5.1 with the same format as panel a). The data in panel b) are from Paper III, but two stations (LYR and HOR) have been added and the data has been averaged to one hour time resolution. The median absolute errors with the DRAP model using cutoff latitudes are significantly lower than those with the WACCM-D model equatorward of about 66° geomagnetic latitude. Some of the differences in median absolute errors of the two models are due to the additional ionization sources in WACCM-D. This is especially the case in dark conditions (solar zenith angle $\gtrsim$100°), where the medium-energy electrons in WACCM-D contribute significantly to the modeled CNA. Although the median absolute errors from the two models cannot be directly compared due to the different modeling approaches and ionization forcings, the difference is striking equatorward of about 66° geomagnetic latitude, and highlights the effect of geomagnetic cutoffs.

5.2 Spatial estimation of solar proton event impact

The relationship between CNA and integral proton flux can be used as an indicator of SPE impact area. As the response of CNA to precipitating protons varies with the energy and flux of protons, and the solar zenith angle (see Section 4.1), riometer observations are biased towards a certain energy range and are most useful in sunlit

conditions. In the case of wide-beam riometers, the beam covers a large area in the *D* region, which is integrated over the field of view into a single value, and the effects of geomagnetic cutoffs are muted. Despite these drawbacks, riometers can provide a good estimate of the spatial extent of SPEs because of the large spatial coverage of deployed riometers.

In the averaged comparison of WACCM-D CNA and observations presented in Paper II, the effect of geomagnetic cutoffs are visible equatorward of about 66° geomagnetic latitude in sunlit conditions. The largest differences between the model and the observations are at the most equatorward stations within the 60° geomagnetic latitude proton forcing limit of the model. A comparison of sunlit CNA observations and the DRAP model without cutoff latitudes produced similar results in Paper III. Based on the results of Papers II and III, the static 60° geomagnetic latitude proton forcing limit significantly overestimates the impact area of the SPEs on average. The same static 60° limit for the uniform proton precipitation is used in most model studies (e.g., *Baumgaertner et al.*, 2010; *Jackman et al.*, 2000, 2005, 2007, 2009; *Rozanov et al.*, 2012; *Sinnhuber et al.*, 2018) and also in the solar forcing recommendation for the sixth Coupled Model Intercomparison Project (CMIP6, *Matthes et al.*, 2017).

The spatial extent of the SPE impact area compared to the static 60° limit was estimated in Paper III using the *Dmitriev et al.* (2010) cutoff latitude model. The estimation was done by calculating the ratio of the area of the spherical cap bound by the cutoff latitude ellipse from the *Dmitriev et al.* (2010) model and the spherical cap limited by 60° geomagnetic latitude. This calculation was performed for 4, 8, 16, and 32 MeV cutoff latitudes at each 5 min time step of all 73 SPEs studied in the paper. The spatial extent of proton precipitation at these energies is overestimated 90% of the total event time, and the median overestimation of the spatial extent is between 15% and 26% depending on cutoff energy. As the *Dmitriev et al.* (2010) model predicts unrealistically low cutoff latitudes during extremely disturbed geomagnetic conditions, the given spatial and temporal overestimation percentages are conservative values.

Nesse Tyssøy et al. (2013) determined that geomagnetic cutoffs are not present in GOES proton flux measurements, and that using GOES fluxes leads to an overestimation of energy deposition into the atmosphere compared to using precipitating fluxes observed by POES. During the main phase of the SPE on 23 January 2012, the en-

ergy deposition overestimation at 70 km altitude is 50–100%, at and equatorward of 67° geomagnetic latitude on the dayside (*Nesse Tyssøy et al.*, 2013), and 25% at 68° and 64° geomagnetic latitude on the dayside and nightside, respectively (*Nesse Tyssøy and Stadsnes*, 2015). The total energy input overestimation during the event using GOES proton fluxes was 20–30% poleward of 60° geomagnetic latitude (*Nesse Tyssøy et al.*, 2013). *Nesse Tyssøy and Stadsnes* (2015) also noted that most events they studied had stronger day-night cutoff latitude asymmetry than the SPE on 23 January 2012 and that the asymmetry in the event was by no means extreme.

In order to model the atmospheric effects of SPEs more accurately, the SPE forcing in climate and other atmospheric models should be upgraded to include the geomagnetic cutoff effect. This is especially important in studies of short timescale effects of SPEs. The atmospheric impact of SPEs can be used as a reference when studying other EEP ionization, or the combined effect of EPP and dynamical events such as sudden stratospheric warmings, as it is the best understood EPP source, and the occurrence times and particle fluxes at geostationary orbit are known. At time scales of more than a few months, the proton forcing overestimation should not be noticeable, as the simulated impact of SPEs on polar annual mean total ozone and temperature have been reported to be insignificant (*Jackman et al.*, 2009).

SPEs cause large-scale ionization and chemical changes in the middle atmosphere, but occur rarely compared to EEP, so it is possible that the atmospheric effect of EEP dominates at longer timescales. *Rodger et al.* (2010) used the SIC model to study the atmospheric response to a single large geomagnetic storm and reported mesospheric ozone losses that were fairly similar in magnitude, timescale, and altitude to those from previous modeling and observational studies of large SPEs. *Seppälä et al.* (2015) modeled a 5-day period with 61 substorms using the SIC model. The resulting mesospheric ozone loss was similar in scale to a small to medium SPE. Contrary to EEP, SPEs ionize the atmosphere to lower altitudes and affect the whole polar cap. The chemical changes from SPEs occur inside the polar vortex, while at least some of the outer radiation belt electrons precipitate outside the polar vortex reducing the EPP indirect effect and making the direct contrasting of EEP and SPE effects more difficult (*Rodger et al.*, 2010). Tagging and tracing NO_x and the resulting ozone loss by different sources of EPP in a solar-cycle-length climate model run would give a good estimate on the

relative importance of the different EPP sources causing the EPP indirect effect. To my knowledge, no such study has been published by September 2019, but preliminary results have been presented at conferences.

6

Future work

The atmospheric, and especially climate impacts of EPP have been of increasing interest in the recent years, as the role of EPP as a source of climate variability, and the need to include EPP forcing in climate models have been recognized. The current aim of the research community is to understand the link between EPP and its atmospheric and climate effects in greater detail, and to develop accurate EPP forcing for use in climate models.

Based on the research presented in this thesis, applying geomagnetic cutoffs into currently used proton forcing would be an important step forward to model the atmospheric impacts of SPEs with greater accuracy. The logical continuation of this research is to apply a cutoff latitude model into the commonly used proton forcing by *Jackman* (2013) and test the forcing with WACCM-D. The cutoff latitude model by *Dmitriev et al.* (2010) was found to be a suitable cutoff latitude model candidate for this purpose, but some improvements are required in the model for extreme geomagnetic activity. The upgraded proton forcing would better enable the study of other ionization sources by providing a more realistic atmospheric effect of SPEs in models. Possible topics for future study could be, for example, the contribution of electrons to atmospheric ionization during SPEs, the relative importances of different EPP sources, and the sensitivity of the middle atmosphere to different types of EPP. Work on this topic has already started as a part of the Norwegian Research Council funded project, “Which types of particle precipitation matter in the matter atmosphere?”.

Combining modeling results and observations from one, or more, instrument types is often necessary to obtain a more complete picture of the studied phenomena and the background conditions. When using riometers, their nonlinearity to high absorption values should be taken into account, and the nonlinearity correction presented in this thesis provides a good starting point for this. The nonlinearity correction method still needs more testing, and the logical next step would be to test it by using modeled CNA data that includes the effect of geomagnetic cutoff for the fitting.

The estimation of radio wave attenuation with the SuperDARN radars can provide a good supplementary data set for future studies. The attenuation estimation method can also be used for diagnosing SuperDARN backscatter loss, and it highlights the possibility of using routine SuperDARN background noise measurements for scientific use. A combination of background noise measurements and instantaneous echo occurrence has been used to determine occurrence rates of EEP by *Bland et al.* (2019), and the goal is to automate the observation of radio wave attenuation and EEP detection with SuperDARN in the future.

Bibliography

Aggarwal, K., N. Nath, and C. Setty (1979), Collision frequency and transport properties of electrons in the ionosphere, *Planetary and Space Science*, *27*(6), 753–768, doi:10.1016/0032-0633(79)90004-7.

Akmaev, R. A. (2010), D-RAP Model Validation: I. Scientific Report, Retrieved from `https://www.ngdc.noaa.gov/stp/drap/DRAP-V-Report1.pdf`.

Andersson, M. E., P. T. Verronen, C. J. Rodger, M. A. Clilverd, and A. Seppälä (2014), Missing driver in the Sun–Earth connection from energetic electron precipitation impacts mesospheric ozone, *Nature Communications*, *5*(5197), doi:10.1038/ncomms6197.

Andersson, M. E., P. T. Verronen, D. R. Marsh, S.-M. Päivärinta, and J. M. C. Plane (2016), WACCM-D—Improved modeling of nitric acid and active chlorine during energetic particle precipitation, *Journal of Geophysical Research: Atmospheres*, *121*(17), 10,328–10,341, doi:10.1002/2015JD024173.

Andersson, M. E., P. T. Verronen, D. R. Marsh, A. Seppälä, S.-M. Päivärinta, C. J. Rodger, M. A. Clilverd, N. Kalakoski, and M. van de Kamp (2018), Polar ozone response to energetic particle precipitation over decadal time scales: The role of medium-energy electrons, *Journal of Geophysical Research: Atmospheres*, *123*(1), 607–622, doi:10.1002/2017JD027605.

Arsenovic, P., E. Rozanov, A. Stenke, B. Funke, J. M. Wissing, K. Mursula, F. Tummon, and T. Peter (2016), The influence of middle range energy electrons on atmospheric chemistry and regional climate, *Journal of Atmospheric and Solar-Terrestrial Physics*, *149*, 180–190, doi:10.1016/j.jastp.2016.04.008.

Axford, W. I., and G. C. Reid (1963), Increases in intensity of solar cosmic rays before sudden commencements of geomagnetic storms, *Journal of Geophysical Research*, *68*(7), 1,793–1,803, doi:10.1029/JZ068i007p01793.

Bailey, D. (1964), Polar-cap absorption, *Planetary and Space Science*, *12*(5), 495–541, doi:10.1016/0032-0633(64)90040-6.

Bailey, D. K. (1957), Disturbances in the lower ionosphere observed at VHF following the solar flare of 23 February 1956 with particular reference to auroral-zone absorption, *Journal of Geophysical Research*, *62*(3), 431–463, doi:10.1029/JZ062i003p00431.

Baker, M. B., A. J. Masley, and P. R. Satterblom (1973), Simultaneous satellite and riometer studies, in *International Cosmic Ray Conference*, *International Cosmic Ray Conference*, vol. 2, pp. 1,440.

Banks, P. M., and G. Kockarts (1973), *Aeronomy*, vol. A, Elsevier, New York, doi:10.1016/C2013-0-10328-5.

Bates, D. R., and M. Nicolet (1950), The photochemistry of atmospheric water vapor, *Journal of Geophysical Research*, *55*(3), 301–327, doi:10.1029/JZ055i003p00301.

Baumgaertner, A. J. G., P. Jöckel, H. Riede, G. Stiller, and B. Funke (2010), Energetic particle precipitation in ECHAM5/MESSy — Part 2: Solar proton events, *Atmospheric Chemistry and Physics*, *10*(15), 7,285–7,302, doi:10.5194/acp-10-7285-2010.

Baumgaertner, A. J. G., A. Seppälä, P. Jöckel, and M. A. Clilverd (2011), Geomagnetic activity related NO_x enhancements and polar surface air temperature variability in a chemistry climate model: Modulation of the NAM index, *Atmospheric Chemistry and Physics*, *11*(9), 4,521–4,531, doi:10.5194/acp-11-4521-2011.

Berngardt, O. I., J. M. Ruohoniemi, N. Nishitani, S. G. Shepherd, W. A. Bristow, and E. S. Miller (2018), Attenuation of decameter wavelength sky noise during x-ray solar flares in 2013–2017 based on the observations of midlatitude HF radars, *Journal of Atmospheric and Solar-Terrestrial Physics*, *173*, 1–13, doi:10.1016/j.jastp.2018.03.022.

Berngardt, O. I., J. M. Ruohoniemi, J. St-Maurice, A. Marchaudon, M. J. Kosch, A. S. Yukimatu, N. Nishitani, S. G. Shepherd, M. F. Marcucci, H. Hu, T. Nagatsuma, and M. Lester (2019), Global diagnostics of ionospheric absorption during X-ray solar flares based on 8- to 20-MHz noise measured by over-the-horizon radars, *Space Weather*, *17*(6), 907–924, doi:10.1029/2018SW002130.

Birch, M. J., J. K. Hargreaves, A. Senior, and B. J. I. Bromage (2005), Variations in cutoff latitude during selected solar energetic proton events, *Journal of Geophysical Research: Space Physics*, *110*(A7), A07221, doi:10.1029/2004JA010833.

Blake, J., M. McNab, and J. Mazur (2001), Solar-proton polar-cap intensity structures as a test of magnetic field models, *Advances in Space Research*, *28*(12), 1,753–1,757, doi:10.1016/S0273-1177(01)00542-7.

Bland, E. C., N. Partamies, E. Heino, A. S. Yukimatu, and H. Miyaoka (2019), Energetic electron precipitation occurrence rates determined using the Syowa East SuperDARN radar, *Journal of Geophysical Research: Space Physics*, *124*(7), 6,253–6,265, doi:10.1029/2018JA026437.

Brasseur, G. P., and S. Solomon (2006), *Aeronomy of the middle atmosphere: Chemistry and physics of the stratosphere and mesosphere*, vol. 32, Springer Science & Business Media.

Browne, S., J. Hargreaves, and B. Honary (1995), An imaging riometer for ionospheric studies, *Electronics & Communication Engineering Journal*, *7*(5), 209–217, doi:10.1049/ecej:19950505.

Chakraborty, S., J. B. H. Baker, J. M. Ruohoniemi, B. Kunduri, N. Nishitani, and S. G. Shepherd (2019), A study of SuperDARN response to co-occurring space weather phenomena, *Space Weather*, *17*, doi:10.1029/2019SW002179.

Chisham, G., M. Lester, S. E. Milan, M. P. Freeman, W. A. Bristow, A. Grocott, K. A. McWilliams, J. M. Ruohoniemi, T. K. Yeoman, P. L. Dyson, R. A. Greenwald, T. Kikuchi, M. Pinnock, J. P. S. Rash, N. Sato, G. J. Sofko, J.-P. Villain, and A. D. M. Walker (2007), A decade of the Super Dual Auroral Radar Network (SuperDARN): Scientific achievements, new techniques and future directions, *Surveys in Geophysics*, *28*(1), 33–109, doi:10.1007/s10712-007-9017-8.

Clilverd, M. A., C. J. Rodger, T. Moffat-Griffin, and P. T. Verronen (2007), Improved dynamic geomagnetic rigidity cutoff modeling: Testing predictive accuracy, *Journal of Geophysical Research: Space Physics*, *112*, A08302, doi:10.1029/2007JA012410.

Crutzen, P. J., I. S. A. Isaksen, and G. C. Reid (1975), Solar proton events: Stratospheric sources of nitric oxide, *Science*, *189*(4201), 457–459, doi:10.1126/science.189.4201.457.

Denton, M. H., R. Kivi, T. Ulich, M. A. Clilverd, C. J. Rodger, and P. von der Gathen (2018), Northern Hemisphere stratospheric ozone depletion caused by solar proton events: The role of the polar vortex, *Geophysical Research Letters*, *45*(4), 2,115–2,124, doi:10.1002/2017GL075966, 2017GL075966.

Dmitriev, A. V., P. T. Jayachandran, and L.-C. Tsai (2010), Elliptical model of cutoff boundaries for the solar energetic particles measured by POES satellites in December 2006, *Journal of Geophysical Research: Space Physics*, *115*(A12), A12244, doi:10.1029/2010JA015380.

Evans, J. V., and T. Hagfors (1968), *Radar Astronomy*, McGraw-Hill.

Fanselow, J. L., and E. C. Stone (1972), Geomagnetic cutoffs for cosmic-ray protons for seven energy intervals between 1.2 and 39 MeV, *Journal of Geophysical Research*, *77*(22), 3,999–4,009, doi:10.1029/JA077i022p03999.

Forbush, S. E. (1946), Three unusual cosmic-ray increases possibly due to charged particles from the sun, *Phys. Rev.*, *70*, 771–772, doi:10.1103/PhysRev.70.771.

Freier, P. S., E. P. Ney, and J. R. Winckler (1959), Balloon observation of solar cosmic rays on March 26, 1958, *Journal of Geophysical Research*, *64*(6), 685–688, doi:10.1029/JZ064i006p00685.

Funke, B., A. Baumgaertner, M. Calisto, T. Egorova, C. H. Jackman, J. Kieser, A. Krivolutsky, M. López-Puertas, D. R. Marsh, T. Reddmann, E. Rozanov, S.-M. Salmi, M. Sinnhuber, G. P. Stiller, P. T. Verronen, S. Versick, T. von Clarmann, T. Y. Vyushkova, N. Wieters, and J. M. Wissing (2011), Composition changes after the "Halloween" solar proton event: the High Energy Particle Precipitation in the Atmosphere (HEPPA) model versus MIPAS data intercomparison study, *Atmospheric Chemistry and Physics*, *11*(17), 9,089–9,139, doi:10.5194/acp-11-9089-2011.

Funke, B., M. López-Puertas, G. P. Stiller, and T. von Clarmann (2014), Mesospheric and stratospheric NO_y produced by energetic particle precipitation during 2002–

2012, *Journal of Geophysical Research: Atmospheres*, *119*(7), 4,429–4.446, doi:10.1002/2013JD021404.

Gray, L. J., J. Beer, M. Geller, J. D. Haigh, M. Lockwood, K. Matthes, U. Cubasch, D. Fleitmann, G. Harrison, L. Hood, J. Luterbacher, G. A. Meehl, D. Shindell, B. van Geel, and W. White (2010), Solar influences on the climate, *Reviews of Geophysics*, *48*(4), doi:10.1029/2009RG000282.

Greenwald, R. A., K. B. Baker, J. R. Dudeney, M. Pinnock, T. B. Jones, E. C. Thomas, J. P. Villain, J. C. Cerisier, C. Senior, C. Hanuise, R. D. Hunsucker, G. Sofko, J. Koehler, E. Nielsen, R. Pellinen, A. D. M. Walker, N. Sato, and H. Yamagishi (1995), DARN/SuperDARN, *Space Science Reviews*, *71*(1), 761–796, doi:10.1007/BF00751350.

Hargreaves, J. K., and D. L. Detrick (2002), Application of polar cap absorption events to the calibration of riometer systems, *Radio Science*, *37*(3), 1–11, doi:10.1029/2001RS002465.

Hedin, A. E. (1991), Extension of the MSIS thermosphere model into the middle and lower atmosphere, *Journal of Geophysical Research: Space Physics*, *96*(A2), 1,159–1,172, doi:10.1029/90JA02125.

Hunsucker, R. D., and J. K. Hargreaves (2002), *The High-Latitude Ionosphere and its Effects on Radio Propagation*, Cambridge Atmospheric and Space Science Series, Cambridge University Press, doi:10.1017/CBO9780511535758.

Jackman, C. H. (2013), Ionization rates for 1963–2012 from solar proton events, Retrieved from `http://solarisheppa.geomar.de/solarisheppa/sites/default/files/data/SOLARIS_Jackman_SPEs.pdf`.

Jackman, C. H., E. L. Fleming, and F. M. Vitt (2000), Influence of extremely large solar proton events in a changing stratosphere, *Journal of Geophysical Research: Atmospheres*, *105*(D9), 11,659–11,670, doi:10.1029/2000JD900010.

Jackman, C. H., R. D. McPeters, G. J. Labow, E. L. Fleming, C. J. Praderas, and J. M. Russell (2001), Northern Hemisphere atmospheric effects due to the July 2000 Solar Proton Event, *Geophysical Research Letters*, *28*(15), 2,883–2,886, doi:10.1029/2001GL013221.

Jackman, C. H., M. T. DeLand, G. J. Labow, E. L. Fleming, D. K. Weisenstein, M. K. Ko, M. Sinnhuber, J. Anderson, and J. M. Russell (2005), The influence of the several very large solar proton events in years 2000–2003 on the neutral middle atmosphere, *Advances in Space Research*, *35*(3), 445–450, doi:10.1016/j.asr.2004.09.006.

Jackman, C. H., R. G. Roble, and E. L. Fleming (2007), Mesospheric dynamical changes induced by the solar proton events in October–November 2003, *Geophysical Research Letters*, *34*(4), L04812, doi:10.1029/2006GL028328.

Jackman, C. H., D. R. Marsh, F. M. Vitt, R. R. Garcia, E. L. Fleming, G. J. Labow, C. E. Randall, M. López-Puertas, B. Funke, T. von Clarmann, and G. P. Stiller (2008), Short- and medium-term atmospheric constituent effects of very large solar proton events, *Atmospheric Chemistry and Physics*, *8*(3), 765–785, doi:10.5194/acp-8-765-2008.

Jackman, C. H., D. R. Marsh, F. M. Vitt, R. R. Garcia, C. E. Randall, E. L. Fleming, and S. M. Frith (2009), Long-term middle atmospheric influence of very large solar proton events, *Journal of Geophysical Research: Atmospheres*, *114*, D11304, doi:10.1029/2008JD011415.

Jackman, C. H., D. R. Marsh, D. E. Kinnison, C. J. Mertens, and E. L. Fleming (2016), Atmospheric changes caused by galactic cosmic rays over the period 1960–2010, *Atmospheric Chemistry and Physics*, *16*(9), 5,853–5,866, doi:10.5194/acp-16-5853-2016.

Kallenrode, M.-B. (2003), Current views on impulsive and gradual solar energetic particle events, *Journal of Physics G: Nuclear Physics*, *29*, 965–981, doi:10.1088/0954-3899/29/5/316.

Kavanagh, A., S. Marple, F. Honary, I. McCrea, and A. Senior (2004), On solar protons and polar cap absorption: Constraints on an empirical relationship, *Annales Geophysicae*, *22*, 1,133–1,147, doi:10.5194/angeo-22-1133-2004.

Kress, B. T., C. J. Mertens, and M. Wiltberger (2010), Solar energetic particle cutoff variations during the 29–31 October 2003 geomagnetic storm, *Space Weather*, *8*(5), S05001, doi:10.1029/2009SW000488.

Kyrölä, E., M. E. Andersson, P. T. Verronen, M. Laine, S. Tukiainen, and D. R. Marsh (2018), Middle atmospheric ozone, nitrogen dioxide and nitrogen trioxide in 2002–

2011: SD-WACCM simulations compared to GOMOS observations, *Atmospheric Chemistry and Physics*, *18*(7), 5,001–5,019, doi:10.5194/acp-18-5001-2018.

Lary, D. J. (1997), Catalytic destruction of stratospheric ozone, *Journal of Geophysical Research: Atmospheres*, *102*(D17), 21,515–21,526, doi:10.1029/97JD00912.

Leske, R. A., R. A. Mewaldt, E. C. Stone, and T. T. von Rosenvinge (2001), Observations of geomagnetic cutoff variations during solar energetic particle events and implications for the radiation environment at the space station, *Journal of Geophysical Research: Space Physics*, *106*(A12), 30,011–30,022, doi:10.1029/2000JA000212.

Lester, M. (2013), The Super Dual Auroral Radar Network (SuperDARN): An overview of its development and science, *Advances in Polar Science*, *24*(1), 1–11, doi:10.3724/SP.J.1085.2013.00001.

Lilensten, J., T. De Wit, K. Matthes, and European Cooperation in the Field of Scientific and Technical Research (Organization) (2015), *Earth's Climate Response to a Changing Sun*, Hors Collection, EDP Sciences, doi:10.1051/978-2-7598-1733-7.

Little, C. G., and H. Leinbach (1958), Some measurements of high-latitude ionospheric absorption using extraterrestrial radio waves, *Proceedings of the IRE*, *46*(1), 334–348, doi:10.1109/JRPROC.1958.286795.

Little, C. G., and H. Leinbach (1959), The Riometer—A device for the continuous measurement of ionospheric absorption, *Proceedings of the IRE*, *47*(2), 315–320, doi:10.1109/JRPROC.1959.287299.

Marsh, D. R., R. R. Garcia, D. E. Kinnison, B. A. Boville, F. Sassi, S. C. Solomon, and K. Matthes (2007), Modeling the whole atmosphere response to solar cycle changes in radiative and geomagnetic forcing, *Journal of Geophysical Research: Atmospheres*, *112*, D23306, doi:10.1029/2006JD008306.

Marsh, D. R., M. J. Mills, D. E. Kinnison, J.-F. Lamarque, N. Calvo, and L. M. Polvani (2013), Climate change from 1850 to 2005 simulated in CESM1(WACCM), *Journal of Climate*, *26*(19), 7,372–7,391, doi:10.1175/JCLI-D-12-00558.1.

Matthes, K., B. Funke, M. E. Andersson, L. Barnard, J. Beer, P. Charbonneau, M. A. Clilverd, T. Dudok de Wit, M. Haberreiter, A. Hendry, C. H. Jackman, M. Kretzschmar,

T. Kruschke, M. Kunze, U. Langematz, D. R. Marsh, A. C. Maycock, S. Misios, C. J. Rodger, A. A. Scaife, A. Seppälä, M. Shangguan, M. Sinnhuber, K. Tourpali, I. Usoskin, M. van de Kamp, P. T. Verronen, and S. Versick (2017), Solar forcing for CMIP6 (v3.2), *Geoscientific Model Development*, *10*(6), 2,247–2,302, doi:10.5194/gmd-10-2247-2017.

Milan, S. E., T. B. Jones, T. R. Robinson, E. C. Thomas, and T. K. Yeoman (1997a), Interferometric evidence for the observation of ground backscatter originating behind the CUTLASS coherent HF radars, *Annales Geophysicae*, *15*(1), 29–39, doi: 10.1007/s00585-997-0029-y.

Milan, S. E., T. K. Yeoman, M. Lester, E. C. Thomas, and T. B. Jones (1997b), Initial backscatter occurrence statistics from the CUTLASS HF radars, *Annales Geophysicae*, *15*(6), 703–718, doi:10.1007/s00585-997-0703-0.

Neal, J. J., C. J. Rodger, and J. C. Green (2013), Empirical determination of solar proton access to the atmosphere: Impact on polar flight paths, *Space Weather*, *11*(7), 420–433, doi:10.1002/swe.20066.

Nesse Tyssøy, H., and J. Stadsnes (2015), Cutoff latitude variation during solar proton events: Causes and consequences, *Journal of Geophysical Research: Space Physics*, *120*(1), 553–563, doi:10.1002/2014JA020508.

Nesse Tyssøy, H., J. Stadsnes, F. Søraas, and M. Sørbø (2013), Variations in cutoff latitude during the January 2012 solar proton event and implication for the distribution of particle energy deposition, *Geophysical Research Letters*, *40*(16), 4,149–4,153, doi: 10.1002/grl.50815.

Newnham, D. A., M. A. Clilverd, C. J. Rodger, K. Hendrickx, L. Megner, A. J. Kavanagh, A. Seppälä, P. T. Verronen, M. E. Andersson, D. R. Marsh, T. Kovács, W. Feng, and J. M. C. Plane (2018), Observations and modeling of increased nitric oxide in the Antarctic polar middle atmosphere associated with geomagnetic gtorm-driven energetic electron precipitation, *Journal of Geophysical Research: Space Physics*, *123*(7), 6,009–6,025, doi:10.1029/2018JA025507.

Obayashi, T., and Y. Hakura (1960), Enhanced ionization in the polar ionosphere associated with geomagnetic storms, *Journal of Atmospheric and Terrestrial Physics*, *18*(2), 101–122, doi:10.1016/0021-9169(60)90082-9.

Ogliore, R. C., R. A. Mewaldt, R. A. Leske, E. C. Stone, and T. T. von Rosenvinge (2001), A direct measurement of the geomagnetic cutoff for cosmic rays at space station latitudes, *International Cosmic Ray Conference*, *10*, 4,112.

Patterson, J. D., T. P. Armstrong, C. M. Laird, D. L. Detrick, and A. T. Weatherwax (2001), Correlation of solar energetic protons and polar cap absorption, *Journal of Geophysical Research: Space Physics*, *106*(A1), 149–163, doi:10.1029/2000JA002006.

Pettit, J., C. E. Randall, D. R. Marsh, C. G. Bardeen, L. Qian, C. H. Jackman, T. N. Woods, A. Coster, and V. L. Harvey (2018), Effects of the September 2005 solar flares and solar proton events on the middle atmosphere in WACCM, *Journal of Geophysical Research: Space Physics*, *123*(7), 5,747–5,763, doi:10.1029/2018JA025294.

Ponomarenko, V., Pavlo, B. Iserhienrhien, and J.-P. St.-Maurice (2016), Morphology and possible origins of near-range oblique HF backscatter at high and midlatitudes, *Radio Science*, *51*(6), 718–730, doi:10.1002/2016RS006088.

Porter, H. S., C. H. Jackman, and A. E. S. Green (1976), Efficiencies for production of atomic nitrogen and oxygen by relativistic proton impact in air, *The Journal of Chemical Physics*, *65*(1), 154–167, doi:10.1063/1.432812.

Potemra, T. A. (1972), The empirical connection of riometer absorption to solar protons during PCA events, *Radio Science*, *7*(5), 571–577, doi:10.1029/RS007i005p00571.

Potemra, T. A., and A. J. Zmuda (1972), Solar electrons and alpha particles during polar-cap absorption events, *Journal of Geophysical Research*, *77*(34), 6,916–6,921, doi:10.1029/JA077i034p06916.

Randall, C. E., D. E. Siskind, and R. M. Bevilacqua (2001), Stratospheric NO_x enhancements in the Southern Hemisphere vortex in winter/spring of 2000, *Geophysical Research Letters*, *28*(12), 2,385–2,388, doi:10.1029/2000GL012746.

Randall, C. E., V. L. Harvey, C. S. Singleton, S. M. Bailey, P. F. Bernath, M. Codrescu, H. Nakajima, and J. M. Russell III (2007), Energetic particle precipitation effects on the southern hemisphere stratosphere in 1992–2005, *Journal of Geophysical Research: Atmospheres*, *112*(D8), doi:10.1029/2006JD007696.

Reames, D. V. (2013), The two sources of solar energetic particles, *Space Science Reviews*, *175*(1), 53–92, doi:10.1007/s11214-013-9958-9.

Reid, G., and H. Leinbach (1961), Morphology and interpretation of the great polar cap absorption events of May and July, 1959, *Journal of Atmospheric and Terrestrial Physics*, *23*, 216–228, doi:10.1016/0021-9169(61)90047-2.

Rodger, C. J., M. A. Clilverd, P. T. Verronen, T. Ulich, M. J. Jarvis, and E. Turunen (2006), Dynamic geomagnetic rigidity cutoff variations during a solar proton event, *Journal of Geophysical Research: Space Physics*, *111*, A04222, doi:10.1029/2005JA011395.

Rodger, C. J., M. A. Clilverd, A. Seppälä, N. R. Thomson, R. J. Gamble, M. Parrot, J.-A. Sauvaud, and T. Ulich (2010), Radiation belt electron precipitation due to geomagnetic storms: Significance to middle atmosphere ozone chemistry, *Journal of Geophysical Research: Space Physics*, *115*, A11320, doi:10.1029/2010JA015599.

Rogers, N. C., and F. Honary (2015), Assimilation of real-time riometer measurements into models of 30 MHz polar cap absorption, *Journal of Space Weather and Space Climate*, *5*(27), A8, doi:10.1051/swsc/2015009.

Rogers, N. C., A. Kero, F. Honary, P. T. Verronen, E. M. Warrington, and D. W. Danskin (2016), Improving the twilight model for polar cap absorption nowcasts, *Space Weather*, *14*(11), 950–972, doi:10.1002/2016SW001527.

Rosenberg, T. J., D. L. Detrick, D. Venkatesan, and G. van Bavel (1991), A comparative study of imaging and broad-beam riometer measurements: The effect of spatial structure on the frequency dependence of auroral absorption, *Journal of Geophysical Research: Space Physics*, *96*(A10), 17,793–17,803, doi:10.1029/91JA01827.

Rozanov, E., L. Callis, M. Schlesinger, F. Yang, N. Andronova, and V. Zubov (2005), Atmospheric response to NO_y source due to energetic electron precipitation, *Geophysical Research Letters*, *32*(14), L14811, doi:10.1029/2005GL023041.

Rozanov, E., M. Calisto, T. Egorova, T. Peter, and W. Schmutz (2012), Influence of the precipitating energetic particles on atmospheric chemistry and climate, *Surveys in Geophysics*, *33*(3), 483–501, doi:10.1007/s10712-012-9192-0.

Sauer, H. H., and D. C. Wilkinson (2008), Global mapping of ionospheric HF/VHF radio wave absorption due to solar energetic protons, *Space Weather*, *6*(12), S12002, doi:10.1029/2008SW000399.

Sellers, B., F. A. Hanser, M. A. Stroscio, and G. K. Yates (1977), The night and day relationships between polar cap riometer absorption and solar protons, *Radio Science*, *12*(5), 779–789, doi:10.1029/RS012i005p00779.

Sen, H. K., and A. A. Wyller (1960), On the generalization of the Appleton-Hartree magnetoionic formulas, *Journal of Geophysical Research*, *65*(12), 3,931–3,950, doi:10.1029/JZ065i012p03931.

Seppälä, A., P. T. Verronen, E. Kyrölä, S. Hassinen, L. Backman, A. Hauchecorne, J. L. Bertaux, and D. Fussen (2004), Solar proton events of October–November 2003: Ozone depletion in the Northern Hemisphere polar winter as seen by GOMOS/Envisat, *Geophysical Research Letters*, *31*, L19107, doi:10.1029/2004GL021042.

Seppälä, A., C. E. Randall, M. A. Clilverd, E. Rozanov, and C. J. Rodger (2009), Geomagnetic activity and polar surface air temperature variability, *Journal of Geophysical Research: Space Physics*, *114*, A10312, doi:10.1029/2008JA014029.

Seppälä, A., H. Lu, M. A. Clilverd, and C. J. Rodger (2013), Geomagnetic activity signatures in wintertime stratosphere wind, temperature, and wave response, *Journal of Geophysical Research: Atmospheres*, *118*(5), 2,169–2,183, doi:10.1002/jgrd.50236.

Seppälä, A., M. A. Clilverd, M. J. Beharrell, C. J. Rodger, P. T. Verronen, M. E. Andersson, and D. A. Newnham (2015), Substorm-induced energetic electron precipitation: Impact on atmospheric chemistry, *Geophysical Research Letters*, *42*(19), 8,172–8,176, doi:10.1002/2015GL065523.

Sinnhuber, M., H. Nieder, and N. Wieters (2012), Energetic particle precipitation and the chemistry of the mesosphere/lower thermosphere, *Surveys in Geophysics*, *33*(6), 1,281–1,334, doi:10.1007/s10712-012-9201-3.

Sinnhuber, M., U. Berger, B. Funke, H. Nieder, T. Reddmann, G. Stiller, S. Versick, T. von Clarmann, and J. M. Wissing (2018), NO_y production, ozone loss and changes in net

radiative heating due to energetic particle precipitation in 2002–2010, *Atmospheric Chemistry and Physics*, *18*(2), 1,115–1,147, doi:10.5194/acp-18-1115-2018.

Smart, D. (1999), Changes in calculated vertical cutoff rigidities at the altitude of the International Space Station as a function of geomagnetic activity, *Proceedings of the 26th International Cosmic Ray Conference*, *7*, 337.

Smart, D., and M. Shea (2001), A comparison of the Tsyganenko model predicted and measured geomagnetic cutoff latitudes, *Advances in Space Research*, *28*(12), 1,733–1,738, doi:10.1016/S0273-1177(01)00539-7.

Smart, D., and M. Shea (2003), The space-developed dynamic vertical cutoff rigidity model and its applicability to aircraft radiation dose, *Advances in Space Research*, *32*(1), 103–108, doi:10.1016/S0273-1177(03)90376-0.

Smith-Johnsen, C., D. R. Marsh, Y. Orsolini, H. Nesse Tyssøy, K. Hendrickx, M. I. Sandanger, L.-K. G. Ødegaard, and F. Stordal (2018), Nitric oxide response to the April 2010 electron precipitation event: Using WACCM and WACCM-D with and without medium energy electrons, *Journal of Geophysical Research: Space Physics*, *123*(6), 5,232–5,245, doi:10.1029/2018JA025418.

Solomon, S., D. Rusch, J. Gérard, G. Reid, and P. Crutzen (1981), The effect of particle precipitation events on the neutral and ion chemistry of the middle atmosphere: II. Odd hydrogen, *Planetary and Space Science*, *29*(8), 885–893, doi:10.1016/0032-0633(81)90078-7.

Stauning, P. (1996), Investigations of ionospheric radio wave absorption processes using imaging riometer techniques, *Journal of Atmospheric and Terrestrial Physics*, *58*, 753–764, doi:10.1016/0021-9169(95)00072-0.

Stauning, P., and Y. Hisao (1995), Imaging Riometer Installation in Longyearbyen, Svalbard, *Technical report 95-12*, Danish Meteorological Institute, Copenhagen.

Størmer, C. (1955), *The polar aurora*, Clarendon Press, Oxford.

Tsyganenko, N. (1989), A magnetospheric magnetic field model with a warped tail current sheet, *Planetary and Space Science*, *37*(1), 5–20, doi:10.1016/0032-0633(89)90066-4.

Turunen, E., P. T. Verronen, A. Seppälä, C. J. Rodger, M. A. Clilverd, J. Tamminen, C.-F. Enell, and T. Ulich (2009), Impact of different energies of precipitating particles on NO_x generation in the middle and upper atmosphere during geomagnetic storms, *Journal of Atmospheric and Solar-Terrestrial Physics*, *71*(10), 1,176–1,189, doi:10.1016/j.jastp.2008.07.005.

Van Allen, J. A., W. C. Lin, and H. Leinbach (1964), On the relationship between absolute solar cosmic ray intensity and riometer absorption, *Journal of Geophysical Research*, *69*(21), 4,481–4,491, doi:10.1029/JZ069i021p04481.

van de Kamp, M., A. Seppälä, M. A. Clilverd, C. J. Rodger, P. T. Verronen, and I. C. Whittaker (2016), A model providing long-term data sets of energetic electron precipitation during geomagnetic storms, *Journal of Geophysical Research: Atmospheres*, *121*(20), 12,520–12,540, doi:10.1002/2015JD024212.

Verronen, P. T., and R. Lehmann (2013), Analysis and parameterisation of ionic reactions affecting middle atmospheric HO_x and NO_y during solar proton events, *Annales Geophysicae*, *31*(5), 909–956, doi:10.5194/angeo-31-909-2013.

Verronen, P. T., T. Ulich, E. Turunen, and C. J. Rodger (2006a), Sunset transition of negative charge in the D-region ionosphere during high-ionization conditions, *Annales Geophysicae*, *24*(1), 187–202, doi:10.5194/angeo-24-187-2006.

Verronen, P. T., A. Seppälä, E. Kyrölä, J. Tamminen, H. M. Pickett, and E. Turunen (2006b), Production of odd hydrogen in the mesosphere during the January 2005 solar proton event, *Geophysical Research Letters*, *33*(24), L24811, doi:10.1029/2006GL028115.

Verronen, P. T., B. Funke, M. López-Puertas, G. P. Stiller, T. von Clarmann, N. Glatthor, C.-F. Enell, E. Turunen, and J. Tamminen (2008), About the increase of HNO3 in the stratopause region during the Halloween 2003 solar proton event, *Geophysical Research Letters*, *35*(20), L20809, doi:10.1029/2008GL035312.

Verronen, P. T., M. E. Andersson, A. Kero, C.-F. Enell, J. M. Wissing, E. R. Talaat, K. Kauristie, M. Palmroth, T. E. Sarris, and E. Armandillo (2015), Contribution of proton and electron precipitation to the observed electron concentration in October–

November 2003 and September 2005, *Annales Geophysicae*, *33*(3), 381–394, doi: 10.5194/angeo-33-381-2015.

Verronen, P. T., M. E. Andersson, D. R. Marsh, T. Kovács, and J. M. C. Plane (2016), WACCM-D—Whole Atmosphere Community Climate Model with D-region ion chemistry, *Journal of Advances in Modeling Earth Systems*, *8*(2), 954–975, doi:10.1002/2015MS000592.

Vitt, F. M., and C. H. Jackman (1996), A comparison of sources of odd nitrogen production from 1974 through 1993 in the Earth's middle atmosphere as calculated using a two-dimensional model, *Journal of Geophysical Research: Atmospheres*, *101*(D3), 6,729–6,739, doi:10.1029/95JD03386.

Winckler, J. R., and P. D. Bhavsar (1960), Low-energy solar cosmic rays and the geomagnetic storm of May 12, 1959, *Journal of Geophysical Research*, *65*(9), 2,637–2,655, doi:10.1029/JZ065i009p02637.

Winckler, J. R., P. D. Bhavsar, and L. Peterson (1961), The time variations of solar cosmic rays during July 1959 at Minneapolis, *Journal of Geophysical Research*, *66*(4), 995–1022, doi:10.1029/JZ066i004p00995.

PAPER I

Bland, E. C., **Heino, E.**, Kosch, M. J., & Partamies, N. (2018). SuperDARN radar-derived HF radio attenuation during the September 2017 solar proton events. *Space Weather*, 16(10), 1,455–1,469. https://doi.org/10.1029/2018SW001916

AGU100 ADVANCING EARTH AND SPACE SCIENCE

Space Weather

RESEARCH ARTICLE
10.1029/2018SW001916

Special Section:
Space Weather Events of 4-10 September 2017

Key Points:
- SuperDARN HF radars were strongly affected by polar cap absorption events in September 2017
- A novel method to estimate HF attenuation using SuperDARN atmospheric noise measurements has been developed
- Up to 14-dB attenuation at 12 MHz was measured in the polar caps, resulting in backscatter loss

Correspondence to:
E. C. Bland,
emmab@unis.no

Citation:
Bland, E. C., Heino, E., Kosch, M. J., & Partamies, N. (2018). SuperDARN radar-derived HF radio attenuation during the September 2017 solar proton events. *Space Weather*, *16*, 1455–1469. https://doi.org/10.1029/2018SW001916

Received 24 APR 2018
Accepted 3 AUG 2018
Accepted article online 10 AUG 2018
Published online 2 OCT 2018

SuperDARN Radar-Derived HF Radio Attenuation During the September 2017 Solar Proton Events

Emma C. Bland[1,2], **Erkka Heino**[2,3], **Michael J. Kosch**[4,5,6], **and Noora Partamies**[1,2]

[1]Birkeland Centre for Space Science, Bergen, Norway, [2]Department of Arctic Geophysics, University Centre in Svalbard, Longyearbyen, Norway, [3]Department of Physics and Technology, University of Tromsø, Tromsø, Norway, [4]Physics Department, Lancaster University, Lancaster, UK, [5]South African National Space Agency, Hermanus, South Africa, [6]Department of Physics and Astronomy, University of Western Cape, Bellville, South Africa

Abstract Two solar proton events in September 2017 had a significant impact on the operation of the Super Dual Auroral Radar Network (SuperDARN), a global network of high-frequency (HF) radars designed for observing *F* region ionospheric plasma convection. Strong polar cap absorption caused near-total loss of radar backscatter, which prevented the primary SuperDARN data products from being determined for a period of several days. During this interval, the high-latitude and polar cap radars measured unusually low levels of background atmospheric radio noise. We demonstrate that these background noise measurements can be used to observe the spatial and temporal evolution of the polar cap absorption region, using an approach similar to riometry. We find that the temporal evolution of the SuperDARN radar-derived HF attenuation closely follows that of the cosmic noise absorption measured by a riometer. Attenuation of the atmospheric noise up to 10 dB at 12 MHz is measured within the northern polar cap, and up to 14 dB in the southern polar cap, which is consistent with the observed backscatter loss. Additionally, periods of enhanced attenuation lasting 2–4 hr are detected by the midlatitude radars in response to M- and X-class solar flares. Our results demonstrate that SuperDARN's routine measurements of atmospheric radio noise can be used to monitor 8- to 20-MHz radio attenuation from middle to polar latitudes, which may be used to supplement riometer data and also to investigate the causes of SuperDARN backscatter loss during space weather events.

Plain Language Summary Solar proton events are known to cause widespread disruption to high-frequency (HF) radio communications in the high-latitude and polar regions. We demonstrate that SuperDARN HF radars may be used to monitor HF radio wave attenuation during solar proton events using routine measurements of the background radio noise. These background noise measurements are produced as part of the radar data processing, but they are not normally used for science applications. We focus on two solar proton events, which occurred in September 2017, and find that the measured radio attenuation is confined to the polar cap and exhibits temporal and spatial properties that are characteristic of polar cap absorption events. The attenuation measured by the Rankin Inlet SuperDARN radar agrees well with measurements from a nearby riometer, indicating that reasonable estimates of the HF radio attenuation can be obtained from SuperDARN radars despite the high day-to-day variability of the atmospheric radio noise. Our technique may also prove useful for determining the reasons for backscatter loss, particularly when riometer data are not available.

1. Introduction

Ionospheric disturbances caused by solar flares and solar energetic particles are known to disrupt high-frequency (HF, 3–30 MHz) transionospheric radio systems, including HF communication systems used in aviation, maritime, and emergency management, as well as over-the-horizon radars used in applications such as ionospheric research, coastal hazard management, and defense (e.g., Ferguson et al., 2015; Goodman, 2005; Knipp et al., 2016). These ionospheric disturbances cause electron density enhancements which affect HF radio propagation in two distinct ways: (1) increased radio wave attenuation in the *D* region ionosphere (50–90 km) due to collisions between electrons and neutral particles, and (2) changes to the available ionospheric propagation paths in the *E* region (90–150 km) and *F* region (150–600 km). Electron density enhancements in the *D* region arise due to energetic proton precipitation and photoionization from soft X-ray

radiation, whereas enhancements in the *E* and *F* regions arise primarily from extreme ultraviolet and soft X-ray radiation. At auroral latitudes, energetic electron precipitation is also a significant source of ionization above ~100-km altitude. This study focuses on the effects of *D* region electron density enhancements caused by solar proton events (SPEs) and their associated solar flares.

A solar proton event is characterized by the increased flux of high-energy (>10 MeV) protons from the Sun. Solar protons impact the Earth's atmosphere in the polar regions causing increased ionization of the *D* region ionosphere. The size of the affected region depends on the particle rigidity (momentum per unit charge) and the shape of the geomagnetic field, and typically extends from about 60° to 90° geomagnetic latitude (Kress et al., 2010). Consequently, the associated radio absorption is termed *polar cap absorption* (PCA) (Bailey, 1964). PCA is most pronounced in the sunlit ionosphere where the effective recombination coefficient below 80-km altitude is lower (e.g., Hargreaves et al., 1993; Ranta et al., 1995). Since PCA events may last for several days, they have significant consequences for high-latitude users of HF communications, such as commercial airlines operating on transpolar routes (Jones et al., 2005).

The particle acceleration for SPEs is driven by solar flare and/or coronal mass ejection processes (Kallenrode, 2003; Reames, 1999). A solar flare is a brief, explosive release of broadband electromagnetic radiation from the solar surface lasting from minutes to hours. Extreme ultraviolet and X-ray radiation released during the flare may cause excess ionization of the lower dayside ionosphere, resulting in brief periods of strong HF radio absorption known as shortwave fadeout (SWF). SWF affects only those communications circuits that have an ionospheric reflection point in the sunlit ionosphere, since the nightside of the Earth is shielded from the X-ray radiation.

PCA and SWF have been studied for several decades using riometers (e.g., Brodrick et al., 2005; Fiori & Danskin, 2016; Kavanagh et al., 2004; Reid & Leinbach, 1959, 1961), as well as incoherent scatter radars (e.g., Hargreaves et al., 1987; Mendillo & Evans, 1974), very low frequency (VLF) receivers (e.g., Kossey et al., 1983; Wenzel et al., 2016), and Global Positioning System satellite measurements of total electron content (Garcia-Rigo et al., 2007). Recently, there have been efforts to utilize existing HF radio infrastructure to monitor the ionospheric effects of space weather events, in particular, SWF. For example, Frissell et al. (2014) demonstrated that data sent to amateur radio reporting networks can be used to identify communications circuits affected by SWF. Also, several studies have demonstrated that the Super Dual Auroral Radar Network (SuperDARN) may be used to detect SWF at midlatitudes. In this case, the HF radio waves transmitted by the radars are absorbed by the *D* region, resulting in the loss of radar backscatter (Chakraborty et al., 2018; Watanabe & Nishitani, 2013). Also, the background radio noise levels measured by each radar decrease sharply at the event onset and gradually recover to nominal levels in the hours following the flare (Berngardt et al., 2018). In this study we build upon this work to demonstrate that SuperDARN radars may also be used to monitor the spatial and temporal evolution of PCA. In particular, we utilize the background noise measurements from SuperDARN radars to quantify the degree of attenuation using an approach similar to riometry. We demonstrate this capability through case studies of two solar proton events which occurred in September 2017.

2. Instrumentation

2.1. The SuperDARN

The primary instruments used in this study are the SuperDARN HF radars. SuperDARN is a global network of high-frequency (HF) radars designed for studying large-scale ionospheric plasma convection from middle to polar latitudes (Chisham et al., 2007; Greenwald et al., 1995; Lester, 2013). As of 2018 the network consists of 23 radars in the Northern Hemisphere and 12 radars in the Southern Hemisphere. The radars detect coherent backscatter from field-aligned electron density irregularities, which are used as tracers for measuring the *F* region plasma convection. The radars may also detect backscatter from the ground/sea and from meteor plasma trails at around 90-km altitude. When a scattering target is detected, the power (signal-to-noise ratio), Doppler velocity, and spectral width of the received backscatter are determined. These parameters are used for studying the ionospheric signatures of a wide range of phenomena, including the structure and dynamics of global convection (e.g., Ruohoniemi & Baker, 1998), polar cap expansion during substorms (e.g., Bristow & Jensen, 2007), ultralow frequency magnetohydrodynamic waves (e.g., Ponomarenko et al., 2003), and gravity waves (e.g., Bristow et al., 1996). A range of methods have also been developed for determining ionospheric critical frequencies and electron densities using SuperDARN radars (Bland et al., 2014; Gillies et al., 2009, 2011;

Figure 1. (top panel) Locations and fields of view of the Clyde River (CLY), Rankin Inlet (RKN), Saskatoon (SAS), and Christmas Valley East (CVE) SuperDARN radars. The location of the riometer at Taloyoak (TALO) is shown in red. (bottom panel) Locations and fields of view of the South Pole Station (SPS), McMurdo Sound (MCM), Dome C East (DCE), and Zhongshan (ZHO) SuperDARN radars. The blue shading shows the position of the beam used in Figures 2 and 7. Dotted and dashed lines show geographic and geomagnetic coordinates, respectively.

Hughes et al., 2002; Ponomarenko et al., 2011; Sarno-Smith et al., 2016), in some cases taking advantage of the real-time availability of data from some radars.

Each SuperDARN radar consists of a linear array of log-periodic or twin-terminated folded dipole antennas, which are phased electronically to produce a narrow (~3.24°), steerable beam. For most radars, this beam can be steered in 16 different azimuthal directions (numbered 0–15), while some newer radars in the network operate with up to 24 azimuthal beams and thus have wider fields of view. The fields of view of four SuperDARN radars in North America and another four in Antarctica are shown in Figure 1, with one beam shaded for each radar. The antennas exhibit significant gain from approximately 10° to 45° in vertical elevation (e.g., Milan et al., 1997), so the beam is narrow in azimuth but wide in vertical elevation.

SuperDARN radars are designed to operate in the frequency range of 8–20 MHz; however, in practice, most radars operate in the 10–15-MHz range. The radars employ a multipulse sequence method (Greenwald et al., 1985; Ribeiro et al., 2013), which allows all of the radar's range gates to be sampled together in each scan. In the standard mode of operation, called *common mode*, the beams are sampled sequentially with a ~3 s or ~7 s

dwell time. It therefore takes either 1 or 2 minutes to scan all beams in the field of view, which sets the time resolution of the data products. The standard range gate resolution is 45 km.

The primary data products of SuperDARN (power, Doppler velocity, and spectral width) are determined using a fitting routine in the SuperDARN data analysis software called FITACF. FITACF also estimates the background noise level (called the *sky noise* in the data files), which is used to determine which range gates contain coherent backscatter. This background noise measurement is the focus of this study. The noise level is estimated as the average of the 10 lowest values of the lag zero power recorded in all of the radar's range gates (there are between 70 and 110 range gates depending on the radar's configuration). In a recent upgrade to the software, a correction for the effective number of noise samples is also applied, without which the noise level would be underestimated. This method is appropriate for SuperDARN radars because the available ionospheric propagation modes (half-hop, one-hop, etc.) confines the observed backscatter to particular bands of range gates. In this study we have processed the raw radar data using this updated version of FITACF (FITACF 3.0, https://doi.org/10.5281/zenodo.1143675), which uses the condition SNR $\geq$ 1 to identify coherent backscatter. We emphasize that the background noise parameter is available for every scan, including intervals when no coherent backscatter was detected in any range gate. Thus, the noise measurement is available during strong PCA events when the power, velocity, and spectral width parameters cannot be measured.

2.2. Supporting Instrumentation

In this study we also use data from the GO Canada 30 MHz single-beam riometer located at Taloyoak (69.54°N, 93.56°W; Rostoker et al., 1995). A riometer (relative ionospheric opacity meter) is a passive instrument consisting of a radio receiver operating in the 20- to 60-MHz frequency range (Little & Leinbach, 1959). The background radio spectrum at these frequencies is dominated by cosmic radio noise. A reduction in the cosmic radio noise measured at ground level may be attributed to attenuation by the ionosphere and is called *cosmic noise absorption* (CNA). CNA is measured relative to a *quiet day curve* (QDC), which is the background noise level during undisturbed ionospheric conditions and is a function of sidereal time. The QDCs are derived using historical data from the riometer; the method used to baseline the GO Canada riometer data is described in http://aurora.phys.ucalgary.ca/norstar/rio/doc/CANOPUS_Riometer_Baselining.pdf.

We also use integral particle flux measurements from one of the Geosynchronous Operational Environmental Satellites (GOES) (NASA, 2006), which is operated by the National Oceanic and Atmospheric Administration (NOAA). We use the particle flux data from the GOES-15 spacecraft, which is positioned in geosynchronous orbit at 135.0°W. The integral particle flux data are measured by the GOES-15 energetic particle sensor and are provided for energy ranges $\geq$10 MeV, $\geq$50 MeV, and $\geq$100 MeV at 5 min time resolution.

3. SuperDARN Response to the Solar Proton Events

The two solar proton events considered in this study occurred in September 2017. These two events were identified using a standard definition based on proton flux measurements from NOAA-GOES spacecraft—the start of the event is the first of three consecutive measurements of >10-MeV protons with fluxes greater than 10 $cm^{-2}{\cdot}sr^{-1}{\cdot}s^{-1}$, and the event ends when the flux exceeds this value for the last time (https://umbra.nascom.nasa.gov/SEP/). The first panel of Figure 2 shows the integral proton flux measured by the GOES-15 satellite from 1 to 16 September 2017. The two SPEs are labeled as *Event 1* and *Event 2*. Based on the above event threshold level (indicated by the horizontal dashed line in the figure), Event 1 commenced at 01:25 UT on 5 September and ended at 22:45 UT on 8 September. Event 2 commenced at 16:45 UT on 9 September and ended at 17:10 UT on 14 September.

We will first consider the response of four North American SuperDARN radars to the SPEs. The top panel of Figure 1 shows the locations and fields of view of the Clyde River (CLY), Rankin Inlet (RKN), Saskatoon (SAS), and Christmas Valley East (CVE) radars. The blue shading shows the position of beam 5 for the CLY radar and beam 7 for the other three radars. These beams were chosen because they are near the center of each radar's field of view and had continuous temporal coverage for the time period shown. The response of these four radars to the SPEs is shown in the second–fifth panels of Figure 2. The red line in each panel shows the instantaneous echo occurrence, which is the percentage of range gates containing coherent backscatter for a single scan. Prior to the onset of Event 1, the instantaneous echo occurrence at each site ranges from approximately 5% to 40%. During Event 1, the echo occurrence for the two polar cap radars (CLY and RKN) approaches zero when the radars are positioned on the dayside of the Earth. This occurs at CLY from ~09:30 to 23:30 UT, and at RKN

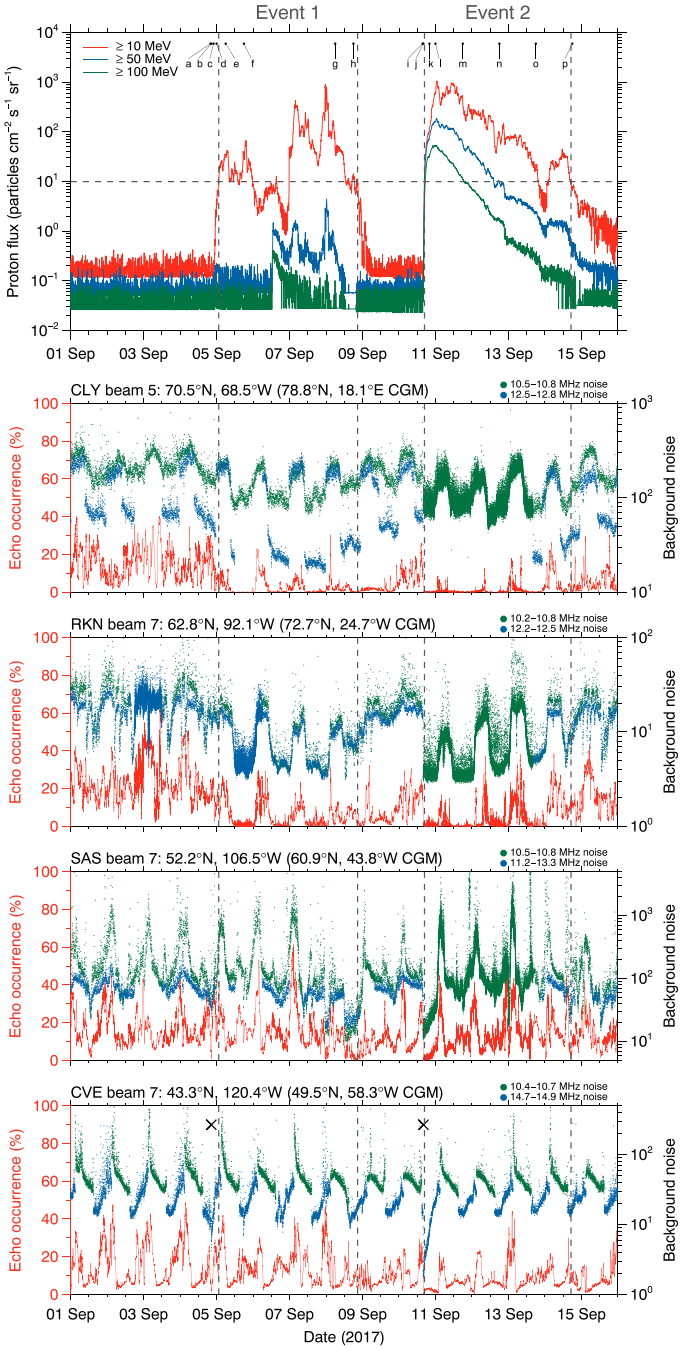

Figure 2. (first panel) Proton fluxes measured by the NOAA GOES-15 satellite from 1 to 16 September 2017. Echo occurrence (red) and background noise measurements (blue and green) from the (second panel) Clyde River (CLY), (third panel) Rankin Inlet (RKN), (fourth panel) Saskatoon (SAS), and (fifth panel) Christmas Valley East (CVE) SuperDARN radars. Solar noon at these stations occurs at approximately 16:31 UT (CLY), 18:05 UT (RKN), 19:03 UT (SAS), and 19:59 UT (CVE). The vertical dashed lines indicate the start and end times of the two solar proton events labeled *Event 1* and *Event 2*, and the black crosses in the fifth panel show the onset time of two solar X-ray flares. The letters (a)–(p) in the first panel correspond to times shown in Figure 6. NOAA = National Oceanic and Atmospheric Administration; GOES = Geostationary Operational Environmental Satellite; SuperDARN = Super Dual Auroral Radar Network.

from ~11:30 to 00:30 UT. The echo occurrence recovers briefly from 10 to 11 September, up until the onset of Event 2 when the dayside echo occurrence nears zero again. During Event 2, very little backscatter was detected by the CLY radar at any local time. At Rankin Inlet, located several degrees equatorward of Clyde River, backscatter was detected only during the night (~00:30–11:30 UT). The low echo occurrence indicates that the radio waves transmitted by the CLY and RKN radars were strongly attenuated by the ionosphere during the periods of enhanced proton flux. This effect is most pronounced during the daytime, which is expected for PCA events (see section 1).

At Saskatoon, the echo occurrence approaches zero toward the end of Event 1 and also near the beginning of Event 2. This approximately coincides with the increased flux of higher-energy protons (≥50 MeV). Similarly, the echo occurrence at Christmas Valley East decreased slightly toward the end of Event 1 and more significantly during Event 2. Due to the low latitude of the CVE radar, the data set is dominated by ground backscatter, which produces the regular daytime occurrence peaks in Figure 2 from 1 to 5 September (~13:30–02:20 UT). Thus, the reduction or absence of these peaks is evidence of enhanced attenuation by the *D* region on the dayside.

The blue and green symbols in Figure 2 show the background noise measured by each radar. The color coding indicates the frequency at which the noise was measured. For most of the time interval shown, CLY, RKN, and SAS were alternating between two frequency bands, and CVE alternated between a daytime and nighttime frequency every 12 hr. The use of different frequency bands produces the discontinuities in the noise measurements, with higher frequencies associated with lower noise levels. During both SPEs, there is a decline in the overall noise level at CLY and RKN, indicating that the background radio noise was attenuated during the SPEs. This is particularly apparent for the 12.5- to 12.8-MHz data at CLY during Event 1 for which the daytime (~09:30–23:30 UT) noise level is reduced by a factor of ~3.

The background noise behaves differently at Saskatoon and Christmas Valley East compared to the polar cap. For these radars, there is a sharp decrease in the noise level and the instantaneous echo occurrence just prior to each SPE. This behavior coincides with the release of two solar flares, which are marked by the crosses in the fifth panel of Figure 2. For the flare on 4 September, the sudden decrease in the noise level observed at SAS and CVE and the gradual recovery to preflare levels over a 1- to 2-hr period agrees well with SuperDARN observations of SWF by Berngardt et al. (2018). There is also a sudden decrease in the noise levels at SAS and CVE following the flare on 10 September. In this case the recovery time at both radar sites is about 10 hr. This longer recovery time may be due to strong *D* region ionization at midlatitudes caused by the increased flux of ≥100-MeV protons near the beginning of Event 2. This makes it difficult to distinguish between the ionospheric disturbance caused by the solar flare and the disturbance due to the solar protons.

The results presented in Figure 2 indicate that both the SuperDARN echo occurrence and the background sky noise parameters respond to the enhanced particle flux associated with solar proton events. These data can be used to observe the spatial and temporal evolution of PCA caused by solar energetic particles. In section 5 we will use the SuperDARN background noise measurements to quantify the degree of attenuation during the September 2017 solar proton events using methods derived from riometry. To perform this estimate, it is first necessary to characterize the behavior of the noise in the absence of any ionospheric disturbances.

4. SuperDARN Background Noise

A key difference between riometers and SuperDARN radars is that the radio spectrum at their respective operating frequencies arise from different sources. At riometer operating frequencies (20–60 MHz), the background radio spectrum is dominated by cosmic radio noise. For an undisturbed ionosphere, the cosmic noise at a given frequency varies with sidereal time only. In contrast, at the typical SuperDARN operating frequencies (10–15 MHz), the radio spectrum is dominated by atmospheric noise, which arises primarily from lightning strikes (Headrick & Anderson, 2008). Although lightning strikes occur most frequently in the tropics, their radio emissions can propagate to polar latitudes via the ionosphere. Therefore, the atmospheric noise measured by SuperDARN radars from middle to polar latitudes is controlled by both the global distribution of thunderstorm activity and the ionospheric propagation conditions (e.g., Giordano & Haber, 1972). In contrast to cosmic noise, atmospheric noise is mostly a function of *solar time* and exhibits day-to-day and seasonal variability.

Background noise measurements from the Zhongshan SuperDARN radar for the year 2012 are shown in the top panel of Figure 3. This radar is located in the southern polar cap at 69.38°S, 76.38°E (74.9°S, 97.2°E geomagnetic), as shown in the lower panel of Figure 1. We have chosen the Zhongshan radar to illustrate the

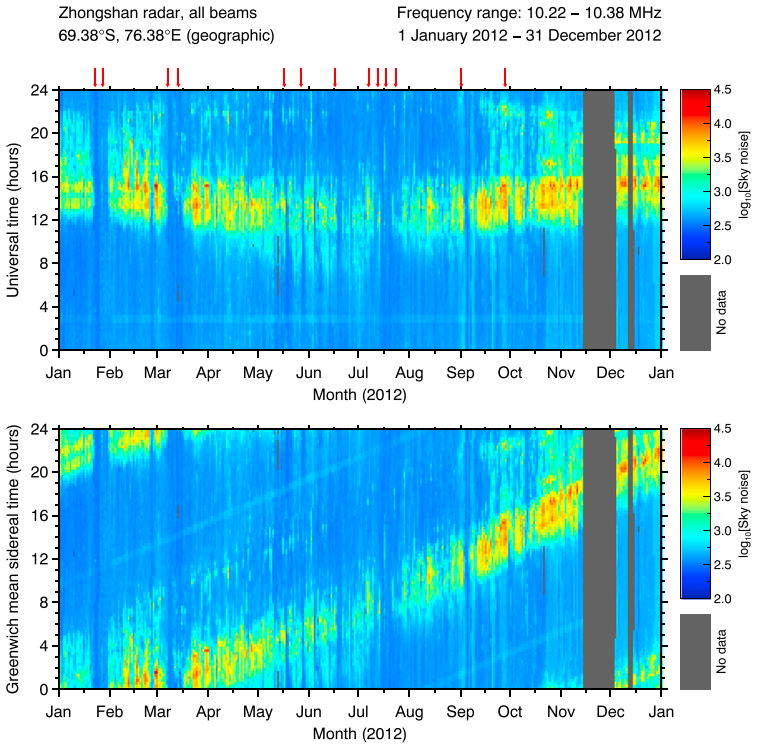

Figure 3. Background noise for the year 2012 measured by the Zhongshan SuperDARN radar. In the top (bottom) panel, the diurnal variation is plotted as a function of universal time (sidereal time). The red arrows indicate the onset times of solar proton events. SuperDARN = Super Dual Auroral Radar Network.

behavior of SuperDARN noise measurements because this radar operated in a fixed, narrow frequency band (10.22–10.38 MHz) for the entire year. This makes it straightforward to visualize the diurnal and seasonal variation of the noise, as well as the effects of multiple SPEs which occurred in 2012. The noise data have been binned according to universal time and day of year. The noise exhibits a clear diurnal trend, with a daily maximum at around 13:00–15:00 UT, which corresponds to 18:00–20:00 local time at the radar site. Lower noise levels were measured in the Antarctic winter months (June, July, August), which is expected due to the reduced lightning activity and lower ionospheric electron densities in the winter hemisphere. The red arrows on the top horizontal axis indicate the onset times for the 13 SPEs which occurred in 2012. There is a decrease in the noise level for each SPE lasting for several days, which we attribute to polar cap absorption.

The bottom panel of Figure 3 shows the same data set binned according to Greenwich mean sidereal time instead of universal time. Any significant sidereal-time-dependent component in the SuperDARN sky noise would manifest itself in this plot as an approximately horizontal feature. However, no such feature is apparent. Therefore, we conclude that the SuperDARN sky noise parameter is controlled by terrestrial sources, namely. atmospheric noise. This result will be used in the next section to generate 'quiet day curves' for SuperDARN radars.

5. SuperDARN Radar-Derived HF Attenuation

To estimate the radio attenuation at each radar site, we have adopted a procedure similar to the methods used for determining CNA from riometer data. The first step is to construct QDCs for the SuperDARN data, analogous to riometer QDCs. For this purpose we have used the SuperDARN data set spanning the interval 1–31 August 2017. Since the background noise is frequency dependent (see Figure 2), we separated the data from each radar into frequency bands. Throughout August and September 2017, most radars operated in two distinct frequency bands, either alternating between the two bands every minute or operating in one frequency band during the day and a different band at night. Brief periods in which the radars were operated

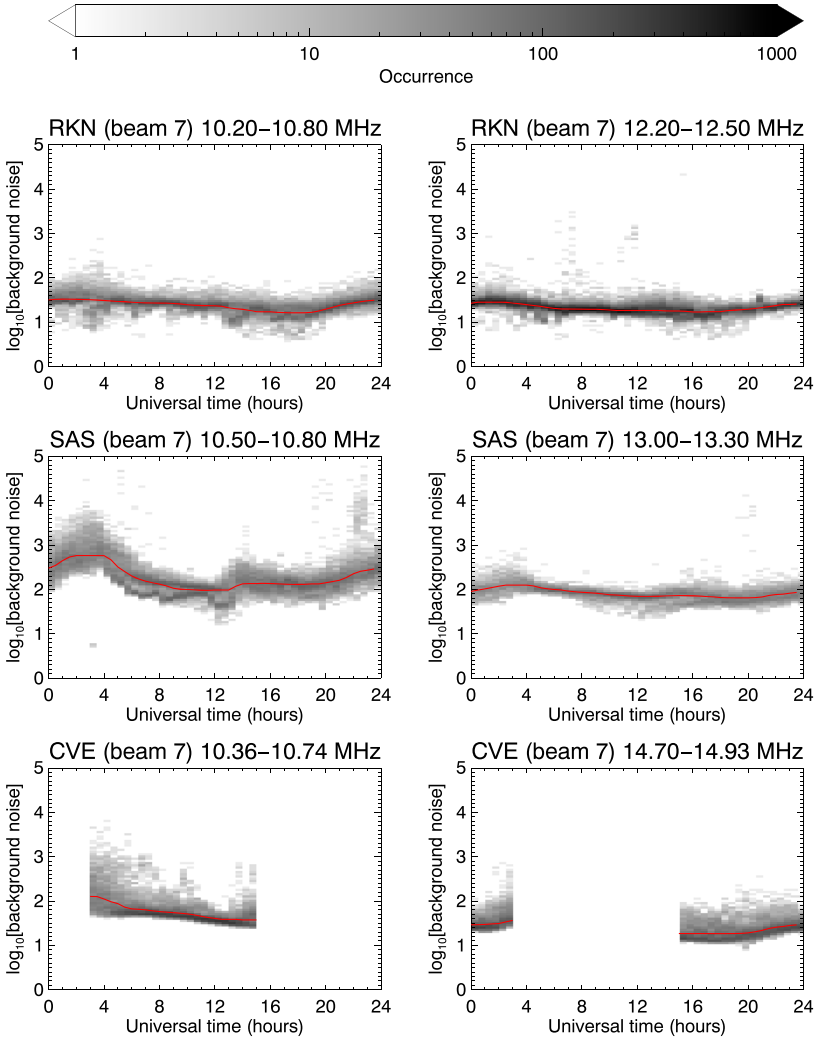

Figure 4. Two-dimensional histograms of the background *sky* noise measured by the Rankin Inlet (RKN), Saskatoon (SAS), and Christmas Valley East (CVE) radars (beam 7 only). The red lines show the final quiet day curves after smoothing.

at other frequencies were excluded. Time intervals for which the radars were operated with a range resolution other than 45 km were also excluded, since we have observed that the noise level changes when the range gate resolution is changed (not shown). The remaining data set covered a minimum of 25 days in August for each radar.

We have observed that the background noise level varies with the azimuthal beam direction, particularly near the solar terminator for the eastward and westward oriented beams. Therefore, separate QDCs were generated for each radar beam and also for each frequency band. The noise measurements for August 2017 were binned into 30-min intervals of universal time (UT), and the median value of the noise in each UT bin was determined. The resulting curve was then smoothed by median filtering to obtain the final QDC. This procedure is illustrated in Figure 4 for beams 7 of the RKN, SAS, and CVE radars. The color scale shows the noise distribution in universal time from 1 to 31 August 2017, and the red lines show the smoothed median noise levels which are used as the QDCs. The gaps in the CVE data arise because the radar operated in separate daytime and nighttime frequency bands. Using median atmospheric noise measurements to produce the QDCs should automatically exclude the effects of any short-term ionospheric disturbances such as SWF in the

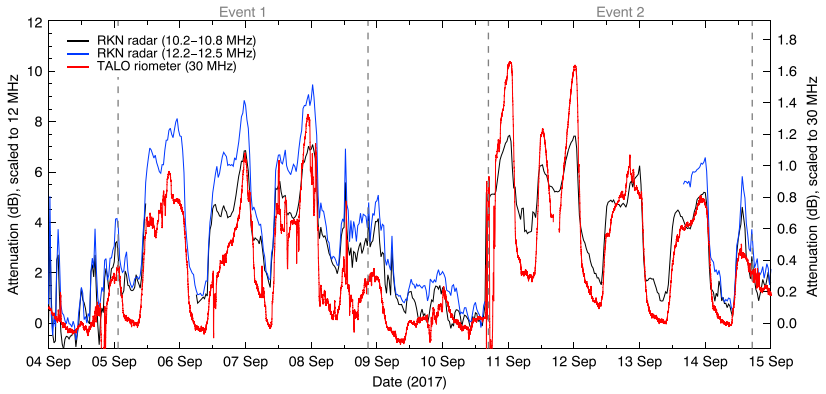

Figure 5. Radio attenuation measured by the Rankin Inlet SuperDARN radar (RKN) and the 30-MHz cosmic noise absorption measured by the Taloyoak riometer (TALO). The radar- and riometer-derived attenuation values can be read using both vertical axes, which show the equivalent attenuation at 12 MHz and 30 MHz. The vertical dashed lines indicate the start and end times of the two solar proton events labeled *Event 1* and *Event 2*.

QDC data set. Long-duration disturbances caused by SPEs or intense geomagnetic storms would affect the accuracy of the QDCs and should be excluded; however, no such events occurred during August 2017.

Following standard methods used in riometry (e.g., Brodrick et al., 2005; Rosenberg et al., 1991), the attenuation relative to the QDC was then determined for each beam and frequency band as

$$A = 10 \log_{10} \left[\frac{N_{\mathrm{QDC}}}{N} \right] \tag{1}$$

where N is the measured background noise and N_{QDC} is the value of the quiet day curve at the corresponding universal time.

In order to compare attenuation measurements from different frequency bands, and also with CNA measurements from riometers, it is necessary to scale all attenuation measurements to their equivalent values at a common frequency. For HF radio waves, *D* region nondeviative absorption varies as the inverse square of the frequency (e.g., Davies, 1990):

$$A_f = A_0 \left(\frac{f_0}{f} \right)^2 \tag{2}$$

where A_0 is the radio wave attenuation measured at frequency f_0, and A_f is the equivalent attenuation at another frequency f. In this study we have chosen to scale all SuperDARN-derived attenuation values to 12 MHz and also to 30 MHz for comparison with riometer data.

Figure 5 shows the HF attenuation measured on beam 7 of the Rankin Inlet radar from 4 to 15 September 2017. The black (blue) line shows the attenuation measured in the 10.20–10.80 MHz (12.20–12.50 MHz) frequency band. The red line shows the cosmic noise absorption measured by the Taloyoak riometer (TALO). The radar- and riometer-derived attenuation values can be read using both vertical axes; the left axis indicates the equivalent attenuation at 12 MHz, and the right axis indicates the equivalent attenuation at 30 MHz (determined using equation (2).

The temporal evolution of the SuperDARN radar-derived attenuation closely follows the CNA measured by the riometer. The differences between the two data sets may be due to the different methods used to determine the QDCs, and the high day-to-day variability of the atmospheric radio noise which limits the precision of the SuperDARN QDCs (see section 6). Despite these differences, the radar-derived attenuation reproduces the key features of the riometer-derived CNA, specifically the diurnal variation and the shape of the amplitude envelope for both events. This indicates that the QDCs generated from the SuperDARN atmospheric noise measurements provided a reasonable reference noise level from which to estimate the attenuation.

Maps of the SuperDARN radar-derived attenuation for all Northern Hemisphere SuperDARN radars are shown in Figure 6. Each azimuthal beam has been projected out to 900 km from each radar site at 90-km altitude.

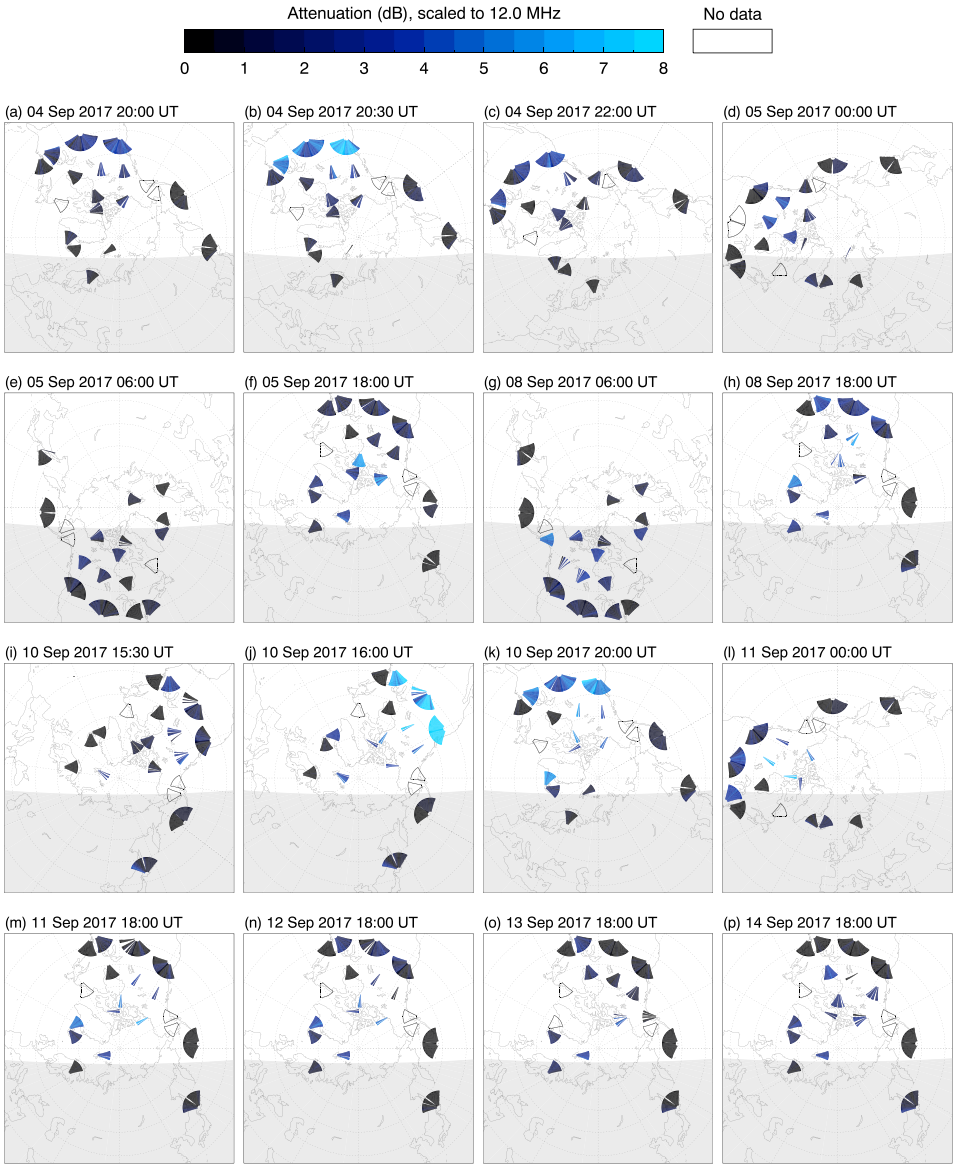

Figure 6. Maps of radio attenuation scaled to 12 MHz for selected time intervals during the two solar proton events. Panels (a)–(d) show the response to the first solar flare on 4 September (20:33 UT). Panels (e)–(h) show the polar cap absorption during Event 1. Panels (i)–(l) show the response to the second solar flare on 10 September (16:06 UT). Panels (m)–(p) show the polar cap absorption during Event 2.

This projection distance is arbitrary because the noise represents the overall background noise level along the beam and cannot be assigned to a specific point in the ionosphere (see section 6). All attenuation values have been scaled to the equivalent attenuation at 12 MHz using equation (2). When the attenuation was measured at two frequencies on a given radar beam, the results were averaged together after scaling. The gray shading in each panel indicates the nightside of the ionosphere. For several of the intervals shown, data from some radars were available only for selected beams, reflecting the use of operational modes other than the common mode. The times shown in panels (a)–(p) correspond to the letters (a)–(p) in the top panel of Figure 2.

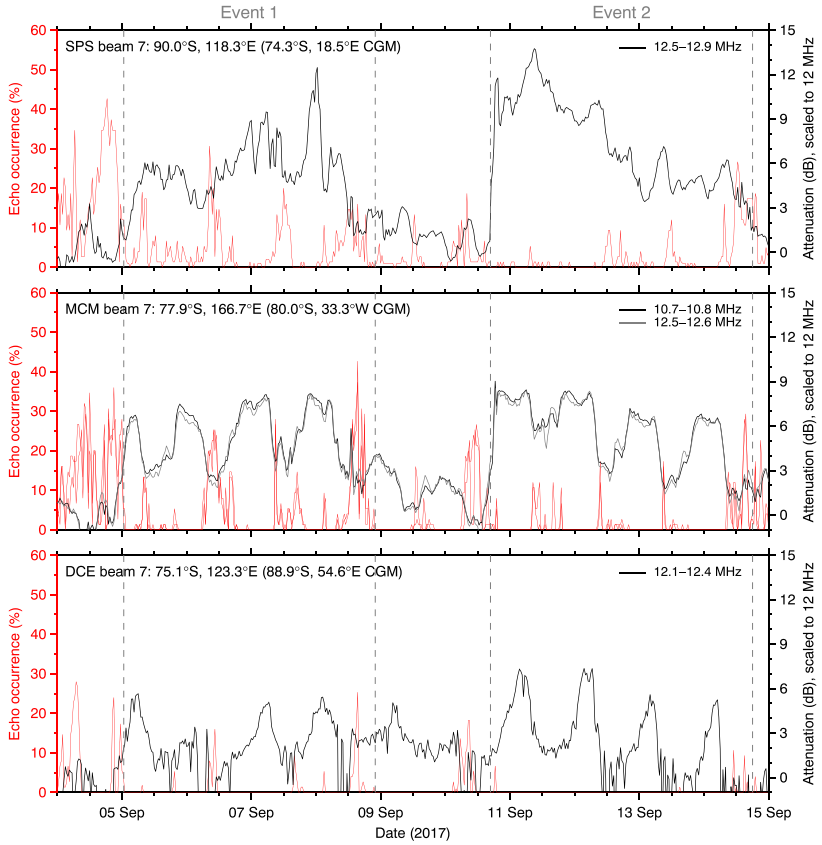

Figure 7. Echo occurrence and radio attenuation measured by the (top) South Pole Station (SPS), (middle) McMurdo Sound (MCM), and (bottom) Dome C East (DCE) SuperDARN radars. The attenuation values have been scaled to 12 MHz using equation (2). Solar noon at MCM and DCE occur at approximately 00:50 UT and 03:43 UT, respectively. CGM=corrected geomagnetic.

Panels (a)–(d) show the midlatitude radar response to the M5 solar flare which occurred at 20:33 UT on 4 September. Prior to the solar flare (panel a), very low levels of attenuation were observed by all radars. A peak in the attenuation occurs at midlatitudes when the flare occurs (panel b), which gradually decays in the hours following the flare (panels c–d).

The evolution of the PCA during Event 1 is shown in panels (e)–(h). Significant attenuation is observed only by the high-latitude and polar cap radars, and thus, the *D* region enhancement associated with the SPE is confined to the polar caps as expected. The radar response to an X8 solar flare at 16:06 UT on 10 September is shown in panels (i)–(l). The response is similar to the M5 flare, with a sudden peak in the midlatitude attenuation which then declines over the following hours. Finally, panels (m)–(p) show the attenuation at 18:00 UT for each day of Event 2. The enhanced attenuation is confined to polar latitudes and decreases gradually as the proton flux decreases.

The HF attenuation during the two SPEs was also determined for three SuperDARN radars located within the southern polar cap—South Pole Station (SPS), McMurdo Sound (MCM), and Dome C East (DCE). The locations and fields of view of these radars are shown in the bottom panel of Figure 1, with beam 7 shaded for each radar. Figure 7 shows the echo occurrence and the attenuation measured on beam 7 for each of these radars, scaled to 12 MHz. All three radars exhibit backscatter loss during the two events. At SPS and MCM, the backscatter loss occurs only at certain local times, whereas at DCE the backscatter loss lasts for almost the entire event.

In addition to the backscatter loss, the SPS, MCM, and DCE radars measure enhanced levels of attenuation during the SPEs, with stronger attenuation occurring at higher geographic latitudes. The attenuation

measured by these radars exhibits similar behavior to the attenuation measured at Rankin Inlet (Figure 5), with the attenuation peaks centered approximately around local midday in each case. At McMurdo Sound, the daytime attenuation maxima coincide with the echo occurrence minima. Similarly, at South Pole Station, backscatter is detected during the SPEs only when the attenuation is low ($\lesssim$4 dB at 12 MHz). These results provide strong evidence that the observed backscatter loss at each radar site is caused by attenuation of the transmitted radio waves, rather than an absence of scattering targets, for example.

6. Discussion

In this paper we have demonstrated that SuperDARN radars can be used to observe the spatial and temporal evolution of polar cap absorption using routine measurements of the background radio noise. This background noise measurement is required for processing the raw radar data and is recorded in the SuperDARN data files, but it is not normally used in science applications. The authors are aware of two previous studies utilizing the background noise data: (1) Berngardt et al. (2018), who showed that background noise measurements by the midlatitude SuperDARN radars can be used to detect shortwave fadeout, and (2) Ponomarenko et al. (2016), who investigated the effect of background noise on long-term echo occurrence rates. These two studies, and our study, highlight the utility of SuperDARN background noise data for monitoring ionospheric disturbances.

Although this study has focused on attenuation due to solar proton events and solar flares, it may also be possible to use SuperDARN radars to detect attenuation caused by other ionospheric disturbances, particularly energetic electron precipitation (EEP) during geomagnetic storms, substorms, and pulsating aurora. The SuperDARN data set consists of more than 20 years of continuous observations, including background noise measurements and may provide a useful addition to riometer, incoherent scatter radar, and optical observations of EEP. Ionospheric disturbances due to EEP are generally weaker than those caused by SPEs and solar flares and would be more difficult to detect within the highly variable atmospheric noise.

The SuperDARN noise measurements may be useful for identifying the causes of SuperDARN backscatter loss. Backscatter loss has been shown to occur for several reasons, including signal attenuation (Milan et al., 1999, 2008), disturbed propagation conditions in the *E* or *F* region (Baker et al., 2007; Currie et al., 2016; Danskin et al., 2002; Gauld et al., 2002), and the suppression of ionospheric irregularities in the observation region (Baker et al., 2007; Milan et al., 1999). Colocated riometer and SuperDARN data are rarely available, so the SuperDARN data may be a substitute for riometer data when determining whether attenuation was the cause of backscatter loss. The *combination* of reduced noise levels and backscatter loss indicates that attenuation has occurred. If backscatter loss results from the absence of scattering targets or disturbed propagation conditions, one would expect no such reduction in the background noise. Backscatter loss may also result from external radio interference, which would be accompanied by an increase in the background noise.

There are several factors that must be considered when interpreting SuperDARN background noise measurements and the HF attenuation values derived from them. First, there is an inherent ambiguity in assigning geographic coordinates to the attenuation values due to the shape of the antenna gain pattern. The gain pattern has a wide vertical extent and oblique orientation, ranging from about 10° to 45° from the horizontal. Furthermore, the antenna gain pattern includes a large backlobe and sidelobes (Milan et al., 1997; Sterne et al., 2011), which are also sensitive to atmospheric noise. Since atmospheric noise is produced equatorward of most SuperDARN radar sites, we anticipate that the backlobe may at times be the dominant contributor to the noise measurement. For example, radars located near the boundary of the PCA region would detect significantly more noise from the equatorward oriented backlobe compared to the poleward oriented main lobe. This makes it difficult to assign geographic coordinates to SuperDARN attenuation measurements.

Further ambiguity arises from the fact that atmospheric noise propagating via the ionosphere to the polar caps traverses the *D* region in at least two separate locations (i.e., for one-hop propagation modes). The radar cannot distinguish between attenuation that occurred close to the radar site and that which occurred ~1,000–2,000 km away where the noise signal propagated from the troposphere to the ionosphere. For PCA events, it is expected that the attenuation is confined to the region poleward of ~60° magnetic latitude, so attenuation measured by the polar cap SuperDARN radars is likely to be caused by an ionospheric enhancement close to the radar site. We can justify this further by considering the absence of radar backscatter during the periods of PCA. Echo returns from polar cap SuperDARN radars are dominated by half-hop ionospheric

backscatter, for which the only *D* region traversal occurs within a few hundred kilometers of the radar site. Therefore, the loss of backscatter from the polar cap radars is evidence that the attenuation occurred close to the radar site.

One should also verify that the SuperDARN-derived attenuation is consistent with the observed backscatter loss. For the two PCA events considered in this work, attenuation up to 10 dB at 12 MHz was detected within the northern polar cap, and up to 14 dB in the southern polar cap. In order for SuperDARN radars to detect ionospheric, ground, or meteor backscatter, the transmitted radio waves traverse the *D* region multiple times and thus undergo significant attenuation when the *D* region is enhanced. Based on the results presented in Figures 5 and 7, which show one-way attenuation, one could reasonably expect 12-MHz waves to undergo a total of 20- to 30-dB attenuation as they propagate to ionospheric scattering targets and back to the radar. Since the SuperDARN backscatter power parameter typically ranges from 0 to 30 dB, this degree of attenuation would extinguish most or all of the backscatter. Therefore, the attenuation values derived from the SuperDARN noise measurements are consistent with the observed backscatter loss.

In Figure 5 we compared the PCA observed by the Rankin Inlet SuperDARN radar and the Taloyoak riometer. Qualitatively, the radar and riometer observations exhibit similar behavior in terms of the dayside (nightside) attenuation maxima (minima), and also the shape of the amplitude envelope. However, there are also some key differences in the two data sets. For example, the RKN radar detects enhanced attenuation on the nightside during Event 1, but the TALO riometer detects no obvious enhancement. Also, the first two dayide attenuation peaks during Event 2 have significantly different amplitudes. We identify several potential contributors to the differences between the radar- and riometer-derived attenuation measurements:

1. the ~750 km spatial separation between the RKN radar and the TALO riometer;
2. the use of equation (2) to scale the attenuation data to a common frequency;
3. the high variability of the atmospheric noise used for determining the radar attenuation values;
4. differences in the methods used to baseline the radar and riometer data sets (quiet day curve determination).

The spatial separation between the RKN radar and the TALO riometer is unlikely to be a major contributor, because PCA is a large-scale event affecting the entire polar cap. Also, both the radar and the riometer have wide antenna gain patterns, reducing the effect of the station separation. The other factors listed above, however, may be significant. We chose to scale the radar and riometer data to common frequencies using the nondeviative absorption relationship (equation (2) from magnetoionic theory, but empirical relationships also exist in the literature. For example, Sauer and Wilkinson (2008) showed that dayside 10- to 50-MHz PCA varies with frequency as $f^{-1.5}$. Patterson et al. (2001) showed that the frequency exponent is dependent on the particle energy, ranging from −1.2 to −1.8. Other studies have validated the f^{-2} relationship from magnetoionic theory (Rosenberg et al., 1991). For CNA due to solar flares, Schumer (2009) determined an $f^{-1.24}$ relationship. These exponents produce significantly different attenuation values when scaling from 10–15 MHz to 30 MHz. For example, 8-dB attenuation measured at 12 MHz is equivalent to 1.3 dB at 30 MHz using an f^{-2} relationship, or 2.7 dB using an $f^{-1.2}$ relationship. However, there is no single exponent that would account for the differences between the radar and riometer data presented in Figure 5. This is because the TALO riometer consistently measures lower levels of attenuation compared to the RKN radar during Event 1, but for Event 2 the riometer values are, in general, higher than the radar measurements during the day and lower at night.

We suggest that both items (3) and (4) from the above list are responsible for the observed attenuation differences in Figure 5. A variety of methods exist for producing riometer QDCs, and so the particular CNA curve obtained after baselining can vary significantly. Additionally, the high variability of atmospheric noise introduces a source of error into the SuperDARN QDCs that does not apply to riometer QDCs derived from cosmic noise. In particular, it is not possible to distinguish between reduced production of atmospheric noise and increased attenuation based on SuperDARN noise measurements alone. This highlights the importance of considering the instantaneous echo occurrence together with the noise measurements to confirm that attenuation has taken place, since reduced atmospheric noise production would not cause backscatter loss.

7. Conclusion

We have demonstrated that SuperDARN radars can be used to observe the spatial and temporal evolution of 10- to 15-MHz polar cap absorption by utilizing routine background noise measurements. PCA is identified in the SuperDARN data set as a combination of reduced background noise and near-total loss of backscatter

lasting for several days. Following methods used in riometry, we produced QDCs describing the SuperDARN atmospheric noise for undisturbed conditions and estimated the degree of attenuation relative to these QDCs. For our two case study PCA events in September 2017, attenuation up to 10 dB at 12 MHz was detected within the northern polar cap, and up to 14 dB in the southern polar cap. Radar-derived attenuation values from Rankin Inlet agree qualitatively with CNA measurements from the Taloyoak riometer. In addition to the PCA, brief attenuation enhancements lasting 2–4 hr were observed at midlatitudes, consistent with previous SuperDARN observations of shortwave fadeout caused by solar X-ray flares. We emphasize that the SuperDARN noise measurement is available for every scan and can therefore be used to measure HF attenuation even during intervals of backscatter loss when the primary SuperDARN data products cannot be determined.

Acknowledgments
This study was supported by the Research Council of Norway/CoE under contract 223252/F50. The SuperDARN data were obtained from the British Antarctic Survey data mirror (https://www.bas.ac.uk/project/superdarn). SuperDARN is a collection of radars funded by the national scientific funding agencies of Australia, Canada, China, France, Japan, Norway, South Africa, United Kingdom, and United States of America. The GO Canada (previously NORSTAR) riometer array is operated by the University of Calgary with financial support from the Canadian Space Agency. All riometer data are openly available from data.phys.ucalgary.ca. The authors also acknowledge NOAA for the GOES proton flux data (https://www.ngdc.noaa.gov/stp/satellite/goes/dataaccess.html).

References

Bailey, D. K. (1964). Polar-cap absorption. *Planetary and Space Science*, *12*(5), 495–541. https://doi.org/10.1016/0032-0633(64)90040-6

Baker, J. B. H., Greenwald, R. A., Ruohoniemi, J. M., Oksavik, K., Gjerloev, J. W., Paxton, L. J., et al. (2007). Observations of ionospheric convection from the Wallops SuperDARN radar at middle latitudes. *Journal of Geophysical Research*, *112*, A01303. https://doi.org/10.1029/2006JA011982

Berngardt, O. I., Ruohoniemi, J. M., Nishitani, N., Shepherd, S. G., Bristow, W. A., & Miller, E. S. (2018). Attenuation of decameter wavelength sky noise during X-ray solar flares in 2013–2017 based on the observations of midlatitude HF radars. *Journal of Atmospheric and Solar-Terrestrial Physics*, *173*, 1–13. https://doi.org/10.1016/j.jastp.2018.03.022

Bland, E. C., McDonald, A. J., de Larquier, S., & Devlin, J. C. (2014). Determination of ionospheric parameters in real time using SuperDARN HF radars. *Journal of Geophysical Research: Space Physics*, *119*, 5830–5846. https://doi.org/10.1002/2014JA020076

Bristow, W. A., Greenwald, R. A., & Villain, J. P. (1996). On the seasonal dependence of medium-scale atmospheric gravity waves in the upper atmosphere at high latitudes. *Journal of Geophysical Research*, *101*(A7), 15,685–15,699. https://doi.org/10.1029/96JA01010

Bristow, W. A., & Jensen, P. (2007). A superposed epoch study of SuperDARN convection observations during substorms. *Journal of Geophysical Research*, *112*, A06232. https://doi.org/10.1029/2006JA012049

Brodrick, D., Tingay, S., & Wieringa, M. (2005). X-ray magnitude of the 4 November 2003 solar flare inferred from the ionospheric attenuation of the galactic radio background. *Journal of Geophysical Research*, *110*, A09S36. https://doi.org/10.1029/2004JA010960

Chakraborty, S., Ruohoniemi, J. M., Baker, J. B. H., & Nishitani, N. (2018). Characterization of short-wave fadeout seen in daytime SuperDARN ground scatter observations. *Radio Science*, *53*, 472–484. https://doi.org/10.1002/2017RS006488

Chisham, G., Lester, M., Milan, S. E., Freeman, M. P., Bristow, W. A., Grocott, A., et al. (2007). A decade of the Super Dual Auroral Radar Network (SuperDARN): Scientific achievements, new techniques and future directions. *Surveys in Geophysics*, *28*, 33–109. https://doi.org/10.1007/s10712-007-9017-8

Currie, J. L., Waters, C. L., Menk, F. W., Sciffer, M. D., & Bristow, W. A. (2016). SuperDARN backscatter during intense geomagnetic storms. *Radio Science*, *51*(6), 814–825. https://doi.org/10.1002/2016RS005960

Danskin, D. W., Koustov, A. V., Ogawa, T., Nishitani, N., Nozawa, S., Milan, S. E., et al. (2002). On the factors controlling occurrence of *F*-region coherent echoes. *Annales de Geophysicae*, *20*(9), 1385–1397. https://doi.org/10.5194/angeo-20-1385-2002

Davies, K. (1990). *Ionospheric Radio*, no 31 in IEE electromagneitc waves series. London: Peter Peregrinus Ltd.

Ferguson, D. C., Worden, S. P., & Hastings, D. E. (2015). The space weather threat to situational awareness, communications, and positioning systems. *IEEE Transactions on Plasma Science*, *43*(9), 3086–3098. https://doi.org/10.1109/TPS.2015.2412775

Fiori, R., & Danskin, D. (2016). Examination of the relationship between riometer-derived absorption and the integral proton flux in the context of modeling polar cap absorption. *Space Weather*, *14*, 1032–1052. https://doi.org/10.1002/2016SW001461

Frissell, N. A., Miller, E. S., Kaeppler, S. R., Ceglia, F., Pascoe, D., Sinanis, N., et al. (2014). Ionospheric sounding using real-time amateur radio reporting networks. *Space Weather*, *12*, 651–656. https://doi.org/10.1002/2014SW001132

Garcia-Rigo, A., Hernández-Pajares, M., Juan, J. M., & Sanz, J. (2007). Solar flare detection system based on global positioning system data: First results. *Advances in Space Research*, *39*(5), 889–895. https://doi.org/10.1016/j.asr.2006.09.031

Gauld, J. K., Yeoman, T. K., Davies, J. A., Milan, S. E., & Honary, F. (2002). SuperDARN radar HF propagation and absorption response to the substorm expansion phase. *Annales de Geophysicae*, *20*(10), 1631–1645. https://doi.org/10.5194/angeo-20-1631-2002

Gillies, R. G., Hussey, G. C., Sofko, G. J., McWilliams, K. A., Fiori, R. A. D., Ponomarenko, P., et al. (2009). Improvement of SuperDARN velocity measurements by estimating the index of refraction in the scattering region using interferometry. *Journal of Geophysical Research*, *114*, A07305. https://doi.org/10.1029/2008JA013967

Gillies, R. G., Hussey, G. C., Sofko, G. J., Ponomarenko, P. V., & McWilliams, K. A. (2011). Improvement of HF coherent radar line-of-sight velocities by estimating the refractive index in the scattering volume using radar frequency shifting. *Journal of Geophysical Research*, *116*, A01302. https://doi.org/10.1029/2010JA016043

Giordano, A. A., & Haber, F. (1972). Modeling of atmospheric noise. *Radio Science*, *7*(11), 1011–1023. https://doi.org/10.1029/RS007i011p01011

Goodman, J. M. (2005). Operational communication systems and relationships to the ionosphere and space weather. *Advances in Space Research*, *36*(12), 2241–2252.

Greenwald, R. A., Baker, K. B., Dudeney, J. R., Pinnock, M., Jones, T. B., Thomas, E. C., et al. (1995). DARN/SuperDARN: A global view of the dynamics of high-latitude convection. *Space Science Reviews*, *71*, 761–796. https://doi.org/10.1007/BF00751350

Greenwald, R. A., Baker, K. B., Hutchins, R. A., & Hanuise, C. (1985). An HF phased-array radar for studying small-scale structure in the high-latitude ionosphere. *Radio Science*, *20*, 63–79. https://doi.org/10.1029/RS020i001p00063

Hargreaves, J., Ranta, H., Ranta, A., Turunen, E., & Turunen, T. (1987). Observations of the polar cap absorption event of February 1984 by the EISCAT incoherent scatter radar. *Planetary and space science*, *35*(7), 947–958. https://doi.org/10.1016/0032-0633(87)90072-9

Hargreaves, J. K., Shirochkov, A. V., & Farmer, A. D. (1993). The polar cap absorption event of 19–21 March 1990: Recombination coefficients, the twilight transition and the midday recovery. *Journal of Atmospheric and Terrestrial Physics*, *55*(6), 857–862. https://doi.org/10.1016/0021-9169(93)90026-U

Headrick, J. M., & Anderson, S. J. (2008). *Radar Handbook*, chap. HF over-the-horizon radar (vol. 34, pp. 24.1–24.43). New York: McGraw-Hill.

Hughes, J. M., Bristow, W. A., Greenwald, R. A., & Barnes, R. J. (2002). Determining characteristics of HF communications links using SuperDARN. *Annales de Geophysicae*, *20*, 1023–1030. https://doi.org/10.5194/angeo-20-1023-2002

Jones, J. B. L., Bentley, R. D., Hunter, R., Iles, R. H. A., Taylor, G. C., & Thomas, D. J. (2005). Space weather and commercial airlines. *Advances in Space Research*, *36*(12), 2258–2267. https://doi.org/10.1016/j.asr.2004.04.017

Kallenrode, M.-B. (2003). Current views on impulsive and gradual solar energetic particle events. *Journal of Physics G: Nuclear and Particle Physics*, *29*(5), 965. https://doi.org/10.1088/0954-3899/29/5/316

Kavanagh, A. J., Marple, S. R., Honary, F., McCrea, I. W., & Senior, A. (2004). On solar protons and polar cap absorption: constraints on an empirical relationship. *Annales de Geophysicae*, *22*(4), 1133–1147. https://doi.org/10.5194/angeo-22-1133-2004

Knipp, D. J., Ramsay, A. C., Beard, E. D., Boright, A. L., Cade, W. B., Hewins, I. M., et al. (2016). The May 1967 great storm and radio disruption event: Extreme space weather and extraordinary responses. *Space Weather*, *14*, 614–633. https://doi.org/10.1002/2016SW001423

Kossey, P. A., Turtle, J. P., Pagliarulo, R. P., Klemetti, W. I., & Rasmussen, J. E. (1983). VLF reflection properties of the normal and disturbed polar ionosphere in northern Greenland. *Radio science*, *18*(6), 907–916. https://doi.org/10.1029/RS018i006p00907

Kress, B. T., Mertens, C. J., & Wiltberger, M. (2010). Solar energetic particle cutoff variations during the 29–31 October 2003 geomagnetic storm. *Space Weather*, *8*, S05001. https://doi.org/10.1029/2009SW000488

Lester, M. (2013). The Super Dual Auroral Radar Network (SuperDARN): An overview of its development and science. *Advances in Polar Science*, *24*, 1–11.

Little, C. G., & Leinbach, H. (1959). The riometer—A device for the continuous measurement of ionospheric absorption. *Proceedings of the IRE*, *47*(2), 315–320. https://doi.org/10.1109/JRPROC.1959.287299

Mendillo, M., & Evans, J. V. (1974). Incoherent scatter observations of the ionospheric response to a large solar flare. *Radio Science*, *9*(2), 197–203. https://doi.org/10.1029/RS009i002p00197

Milan, S., Davies, J., & Lester, M. (1999). Coherent HF radar backscatter characteristics associated with auroral forms identified by incoherent radar techniques: A comparison of CUTLASS and EISCAT observations. *Journal of Geophysical Research*, *104*(A10), 22,591–22,604. https://doi.org/10.1029/1999JA900277

Milan, S. E., Hosokawa, K., Lester, M., Sato, N., Yamagishi, H., & Honary, F. (2008). D region HF radar echoes associated with energetic particle precipitation and pulsating aurora. *Annales de Geophysicae*, *26*(7), 1897–1904. https://doi.org/10.5194/angeo-26-1897-2008

Milan, S. E., Jones, T. B., Robinson, T. R., Thomas, E. C., & Yeoman, T. K. (1997). Interferometric evidence for the observation of ground backscatter originating behind the CUTLASS coherent HF radars. *Annales de Geophysicae*, *15*(1), 29–39. https://doi.org/10.1007/s00585-997-0029-y

NASA, GOES N Data book (2006). CDRL PM-1-1-03, Revision B, February 2005. Retrieved from https://goes.gsfc.nasa.gov/text/goes.databookn.html

Patterson, J. D., Armstrong, T. P., Laird, C. M., Detrick, D. L., & Weatherwax, A. T. (2001). Correlation of solar energetic protons and polar cap absorption. *Journal of Geophysical Research*, *106*(A1), 149–163. https://doi.org/10.1029/2000JA002006

Ponomarenko, P. V., Iserhienrhien, B., & St.-Maurice, J.-P. (2016). Morphology and possible origins of near-range oblique HF backscatter at high and midlatitudes. *Radio Science*, *51*(6), 718–730. https://doi.org/10.1002/2016RS006088

Ponomarenko, P. V., Koustov, A. V., St-Maurice, J. P., & Wiid, J. (2011). Monitoring the *F*-region peak electron density using HF backscatter interferometry. *Geophysical Research Letters,38*, L21102. https://doi.org/10.1029/2011GL049675

Ponomarenko, P. V., Menk, F. W., & Waters, C. L. (2003). Visualization of ULF waves in SuperDARN data. *Geophysical Research Letters*, *30*(18), 1926. https://doi.org/10.1029/2003GL017757

Ranta, H., Yamagishi, H., & Stauning, P. (1995). Twilight anomaly, midday recovery and cutoff latitudes during the intense polar cap absorption event of March 1991. *Annales de Geophysicae*, *13*(3), 262–276. https://doi.org/10.1007/s00585-995-0262-1

Reames, D. V. (1999). Particle acceleration at the Sun and in the heliosphere. *Space Science Reviews*, *90*(3-4), 413–491. https://doi.org/10.1023/A:1005105831781

Reid, G. C., & Leinbach, H. (1959). Low-energy cosmic-ray events associated with solar flares. *Journal of Geophysical Research*, *64*(11), 1801–1805. https://doi.org/10.1029/JZ064i011p01801

Reid, G., & Leinbach, H. (1961). Morphology and interpretation of the great polar cap absorption events of May and July, 1959. *Journal of Atmospheric and Terrestrial Physics*, *23*, 216–228. https://doi.org/10.1016/0021-9169(61)90047-2

Ribeiro, A. J., Ruohoniemi, J. M., Ponomarenko, P. V., Clausen, L. B. N., Baker, J. B. H., Greenwald, R. A., et al. (2013). A comparison of SuperDARN ACF fitting methods. *Radio Science*, *48*(3), 274–282. https://doi.org/10.1002/rds.20031

Rosenberg, T. J., Detrick, D. L., Venkatesan, D., & van Bavel, G. (1991). A comparative study of imaging and broad-beam riometer measurements: The effect of spatial structure on the frequency dependence of auroral absorption. *Journal of Geophysical Research*, *96*(A10), 17,793–17,803. https://doi.org/10.1029/91JA01827

Rostoker, G., Samson, J. C., Creutzberg, F., Hughes, T. J., McDiarmid, D. R., McNamara, A. G., et al. (1995). CANOPUS—A ground-based instrument array for remote sensing the high latitude ionosphere during the ISTP/GGS program. *Space Science Reviews*, *71*(1), 743–760. https://doi.org/10.1007/BF00751349

Ruohoniemi, J. M., & Baker, K. B. (1998). Large-scale imaging of high-latitude convection with Super Dual Auroral Radar Network HF radar observations. *Journal of Geophysical Research*, *103*(A9), 20,797–20,811. https://doi.org/10.1029/98JA01288

Sarno-Smith, L. K., Kosch, M. J., Yeoman, T., Rietveld, M., Nel, A., & Liemohn, M. W. (2016). Ionospheric electron number densities from CUTLASS dual-frequency velocity measurements using artificial backscatter over EISCAT. *Journal of Geophysical Research: Space Physics*, *121*, 8066–8076. https://doi.org/10.1002/2016JA022788

Sauer, H. H., & Wilkinson, D. C. (2008). Global mapping of ionospheric HF/VHF radio wave absorption due to solar energetic protons. *Space Weather*, *6*, S12002. https://doi.org/10.1029/2008SW000399

Schumer, E. A. (2009). Improved modeling of midlatitude *D*-region ionospheric absorption of high frequency radio signals during solar X-ray flares (Ph.D. thesis), Air Force Institute of Technology Wright-Patterson Air Force Base, Ohio, USA. http://www.dtic.mil/dtic/tr/fulltext/u2/a516063.pdf

Sterne, K. T., Greenwald, R. A., Baker, J. B. H., & Ruohoniemi, J. M. (2011). Modeling of a twin terminated folded dipole antenna for the Super Dual Auroral Radar Network (SuperDARN). In *Radar Conference (RADAR), 2011 IEEE*, pp. 934–938. https://doi.org/10.1109/RADAR.2011.5960673

Watanabe, D., & Nishitani, N. (2013). Study of ionospheric disturbances during solar flare events using the SuperDARN Hokkaido radar. *Advances in Polar Science*, *24*(1), 12–18.

Wenzel, D., Jakowski, N., Berdermann, J., Mayer, C., Valladares, C., & Heber, B. (2016). Global ionospheric flare detection system (GIFDS). *Journal of Atmospheric and Solar-Terrestrial Physics*, *138*, 233–242. https://doi.org/10.1016/j.jastp.2015.12.011

PAPER II

Heino, E., Verronen, P. T., Kero, A., Kalakoski, N., & Partamies, N. (2019). Cosmic noise absorption during solar proton events in WACCM-D and riometer observations. *Journal of Geophysical Research: Space Physics*, 124(2), 1,361–1,376. https://doi.org/10.1029/2018JA026192

JGR Space Physics

RESEARCH ARTICLE
10.1029/2018JA026192

Cosmic Noise Absorption During Solar Proton Events in WACCM-D and Riometer Observations

Erkka Heino[1,2], **Pekka T. Verronen**[3], **Antti Kero**[4], **Niilo Kalakoski**[3], **and Noora Partamies**[1,5]

[1]Department of Arctic Geophysics, The University Centre in Svalbard, Longyearbyen, Norway, [2]Department of Physics and Technology, University of Tromsø, Tromsø, Norway, [3]Space and Earth Observation Centre, Finnish Meteorological Institute, Helsinki, Finland, [4]Sodankylä Geophysical Observatory, University of Oulu, Sodankylä, Finland, [5]Birkeland Centre for Space Science, Bergen, Norway

Key Points:
- CNA during 62 SPEs was studied with WACCM-D and riometer observations
- CNA is modeled well on average and in individual events with a nonlinearity correction for high levels of CNA
- The fixed proton cutoff latitude in WACCM-D at 60 degrees leads to overestimation of the extent of the CNA, especially in small to moderate SPEs

Correspondence to:
E. Heino,
erkkah@unis.no

Citation:
Heino, E., Verronen, P. T., Kero, A., Kalakoski, N., & Partamies, N. (2019). Cosmic noise absorption during solar proton events in WACCM-D and riometer observations. *Journal of Geophysical Research: Space Physics*, *124*. https://doi.org/10.1029/2018JA026192

Received 11 OCT 2018
Accepted 13 JAN 2019
Accepted article online 18 JAN 2019

Abstract Solar proton events (SPEs) cause large-scale ionization in the middle atmosphere leading to ozone loss and changes in the energy budget of the middle atmosphere. The accurate implementation of SPEs and other particle ionization sources in climate models is necessary to understand the role of energetic particle precipitation in climate variability. We use riometer observations from 16 riometer stations and the Whole Atmosphere Community Climate Model with added *D* region ion chemistry (WACCM-D) to study the spatial and temporal extent of cosmic noise absorption (CNA) during 62 SPEs from 2000 to 2005. We also present a correction method for the nonlinear response of observed CNA during intense absorption events. We find that WACCM-D can reproduce the observed CNA well with some need for future improvement and testing of the used energetic particle precipitation forcing. The average absolute difference between the model and the observations is found to be less than 0.5 dB poleward of about 66° geomagnetic latitude, and increasing with decreasing latitude to about 1 dB equatorward of about 66° geomagnetic latitude. The differences are largest during twilight conditions where the modeled changes in CNA are more abrupt compared to observations. An overestimation of about 1° to 3° geomagnetic latitude in the extent of the CNA is observed due to the fixed proton cutoff latitude in the model. An unexplained underestimation of CNA by the model during sunlit conditions is observed at stations within the polar cap during 18 of the studied events.

1. Introduction

Solar proton events (SPEs) are large, albeit infrequent, expulsions of energetic particles from the Sun that can last from a few hours to multiple days. A SPE is defined as a period of time where the ≥10-MeV integral proton flux, measured by a geosynchronous satellite, exceeds 10 pfu (particle flux unit, $cm^{-2}{\cdot}s^{-1}{\cdot}sr^{-1}$). The dominant particle species in SPEs is protons, which are accelerated near the Sun to energies of 10 keV/nucl to multiple GeV/nucl (Kallenrode, 2003) by solar flares and coronal mass ejection-driven shocks (e.g., Reames, 1999). The acceleration processes get their energy from the magnetic energy stored in the solar corona, but the exact acceleration mechanisms are still being discussed (Vainio et al., 2009). High-energy SPE protons and electrons, as well as energetic electrons from the outer radiation belt, have access to the mesosphere and upper stratosphere in the magnetic polar regions affecting the neutral composition and dynamics of the middle atmosphere (Sinnhuber et al., 2012; Verronen & Lehmann, 2013).

Ionization in the middle atmosphere due to energetic particle precipitation (EPP) causes production of odd hydrogen (HO_x) and odd nitrogen (NO_x) species that lead to the loss of ozone (O_3) through catalytic ozone loss cycles. Odd hydrogen species have a short chemical lifetime and an effect on ozone loss in the mesosphere. Odd nitrogen species are destroyed in the sunlit atmosphere and thus have a long lifetime during the polar winter. Due to its long chemical lifetime in the dark atmosphere, NO_x is subject to transport in the middle atmosphere and has an important effect on stratospheric ozone loss (Randall et al., 2005). Funke et al. (2014) showed from MIPAS/Envisat observations that EPP-produced reactive reservoir nitrogen species (NO_y) descent regularly down into the stratosphere during polar winter. A NO_2 increase of several hundred percent and an O_3 decrease of tens of percent between 36- and 60-km altitude, due to the SPEs of October–November 2003, were reported by Seppälä et al. (2004) based on GOMOS/Envisat observations. This SPE effect on the NO_2 and O_3 concentrations was observed to last several months after the SPEs. Ozone

Table 1
Names, Locations, and Operating Frequencies of Riometers Used in This Study

Station name and code	Latitude	Longitude	Frequency (MHz)
European chain:			
Longyearbyen (LYR)	75.18° (78.20°)	111.11° (15.82°)	38.2
Hornsund (HOR)	74.05° (77.00°)	108.77° (15.60°)	30.0
Kilpisjärvi (KIL)	65.82° (69.05°)	103.54° (20.79°)	38.2
Abisko (ABI)	65.25° (68.40°)	101.59° (18.90°)	30.0
Ivalo (IVA)	65.01° (68.55°)	108.34° (27.28°)	29.9
Sodankylä (SOD)	63.90° (67.42°)	106.89° (26.39°)	30.0
Rovaniemi (ROV)	63.26° (66.78°)	106.13° (25.94°)	32.4
Oulu (OUL)	61.51° (65.08°)	105.15° (25.90°)	30.0
Jyväskylä (JYV)	58.77° (62.42°)	103.34° (25.28°)	32.4
Canadian chain:			
Taloyoak (TAL)	78.62° (69.54°)	−30.04° (266.44°)	30.0
Rankin Inlet (RAN)	72.53° (62.82°)	−24.84° (267.89°)	30.0
Eskimo Point (ESK)	70.80° (61.11°)	−27.70° (265.95°)	30.0
Fort Churchill (CHU)	68.57° (58.76°)	−27.27° (265.91°)	30.0
Gillam (GIL)	66.25° (56.38°)	−27.73° (265.36°)	30.0
Island Lake (ISL)	63.82° (53.86°)	−27.40° (265.34°)	30.0
Pinawa (PIN)	60.13° (50.20°)	−29.00° (263.96°)	30.0

Note. Locations are in geomagnetic coordinates with geodetic coordinates in parentheses.

is the dominant absorber of ultraviolet radiation in the atmosphere and therefore important in the energy budget of the middle atmosphere. Changes in ozone concentrations in the stratosphere have been shown to affect ground-level climate variability especially in the polar regions (Gillett & Thompson, 2003). As EPP affects ozone variability in the middle atmosphere, a similar ground-level coupling effect has been suggested and possible ground-level signatures have been observed and modeled (Baumgaertner et al., 2011; Seppälä et al., 2009). The implementation of EPP ionization in climate models is therefore necessary to understand the role of EPP in climate variability on longer timescales (Andersson et al., 2014; Matthes et al., 2017).

Increased ionization due to EPP causes absorption of high-frequency radio waves in the polar *D* region, which has been measured with riometers since the 1950s (Little & Leinbach, 1958, 1959). Riometers are passive instruments that measure cosmic radio noise continuously, typically at 30- to 40-MHz frequency. Absorption of radio waves, or cosmic noise absorption (CNA), in the ionosphere is determined with riometers from the difference between the measured radio noise and a quiet day curve (QDC), which is the expected level of radio noise without absorption—that is, during a "quiet" day.

In this paper, we use riometer observations and the Whole Atmosphere Community Climate Model with added *D* region ion chemistry (WACCM-D) to study the spatial and temporal extent of CNA caused by SPEs, the effect of geomagnetic cutoff on the CNA, and the ability of the WACCM-D model to reproduce the level and time behavior of observed CNA during SPEs. The nonlinear response of riometers to high levels of CNA is also presented and discussed.

2. Observational Data

The used observational data cover 62 SPEs from 2000 to 2005, whose occurrence times were taken from the SPE list at `ftp://ftp.swpc.noaa.gov/pub/indices/SPE.txt` updated by the National Oceanic and Atmospheric Administration. The studied 62 SPEs (see Tables A1 and A2) were chosen based on availability of data from the Longyearbyen and Kilpisjärvi imaging riometers. The data set consists of 34 S1-class (maximum ≥10-MeV integral proton flux ≥ 10 pfu), 17 S2-class (≥100 pfu), 6 S3-class (≥1,000 pfu), and 5 S4-class (≥10,000 pfu) SPEs. The number of available stations varies within the used events.

The used riometer CNA data are from two arrays of riometers in northern Europe and Canada (see Table 1 and Figure 1). The riometers in the European sector are the Sodankylä Geophysical Observatory (SGO)

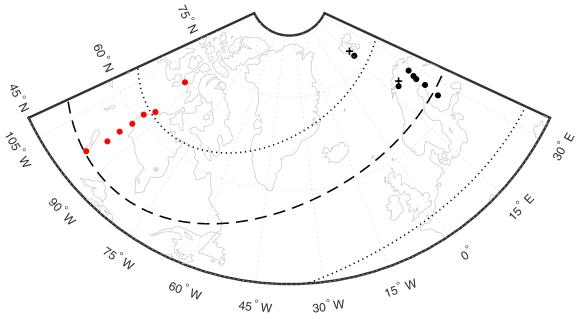

Figure 1. Geographical locations of the riometers used in the study and the limits of the solar proton event and medium-energy electron ionization in the used model. The Canadian GO-Canada chain riometers are marked with red dots, the Sodankylä Geophysical Observatory riometers with black dots, and the two imaging riometers with black crosses. The upper and lower limits (72° and 45° geomagnetic latitude) of the medium-energy electron ionization are marked with the black dotted lines, and the lower limit of the solar proton event ionization is marked with the black dashed line.

wide-beam riometer network spanning from Jyväskylä, Finland, to Hornsund, Svalbard, and imaging riometers located at Kilpisjärvi, Finland (Browne et al., 1995), and Longyearbyen, Svalbard (Stauning & Hisao, 1995). The Canadian sector riometers are the Churchill line stations of the GO-Canada (formerly NORSTAR) wide-beam riometer array (Rostoker et al., 1995).

The SGO and GO-Canada wide-beam riometers are analog La Jolla receivers with a dual half-wavelength dipole antenna that produces a single 60° beam toward the local zenith (Spanswick et al., 2005). The QDCs for the SGO riometers have been calculated with an automated method that fits a sinusoidal curve to data from the previous ten days to calculate the QDC for the next day. The QDC is calculated separately for each station. SGO data during winter months of 2000 to 2003 (27 events in total) were excluded from this study due to data being corrupted by unknown daily radio interference. The GO-Canada baselining method is based on characterizing the shape of the cosmic background noise rather than fitting a curve to a specific subset of data and is described in detail online at `http://aurora.phys.ucalgary.ca/GO-Canada/rio/doc/CANOPUS_Riometer_Baselining.pdf`. Time resolution of the SGO data is 1 min, and the time resolution of the GO-Canada data is 5 s.

The Kilpisjärvi imaging riometer (Imaging Riometer for Ionospheric Studies, IRIS) produces 49 narrow directional beams including a beam directed at the local zenith with a beam width of 13° (Browne et al., 1995). The QDC is produced separately for each beam by finding the largest value received without interference and absorption events for any point of time of a sidereal day. Observations from a time period of 14 days is usually used for the QDC determination. CNA measurements from the middle beam of the riometer was used in this study to produce a comparable beam to the modeled zenithal CNA. The time resolution of IRIS is 1 s, but the data were provided as 5-min median values.

The imaging riometer in Longyearbyen produces 64 narrow directional beams. The QDC is determined for each beam separately by superimposing 10 to 20 days of observations near and including the day of interest into a mass plot, and determining the upper level of undisturbed observations visually (Stauning & Hisao, 1995). As the riometer does not have a beam directed at the local zenith, CNA measurements from the four middle beams of the imaging riometer are combined into a single CNA value by taking the mean of the beam values if there are one or two measured values. If there are three or four values, the maximum and minimum values are discarded, and the mean is taken from the remaining values. The time resolution of the Longyearbyen data is 1 min.

Data from all riometers were averaged to have a 5-min time resolution and checked manually. Times with clear abrupt level changes, QDC problems, and other clear radio interference were removed. The data were then averaged to 1-hr time resolution to match the time resolution of the WACCM-D model. The mean values of the standard error from averaging the data from 5-min resolution into 1-hr resolution is less than 0.05 dB for all stations. The absorption measured by riometers not operating at 30 MHz was converted to 30-MHz equivalent absorption using the generalized magnetoionic theory f^{-2} dependence of absorption and operating frequency (Friedrich et al., 2002). It should be noted that the frequency dependence deviates from the inverse square relationship when strong spatial gradients of absorption regions are in the riometer beam and at altitudes below about 70-km altitude where the effective electron-neutral collision frequency becomes comparable with, or much greater than, the effective angular radio frequency (Rosenberg et al., 1991). Despite these caveats, the simple inverse square dependence was used, as the frequency dependence in the model CNA calculation method is close to the inverse square relationship.

Proton flux measurements during the studied SPEs are from the Space Environment Monitor instrument package of the National Oceanic and Atmospheric Administration Geostationary Operational Environmental Satellite (GOES) system satellites. Due to the long time period of the study, data from two different GOES satellites had to be used. GOES-8 data were used for years 2000 to 2002, and GOES-10 data for years

Table 2
WACCM-D Output Data Used in This Study

Data product	Time resolution
Neutral temperature (K)	Hourly
Electron mixing ratio, ppv	Hourly
O mixing ratio, ppv	Hourly
H mixing ratio, ppv	Hourly
O_2 mixing ratio, ppv	Monthly
N_2 mixing ratio, ppv	Monthly

2003 to 2005. Proton flux data from the >10-MeV integral proton flux channel (I3) was used to determine the durations of the SPEs.

3. Modeling

WACCM-D is a variant of the global 3-D climate model, WACCM, with added *D* region ion chemistry. The aim of the added *D* region chemistry is to better reproduce the effects of EPP on the neutral atmospheric constituents in the mesosphere and upper stratosphere. For a comprehensive description of WACCM-D and its lower ionospheric performance, see Verronen et al. (2016). Andersson et al. (2016) showed that the addition of *D* region ion chemistry into WACCM significantly improves modeling of polar HNO_3, HCl, ClO, OH, and NO_x and that WACCM-D can model atmospheric effects of the January 2005 SPE (event 58 in this study, max 5,040 pfu) as compared to Aura/MLS observations.

SD-WACCM-D (WACCM4) was run for the time periods of the 62 SPEs examined in this study with preconfigured specified dynamics driven by MERRA 19 × 2 (Rienecker et al., 2011) meteorological fields for the year 2000 with a 6-hr time resolution. The specified dynamics force the model at altitudes below 50 km at every dynamics time step by 10%, while model dynamics are fully interactive above 60 km. Between 50- and 60-km altitude, the forcing transitions linearly from forcing to no forcing (Kunz et al., 2011). The model runs span the altitude range from the Earth's surface to the thermosphere ($4.5 \cdot 10^{-6}$ hPa, ≈140 km) with 88 vertical pressure levels. The latitudinal resolution of the model runs is 1.9°, and the longitudinal resolution is 2.5°. The specified dynamics-driven SD-WACCM-D that was used in this study is referred to as WACCM-D in the rest of this article.

Ionization sources in the used version of WACCM-D include solar protons, energetic radiation belt electrons, solar extreme ultraviolet radiation (EUV), Lyman-α, auroral electrons, and galactic cosmic rays (GCRs). Hourly solar proton ionization rates were used in the model runs for the SPE protons. SPE ionization was applied uniformly to geomagnetic latitudes larger than 60°. The solar proton ionization rates are determined in the same way from GOES proton flux measurements as the daily ionization rates published by Jackman et al. (2005), but with a higher time resolution. For an overview of the daily SPE ionization rate determination, see Jackman (2013). Ionization rates for energetic radiation belt electrons (30–1,000 keV) were implemented from the medium-energy electron (MEE) model by van de Kamp et al. (2016). The MEE model is based on precipitation data from low Earth orbiting POES satellites and an empirically described plasmasphere structure. The MEE model can use the *Dst* or the *Ap* index as an input and calculates the energy-flux spectrum of precipitating electrons with a time resolution of 1 day. In this study, we used the *Ap*-driven model. The forcing from the MEE model includes electrons with energies from 30 to 1,000 keV, which precipitate into 16 geomagnetic latitude bins between 45° and 72°. Other ionization sources used in the model runs were standard WACCM ionization sources, that is, solar EUV radiation, GCRs, auroral electrons, and solar Lyman-α (see Marsh et al., 2007; Smith-Johnsen et al., 2018). The time resolutions of the EUV and Lyman-α ionization sources are 1 day, and the time resolution of the auroral electron ionization source is 3 hr. The Nowcast of Atmospheric Ionising Radiation for Aviation Safety (NAIRAS) model is used in the simulation as the GCR ionization source (Jackman et al., 2016). The inclusion of GCR ionization in the model is necessary to provide an ion source for the *D* region chemistry at low latitudes.

The time resolution of the used WACCM-D output data is 1 hr or 1 month, depending on the atmospheric quantity. One-hour-resolution data are output by WACCM-D as a snapshot of the model state every hour at every model grid point and pressure level. Monthly data are output as a monthly mean of the wanted quantity at every model grid point and pressure level. The output data used in this study and their time resolutions are listed in Table 2.

To convert the atmospheric conditions in the WACCM-D model into CNA, differential CNA (dB/km) was calculated from WACCM-D output with the method by Sen and Wyller (1960). The required electron collision frequencies with different neutral species (N_2, O_2, O, and H) were calculated from WACCM-D data following Banks and Kockarts (1973), part A, p. 194. This approach has been previously used with Sodankylä Ion-Neutral Chemistry (SIC) model data (e.g., Clilverd et al., 2007; Verronen et al., 2006). WACCM-D does not provide electron temperature separately; thus, it was assumed to be the same as the neutral temperature,

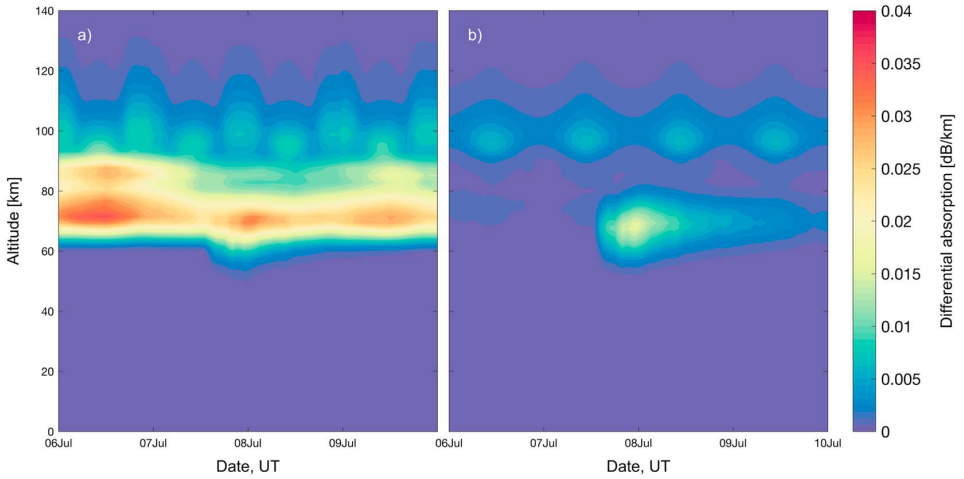

Figure 2. Modeled differential cosmic noise absorption during the 7 July 2002 solar proton event (event 43, max 22 pfu) in (a) Sodankylä and (b) Longyearbyen. Date is shown in the horizontal axis, altitude in the vertical axis, and differential cosmic noise absorption as a color-coded surface. Note that the plotted data start from 00 UT 6 July 2002.

which is a valid assumption below approximately 120-km altitude. Concentrations of He were not available from the model output; however, the electron collision frequency with He is approximately 5 orders of magnitude smaller than that of the dominant species at 50- to 90-km altitude, based on our test calculations using He concentrations from the MSISE-E-90 model (for a MSIS description, see Hedin, 1991). The differential absorption was integrated with respect to altitude to get the total absorption of the atmospheric column. Differential absorption as a function of altitude and time in SOD and LYR during the 7 July 2002 SPE (event 43, max 22 pfu) is shown in Figure 2 as an example. Panel (a) of the figure shows differential absorption in SOD, and panel (b) in LYR. A weak event was chosen as an example to show the differential absorptions from multiple ionization sources, as the SPE ionization dominates in stronger events. At SOD (panel a), CNA due to auroral electrons and EUV radiation is visible at altitudes above approximately 90 km. Auroral CNA is centered around approximately each midnight, and EUV CNA is centered around approximately each midday. At LYR (panel b), EUV is the dominant source of CNA above 90-km altitude. CNA due to radiation belt electrons is visible in the altitude range 60 to 90 km as the dominant source of CNA in SOD during this weak SPE event. CNA due to the SPE is clearly visible in LYR in the altitude range of 55 to 80 km starting abruptly from approximately midday of 7 July. The SPE is also visible in SOD, but not as clearly due to the CNA caused by radiation belt electrons. The ionization rates due to the SPE in LYR and SOD are identical, as the model SPE input is applied uniformly to geomagnetic latitudes over 60°.

Model CNA for each riometer station was calculated separately at the closest grid point to the station's location with 30-MHz operating frequency. The wide-beam riometers' CNA was calculated as a wide-beam, and the imaging riometers' CNA as zenithal CNA. For the wide-beam riometers, the modeled zenithal CNA were multiplied by a scaling factor of 1.2 in the calculations to get equivalent wide-beam CNA (Hargreaves et al., 1987).

4. Results

The median observed and modeled CNA during the 62 SPEs were compared as a function of solar zenith angle and geomagnetic latitude. The field of view of each riometer in the *D* region was assumed to be ±0.5° in geomagnetic latitude for the comparison, which corresponds approximately to the area seen by a 60° wide-beam riometer at 90-km altitude (calculated to be ±0.46° geomagnetic latitude). The observational and model CNA data from all available SPEs were binned into 5° solar zenith angle bins for each station, and the median value of the bin was calculated. Data were limited to time periods where the GOES I3 integral proton flux is greater than or equal to 10 pfu and observational data are available. In case of overlapping riometer fields of view, the overlapping bins were averaged together. At any latitude bin with both GO-Canada and European chain riometer data, only one chain is used in the median value calculations by simply removing the other, which then favors either the European chain (case 1) or GO-Canada (case 2). In case 1, GIL and

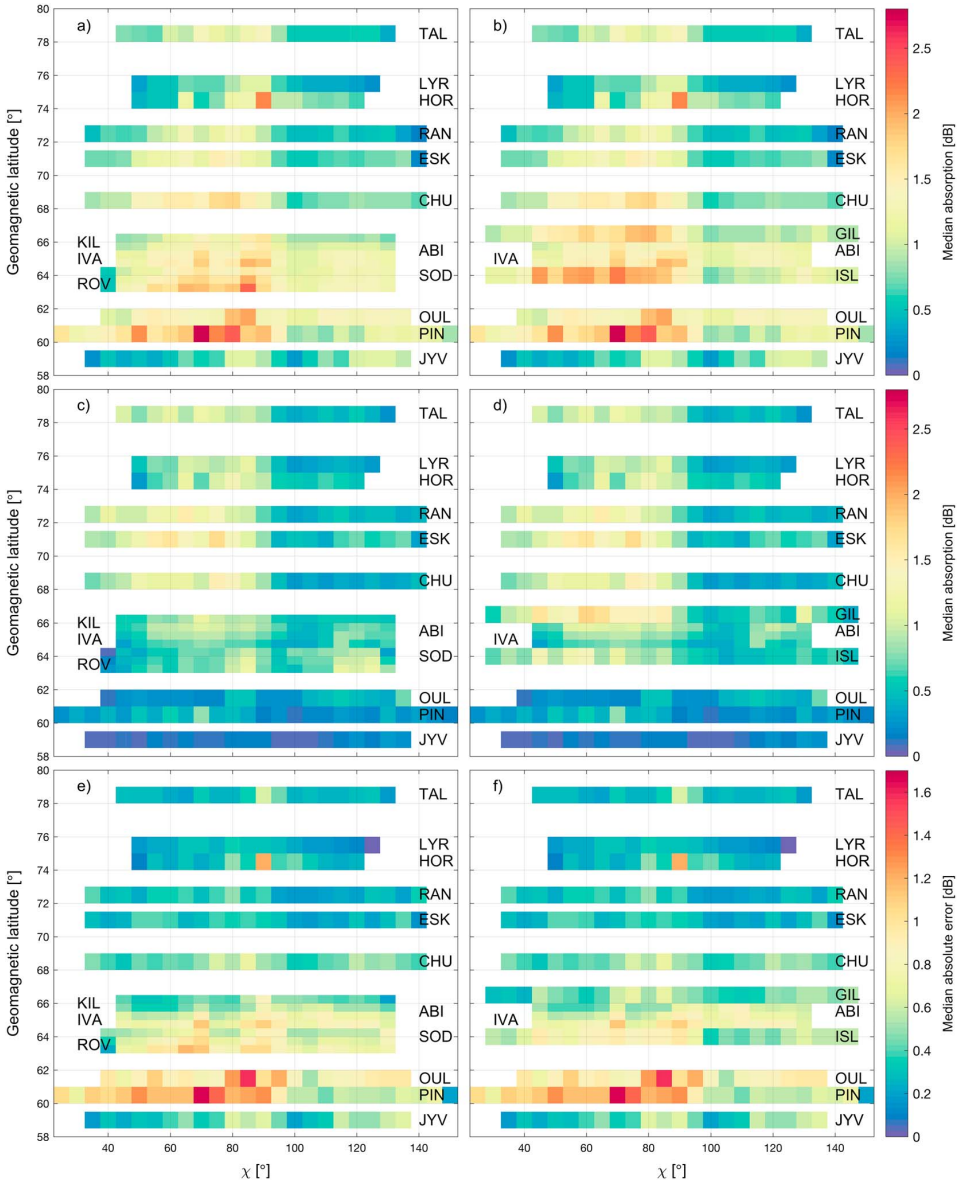

Figure 3. Modeled and observed median absorptions during solar proton events, and the median absolute errors between the model and the observations as a function of solar zenith angle, χ, and geomagnetic latitude. Panels in the left column are for case 1 (overlapping GO-Canada stations removed) and panels in the right column are for case 2 (overlapping European sector stations removed). Panels (a) and (b) are modeled median absorptions, panels (c) and (d) are observed median absorptions, and panels (e) and (f) are the median absolute errors between the model and the observations. Note that the color scaling in the last row is different from the first two rows.

ISL were removed, and in case 2, KIL, SOD, and ROV were removed. This approach was chosen due to the difference in observed CNA between the two riometer chains, which is due to the removal of the corrupted winter events from the SGO data and the different QDC methods. Model median absorption and observed median absorption for case 1 during the SPEs as a function of geomagnetic latitude and solar zenith angle are shown in Figures 3a and 3c. Model median absorption and observed median absorption for case 2 during the SPEs as a function of geomagnetic latitude and solar zenith angle are shown in Figures 3b and 3d, and the median absolute errors between the modeled and observed absorptions for both cases are shown in

Table 3
Mean Differences Between the Model and the Observed Median CNA at Each Riometer Station, and the Nonlinearity Correction Parameter R and Its 95% Confidence Intervals

Station	Sunlit[a](dB)	Twilight[b](dB)	Dark[c](dB)	*R*	95% CI
TAL	0.06	0.45	0.18	4.02	3.69/4.40
LYR	−0.24	0.14	0.07		
HOR	0.06	0.62	0.29	1.88	1.72/2.05
RAN	−0.16	0.22	0.09	11.93	9.51/14.85
ESK	−0.16	0.24	0.14	17.84	14.39/21.67
CHU	0.25	0.50	0.43	4.19	3.53/4.97
GIL	0.23	0.47	0.38	4.25	3.65/4.95
KIL	0.29	0.59	0.36		
ABI	0.34	0.59	0.49	7.77	4.76/18.16
IVA	0.78	1.00	0.76	1.98	1.72/2.31
ISL	0.75	0.70	0.44	3.71	3.02/4.65
SOD	0.63	0.74	0.52	2.00	1.74/2.35
ROV	0.79	0.85	0.59	9.88	5.61/21.02
OUL	0.93	1.25	0.82		
PIN	1.06	1.02	0.45		
JYV	0.31	0.41	0.39		

Note. CNA = cosmic noise absorption; CI = confidence interval.
[a]Sunlit $\chi < 82.5°$. [b]Twilight $82.5° < \chi < 97.5°$. [c]Dark $\chi > 97.5°$.

Figures 3e and 3f, respectively. Bins with less than or equal to 10 data points were removed in each of the panels. The number of data points in the remaining bins varies between 15 and 268 from the extreme solar zenith angles to the most common solar zenith angles.

The median absolute errors between the model and the observations are very similar at the five stations (TAL-ESK) poleward of 70° geomagnetic latitude. The model underestimates the CNA slightly as compared to the observations in the sunlit atmosphere and overestimates it in the twilight transition. CNA in the dark atmosphere is overestimated slightly by the model as compared to the observations. The differences and median absolute errors are generally small (≤0.5 dB) poleward of 70° geomagnetic latitude. The mean values of the differences between the model and the observations during sunlit ($\chi < 82.5°$), twilight ($82.5° < \chi < 97.5°$), and dark conditions ($\chi > 97.5°$) for all 16 stations are listed in Table 3. The absorption decrease due to the twilight transition is at larger zenith angles in the model than in the observations, which can be seen as increased difference between the model and the observations in twilight conditions and as increased median absolute errors in the zenith angle bin centered at $\chi = 90°$ in Figures 3e and 3f. The two GO-Canada stations between 66° and 69° geomagnetic latitude (CHU and GIL) show larger differences and median absolute errors between the model and the observations than the poleward stations. Unlike at the stations poleward of 70° geomagnetic latitude, the sunlit values are generally overestimated by the model. CNA in the dark atmosphere and during twilight conditions is overestimated by the model at these two stations. The difference between the model and the observations at the European chain stations KIL-ROV is systematically larger than the difference at the poleward stations and GIL. The overestimation of CNA by the model compared to the observations increases with decreasing geomagnetic latitude. The results from the stations equatorward of approximately 66° geomagnetic latitude indicate that protons precipitating into these geomagnetic latitudes are subject to varying levels of geomagnetic cutoff, which is not represented in the simulations, and that the MEE ionization is overestimated in the model. The effect of geomagnetic cutoff is especially evident at OUL and PIN, where CNA is overestimated by the model at all zenith angles. The overestimation of MEE ionization is, in conjunction with the geomagnetic cutoff effect, responsible for the overestimation of CNA at geomagnetic latitudes between about 63° and 66°. The modeled and observed median absorptions in JYV are low, as the latitude limit for proton precipitation in the model is set at 60° geomagnetic latitude and only very high energy (about >100 MeV; Rodger et al., 2006, Figure 8) protons can precipitate into the atmosphere above JYV in the observed data.

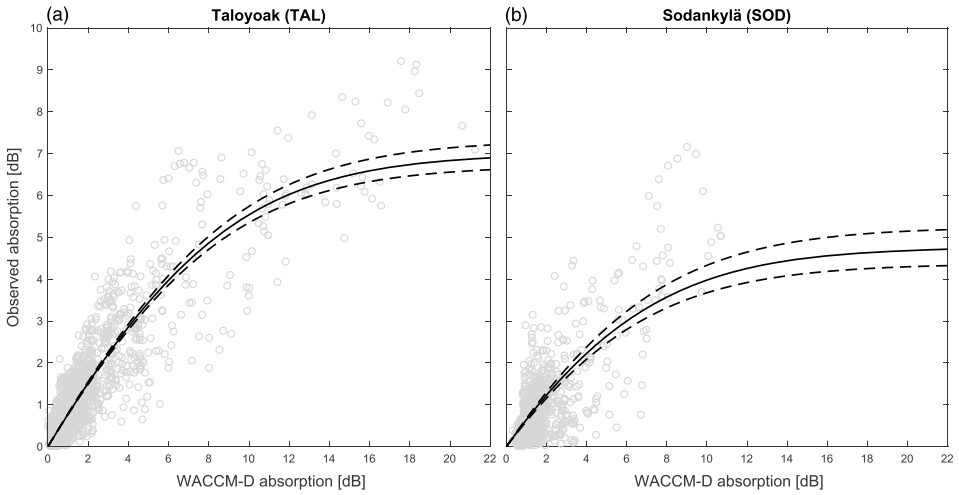

Figure 4. Modeled and observed absorptions from (a) TAL and (b) SOD riometers with fitted nonlinear response curves, equation (5), and their 95% bootstrap confidence intervals. Individual data points shown as gray circles, best fits to data as solid lines, and confidence intervals as dashed lines. WACCM-D = Whole Atmosphere Community Climate Model with added *D* region ion chemistry.

The relationship between the observed and modeled CNA during the SPEs was studied by plotting the 1-hr data points during the SPEs as scatter plots for each station. Scatter plots for TAL (panel a) and SOD (panel b) are shown as an example in Figure 4. The observed and modeled CNA values at TAL agree well and are linear to approximately 6 dB, with an intercept at the origin. At higher model CNA values, the relationship between the observed and modeled CNA becomes nonlinear, and the model shows higher values than the observations. The TAL scatter plot was chosen as an example of best-case nonlinear agreement between the observed and modeled CNA of the wide-beam riometers. Compared to the TAL scatter plot, the SOD scatter plot shows a worst-case agreement between observed and modeled values. The modeled CNA values are offset from zero by approximately 0.5 dB when the observed CNA values are at zero. A similar offset is visible in IVA, and to a lesser extent in ROV, GIL, ABI, and HOR (not shown). Compared to TAL, the observed CNA values at SOD vary more with modeled values between 1 and 2 dB, and the linear and nonlinear relationships are more difficult to discern. Increased variation in observed CNA values at modeled values of approximately 1 to 2 dB is also visible in ROV, IVA, ISL, GIL, and ABI. The observed absorptions from LYR and KIL imaging riometers are linear with model absorption (not shown) with separate populations for sunlit and dark atmospheric conditions. The slopes for LYR and KIL in sunlit conditions are 1.30 and 1.00, and in dark conditions 0.71 and 0.61.

As the southernmost stations are heavily affected by geomagnetic cutoffs and the simulations do not consider the effect of geomagnetic cutoff poleward of 60° geomagnetic latitude, the data from JYV, PIN, and OUL were removed from the comparison. As shown in the example scatter plots of Figure 4, the response of the wide-beam riometers becomes nonlinear with large modeled absorption values. All analyzed wide-beam riometers have a nonlinear response to large modeled CNA, but the dependence between the observed and modeled values varies from station to station. A possible correction method for the nonlinear response is presented here.

During normal conditions of low ionospheric absorption, the noise power available to a riometer is determined by the radio noise temperature of the sky with negligible contributions from the absorbing region of the ionosphere and losses in the receiving instrumentation (Little & Leinbach, 1958). As the absorption of the ionosphere increases to large values (greater than 10 dB; Browne et al., 1995), these normally negligible effects become significant. At large absorption values, the riometer receives additional significant signals from the absorbing ionosphere (Hargreaves & Detrick, 2002) and the lossy hardware causing the riometer response to become nonlinear. The signal, P, measured by a riometer is

$$P = G(a \cdot T_s + T_r), \tag{1}$$

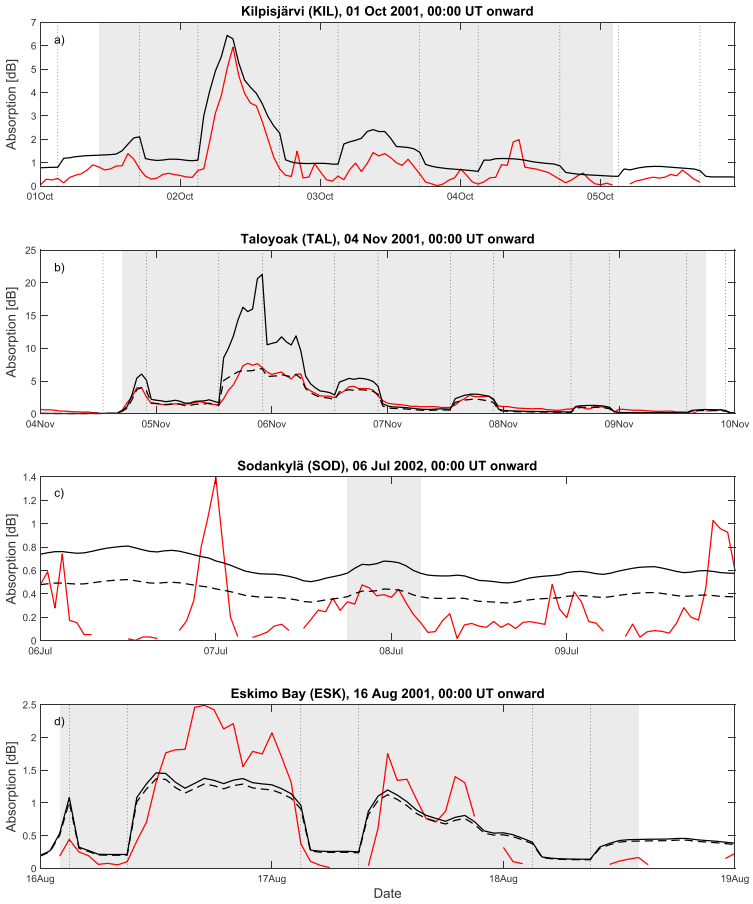

Figure 5. Examples of modeled and observed cosmic noise absorption (CNA) during four solar proton events at (a–d) four different stations. Solid black lines are modeled CNA values, dashed black lines are modeled CNA values with the nonlinear response correction applied, and the solid red lines are observations. Note that panel (a) does not have a nonlinear response corrected line (black dashed line). The gray shaded areas indicate time periods where the GOES >10-MeV integral flux is greater than or equal to 10 pfu, and the dotted vertical lines are the approximate times where the solar zenith angle is 97°.

where G is the gain of the instrument, a is absorption as a linear value in range $[0, 1]$, T_s is the wanted sky noise measured by the instrument, and T_r is unwanted noise from other sources. Absorption, A, is given in data as decibels compared to a quiet day marked by subscript q. Absorption is therefore given by

$$A = 10 \cdot \log_{10}\left(\frac{P_q}{P}\right) = 10 \cdot \log_{10}\left(\frac{a_q \cdot T_s + T_r}{a \cdot T_s + T_r}\right). \tag{2}$$

The ratio between the wanted and unwanted noise is

$$R = \frac{T_s}{T_r}. \tag{3}$$

Assuming that the quiet day absorption is small ($a_q = 1$),

$$A = 10 \cdot \log_{10}\left(\frac{1 + 1/R}{a + 1/R}\right), \tag{4}$$

where $a = 10^{-A_s/10}$ and A_s is the true absorption of the ionosphere in decibels. As R increases, the absorption, A, approaches the true absorption of the ionosphere A_s:

$$R \to \infty \Rightarrow A \to A_s.$$

The dependence between observed absorption and the true absorption of the ionosphere can be written as

$$A = 10 \cdot \log_{10}\left(\frac{1 + 1/R}{10^{-A_s/10} + 1/R}\right). \quad (5)$$

Assuming that the modeled WACCM-D absorption is the true absorption of the ionosphere, the presented dependence can be used to determine the ratio between wanted and unwanted noise in the riometer, which can be used to convert between observed absorption values and true absorption values. The correction function, equation (5), was fitted to each station separately with WACCM-D absorption as the true absorption and R as a free parameter. A nonlinear least squares method was used in the fitting. The fitted function for TAL and SOD, and the 95% bootstrap confidence intervals, are shown in the scatter plots of Figure 4. Ten thousand bootstrap samples were used for the confidence interval determination. The R values and their 95% bootstrap confidence intervals for each analyzed wide-beam riometer are listed in Table 3.

Modeled and observed absorptions were plotted as time series, separately for each station and event, to study the performance of WACCM-D in reproducing the temporal evolution of ionospheric absorption in individual events. Four individual events are shown as examples in Figure 5. Solid black lines are modeled CNA values, dashed black lines are modeled CNA values with the nonlinear response correction applied, and the solid red lines are observations. The time periods where the GOES >10-MeV integral flux is greater than or equal to 10 pfu have been shaded and the approximate times of the model twilight change ($\chi = 97°$) are marked with dotted vertical lines. Panel (a) shows event 26 (max 2,360 pfu) from KIL, where the magnitude of the CNA is overestimated throughout the event by the model up to approximately 1 dB, but the time behavior corresponds very well with the observations. Note that the nonlinear response correction is not applied in the top panel, as the response was linear for both of the imaging riometers (KIL and LYR). Panel (b) shows an extreme event (event 28, max 31,700 pfu) from TAL with the best-case nonlinear response correction. The modeled CNA reaches a maximum value of approximately 21 dB with an observed maximum value of approximately 7.5 dB. The modeled CNA corrected for the nonlinear response of the riometer agrees very well with the observed CNA. The observed sunrise increase in CNA is more gradual than the abrupt increase in the modeled CNA, especially on 5 November. A weak event (event 43, max 22 pfu) with auroral activity from the SOD riometer is shown in panel (c). The same event at SOD is shown in Figure 2a. A small increase in CNA is seen during the short SPE in both observations and model data. Outside the SPE, the observed CNA peaks around midnight between 6 and 7 July, and the evening of 9 July, are caused by auroral activity. The auroral activity is not well reproduced, as the model ionization for auroral electrons (Kp parametrization) produces a uniform ionization band at the auroral oval latitudes that cannot capture local variations (e.g., substorm activity) properly. Unlike the SPE ionization input, the auroral electron parametrization is based on magnetic field variations rather than direct particle measurements. The higher than observed CNA in the model due to the radiation belt electron input is visible through the plot. In 18 of the studied events, the observed CNA was found to be higher than the modeled CNA in three or more stations during sunlit conditions. These cases are only present at stations poleward of 66° geomagnetic latitude. One such event (event 24, max 493 pfu) from ESK is shown in Figure 5d. In this example event, CNA in sunlit conditions is underestimated by the model up to approximately 1.1 dB, and CNA in dark conditions is overestimated by the model up to 0.25 dB. As in Figure 5b, the sunrise increase in CNA is more abrupt in the model than in the observations. In addition to the model sunrise increase of CNA being more abrupt, the sunset decrease in CNA is also more abrupt in the model than in the observations. Variations in the model CNA for the example events of Figure 5 were estimated by calculating the mean absolute error of the CNA at the station's grid point and the adjacent grid points (nine grid points in total) at each time step. The mean absolute errors were less than 0.08 dB at all time time steps discarding the points closest to the model's twilight transition. Next to the twilight transition, where the adjacent grid point is on the other side of the twilight transition, the maximum error in the example events was 0.95 dB in the extreme event shown in Figure 5b.

5. Discussion

WACCM-D can model CNA well in the polar cap, both in sunlit and dark conditions. The twilight transition of CNA is not modeled as well as the sunlit or dark conditions. The modeled median CNA values at twilight conditions are higher than in the observations, which indicates that the increase in CNA during sunrise is more abrupt in the model than in observations and that the sunset decrease of CNA is delayed compared to observations. These differences in sunrise and sunset behavior are also visible in Figures 5a,

5b, and 5d. The twilight difference between the model and the observations is likely due to the night/day scaling in WACCM-D, which is a simple on/off at the solar terminator in the *D* region at $\chi = 97°$ (Verronen et al., 2016), that is, an Earth shadow method. In reality, electron depletion starts during sunset when the whole mesosphere is still sunlit (Collis & Rietveld, 1990), and the rise in CNA can be delayed at sunrise by a screening of solar ultraviolet radiation by the stratospheric ozone layer and the slowly developing chemical changes in the *D* region (for a review, see; Rogers et al., 2016, and references therein). Similar twilight difference results were presented by Rogers et al. (2016), who concluded that using the Earth shadow method in full-profile CNA models will fail to represent the slowly varying ionospheric composition and temperature changes affecting CNA at presunset and especially postsunrise conditions.

Cutoff latitudes are not static but move in latitude with changing conditions of the magnetosphere and the solar wind from event to event, and even within events (Nesse Tyssøy & Stadsnes, 2015), producing a gradual effect in the averaged data. The gradual effect of the geomagnetic cutoffs on observed CNA is visible in Figure 3 and Table 3 at stations equatorward of approximately 66° geomagnetic latitude. The effect is strongest in the stations between 60° and 62° (OUL and PIN), where the energetic protons responsible for the majority of the CNA are almost completely cutoff in the observations on average. The decrease in observed median CNA, increasing differences between the model and the observations, and increasing median absolute errors, especially during sunlit conditions, with decreasing geomagnetic latitude between 66° and 63° indicate that increasing amounts of protons responsible for CNA are cutoff in the averaged data. During suitable conditions, lower-energy protons can access lower latitudes and push the average main cutoff effect equatorward. When limiting data to events with a maximum flux greater than 1,000 pfu, the main cutoff effect in the averaged data seems to be pushed to about 61° geomagnetic latitude. This agrees with the results by Rodger et al. (2006) in that the larger geomagnetic disturbances associated with large SPEs increase the impact area of SPE particles. In addition to moving in latitude with varying magnetospheric and solar wind conditions, cutoff latitudes have been shown to have day-night asymmetry (Nesse Tyssøy et al., 2013; Nesse Tyssøy & Stadsnes, 2015), which is not taken into account by the static cutoff latitude of the model.

The commonly used (e.g., Jackman et al., 2009; Matthes et al., 2017) 60° lower geomagnetic latitude limit for uniform SPE proton precipitation and ionization overestimates the spatial extent of the SPE effect. The importance of implementing improved geomagnetic cutoff constraints for solar proton precipitation in chemistry climate models depends on the desired accuracy of the model results, the timescale of the model studies, and the aggregated impact of SPEs on the chemistry of the middle atmosphere compared to other ionization sources. Even though SPEs cause large-scale ionization and chemical changes in the middle atmosphere, they occur rarely compared to the precipitation of high-energy electrons from the radiation belts during geomagnetically active periods or during substorms. The chemical effect of radiation belt electrons during a single large geomagnetic storm on the neutral atmosphere was modeled by Rodger et al. (2010) with the SIC model. They reported mesospheric O_3 changes that are fairly similar in magnitude, timescales, and altitude to those presented in previous model and experimental observation studies for large SPEs. Seppälä et al. (2015) modeled a 5-day period with 61 substorms using the SIC model resulting in mesospheric O_3 changes that are similar in scale to a small to medium SPE. Compared to energetic electron precipitation effects on the neutral atmosphere, SPEs affect the whole polar cap area and ionize the atmosphere to lower altitudes. At least some of the outer radiation belt electrons precipitate outside the polar vortex, leading to less NO_x transport during the polar winter than in SPEs and making the direct contrasting of energetic electron precipitation and SPE effects more difficult (Rodger et al., 2010).

The modeled CNA is overestimated compared to observations in the auroral and subauroral latitudes as seen in Figures 3 and 4b. The overestimation is in part due to the 60° cutoff latitude and in part due to the overestimation of MEE ionization. The used MEE model does not have an MLT dependence, so a daily zonal mean MEE flux is applied uniformly to all MLTs. The use of daily zonal mean forcing results in overestimation of MEE fluxes on the dayside and underestimation on the nightside. Like the auroral electron ionization input, the MEE model is statistical and is not able to reproduce local variations in MEE precipitation. The effective recombination coefficient is smaller in the sunlit *D* region than in the dark *D* region (Hargreaves & Birch, 2005), resulting in larger CNA in sunlit conditions for the same ionization forcing. Therefore, overestimation in the MEE forcing will cause a larger increase in model CNA in the sunlit atmosphere than in the dark atmosphere, as seen from the model results. An additional reason for the overestimation of CNA by the model in the sunlit *D* region can be solar radio emission, which will cause reduced observed absorption (Kavanagh et al., 2004), especially when the Sun is in the riometer beam or in the beam side lobes. The

WACCM-D model also overestimates CNA in the dark atmosphere at auroral and subauroral latitudes, but the differences between the model and the observations are smaller. The used MEE model has been recently refined by van de Kamp et al. (2018) with improved consideration for low electron fluxes and an option to include MLT dependence with 3-hr temporal resolution. The performance of WACCM-D with the refined MEE model with MLT dependence should be investigated in the future.

The nonlinear response of riometers to large levels of absorption is a known phenomenon in the field but rarely discussed in publications. The hardware in riometer systems has been designed and configured in different ways resulting in different upper limits for the linear response. The nonlinear response correction presented in this paper works well for some of the used riometers but is sensitive to data selection. Special care has to be taken during the selection of data for the method, as the uncertainties in fitting of the R parameter can become large as shown by the 95% bootstrap confidence intervals listed in Table 3. The poor fit in some of the stations is due to the variation in observed CNA values due to substorms, geomagnetic storms, and geomagnetic cutoff; variation in modeled CNA values due to the MEE model's zonal mean input; and the different atmospheric conditions in the sunlit and dark atmosphere. Based on a cursory examination, and the fact that the largest CNA values occur in the sunlit atmosphere, data should possibly be limited to sunlit conditions when determining the nonlinearity of a riometer with this method. When data are limited to sunlit conditions, the values of the R parameter become close to or higher than the upper limits of the 95% bootstrap confidence intervals. Further testing of the nonlinear correction method falls outside the scope of this paper, but the presented results should provide a good starting point for future work on the subject.

No explanation was found for the situations where the dayside observed CNA is higher than the modeled CNA in multiple stations as seen, for example, at ESK in Figure 5d. The higher observed CNA indicates either that the model is underestimating some ionization source or that some other phenomenon causing ionization is lacking from the model in these cases. The difference in CNA between the model and the observations was contrasted with geomagnetic activity (Kp index), integral flux in the different GOES proton channels, season, and cases where multiple SPEs occur consecutively, but no explanation was found for the underestimated model CNA. The electron density output of the model was increased as a test for the example event and location shown in Figure 5d. An increase in electron density by a factor of 1.5 to 1.75 produced approximately the correct level of CNA but did not affect the time behavior of the model. As the stations where this underestimation occurs are poleward of about 66° geomagnetic latitude; a possible explanation is that the SPE proton precipitation is underestimated in the model. This would not explain however why the underestimation is not visible in all or most events. It is also possible that the underestimation happens at all latitudes in the model, but that the MEE precipitation and geomagnetic cutoff effects mask it from stations equatorward of about 66° geomagnetic latitude.

6. Conclusions

We have studied the spatial and temporal extent of CNA during 62 SPEs from 2000 to 2005 using the WACCM-D model and observations from 16 riometer stations. Observed and modeled CNA were contrasted as a function of solar zenith angle and geomagnetic latitude statistically, for each station statistically, and as time series for each event and station individually. We summarize the results of this study as follows:

1. WACCM-D can reproduce the observed CNA well poleward of about 66° geomagnetic latitude with an average absolute difference between the model and the observations of less than 0.5 dB varying with solar zenith angle and station.
2. Equatorward of approximately 66° geomagnetic latitude, the average difference between the model and the observation increases with decreasing geomagnetic latitude from about 0.5 to 1 dB due to the daily zonal mean MEE forcing and the uniform proton forcing poleward of 60° geomagnetic latitude.
3. Due to the Earth shadow implementation of the change between night and day in WACCM-D, the CNA increase (decrease) during sunrise (sunset) is more abrupt and at greater solar zenith angle values in WACCM-D than what is observed, resulting in overestimation of CNA during twilight conditions.
4. Observed CNA in sunlit conditions is underestimated by WACCM-D at three or more stations poleward of 66° geomagnetic latitude in 18 events, in contrast with WACCM-D usually overestimating the observed CNA. More investigations are required to explain the underestimation of CNA in sunlit conditions by WACCM-D for this subset of events.

Table A1
Solar Proton Events Used in This Study

Event	SPE start time (UT)	SPE max time (UT)	Max >10-MeV flux (pfu)
1[a]	18 Feb 2000 11:30	18 Feb 12:15	13
2	04 Apr 2000 20:55	05 Apr 09:30	55
3	07 Jun 2000 13:35	08 Jun 09:40	55
4	10 Jun 2000 18:05	10 Jun 20:45	46
5	14 Jul 2000 10:45	15 Jul 12:30	24,000
6	22 Jul 2000 13:20	22 Jul 14:05	17
7	28 Jul 2000 10:50	28 Jul 11:30	18
8	11 Aug 2000 16:50	11 Aug 16:55	17
9	12 Sep 2000 15:55	13 Sep 03:40	320
10[a]	16 Oct 2000 11:25	16 Oct 18:40	15
11[a]	26 Oct 2000 00:40	26 Oct 03:40	15
12[a]	08 Nov 2000 23:50	09 Nov 16:00	14,800
13[a]	24 Nov 2000 15:20	26 Nov 20:30	942
14[a]	28 Jan 2001 20:25	29 Jan 06:55	49
15[a]	29 Mar 2001 16:35	30 Mar 06:10	35
16[a]	02 Apr 2001 23:40	03 Apr 07:45	1,110
17[a]	10 Apr 2001 08:50	11 Apr 20:55	355
18[a]	15 Apr 2001 14:10	15 Apr 19:20	951
19[a]	18 Apr 2001 03:15	18 Apr 10:45	321
20[a]	28 Apr 2001 04:30	28 Apr 05:00	57
21	07 May 2001 19:15	08 May 07:55	30
22	15 Jun 2001 17:50	16 Jun 00:05	26
23	10 Aug 2001 10:20	10 Aug 11:55	17
24	16 Aug 2001 01:35	16 Aug 03:55	493
25	24 Sep 2001 12:15	25 Sep 22:35	12,900
26	01 Oct 2001 11:45	02 Oct 08:10	2,360
27[a]	19 Oct 2001 22:25	19 Oct 22:35	11
28[a]	04 Nov 2001 17:05	06 Nov 02:15	31,700
29[a]	19 Nov 2001 12:30	20 Nov 00:10	34
30[a]	22 Nov 2001 23:20	24 Nov 05:55	18,900
31[a]	26 Dec 2001 06:05	26 Dec 11:15	779

Note. SPE = solar proton event.
[a]SGO stations affected by unknown radio interference.

5. The absorption response of the used wide-beam riometers becomes nonlinear at large absorption values. A correction method for this nonlinearity was presented with the goal of providing a starting point for further studies on the subject.
6. The used 60° stationary cutoff latitude for proton precipitation in WACCM-D was found to overestimate the spatial extent of CNA during SPEs by about 2° to 3° geomagnetic latitude on average. The overestimation of the average spatial extent seems to decrease to about 1° geomagnetic latitude when data are limited to events with a maximum flux greater than 1,000 pfu. A more realistic cutoff model should be implemented into the proton precipitation forcing in the future, if more accurate performance is required from the model.

Although the overall performance of WACCM-D in reproducing CNA is good, some tests and improvements are recommended for the future. The results presented here should be compared with comparison runs of the WACCM-D model with improved proton cutoff constraints and MLT-dependent MEE fluxes.

Table A2
Solar Proton Events Used in This Study

Event	SPE start time (UT)	SPE max time (UT)	Max >10-MeV flux (pfu)
32[a]	29 Dec 2001 05:10	29 Dec 08:15	76
33[a]	30 Dec 2001 02:45	31 Dec 16:20	108
34[a]	10 Jan 2002 20:45	11 Jan 05:30	91
35[a]	15 Jan 2002 14:35	15 Jan 20:00	15
36[a]	17 Mar 2002 08:20	17 Mar 08:50	13
37	18 Mar 2002 13:00	19 Mar 06:50	53
38[a]	20 Mar 2002 15:10	20 Mar 15:25	19
39[a]	22 Mar 2002 20:20	23 Mar 13:20	16
40	17 Apr 2002 15:30	17 Apr 15:40	24
41	21 Apr 2002 02:25	21 Apr 23:20	2,520
42	22 May 2002 17:55	23 May 10:55	820
43	07 Jul 2002 18:30	07 Jul 19:55	22
44	16 Jul 2002 17:50	17 Jul 16:00	234
45	19 Jul 2002 10:50	19 Jul 15:15	13
46	22 Jul 2002 06:55	23 Jul 10:25	28
47	14 Aug 2002 09:00	14 Aug 16:20	26
48	22 Aug 2002 04:40	22 Aug 09:40	36
49	24 Aug 2002 01:40	24 Aug 08:35	317
50	07 Sep 2002 04:40	07 Sep 16:50	208
51	09 Nov 2002 19:20	10 Nov 05:40	404
52	04 Nov 2003 22:25	05 Nov 06:00	353
53[a]	21 Nov 2003 23:55	22 Nov 02:30	13
54[a]	02 Dec 2003 15:05	02 Dec 17:30	86
55	25 Jul 2004 18:55	26 Jul 22:50	2,086
56	01 Nov 2004 06:55	01 Nov 08:05	63
57	07 Nov 2004 19:10	08 Nov 01:15	495
58	16 Jan 2005 02:10	17 Jan 17:50	5,040
59	14 May 2005 05:25	15 May 02:40	3,140
60	14 Jul 2005 02:45	15 Jul 03:45	134
61	27 Jul 2005 23:00	29 Jul 17:15	41
62	22 Aug 2005 20:40	23 Aug 10:45	330

Note. Continued from previous table.
[a]SGO stations affected by unknown radio interference.

Appendix A: List of Studied Solar Proton Events

Acknowledgments
The work of E. H., P. T. V., and N. K. was supported by the Academy of Finland through the project 276926 (SECTIC: Sun-Earth Connection Through Ion Chemistry). This work of A. K. is a part of the Tenure Track Project in Radio Science at Sodankylä Geophysical Observatory. This work of N. P. was supported by the Research Council of Norway under CoE contract 223252. We acknowledge Peter Stauning from the Danish Meteorological Institute (Denmark) and Hisao Yamagishi from the National Institute of Polar Research (Japan) who provided the Longyearbyen imaging riometer data. The Kilpisjärvi riometer data originated from the Imaging Riometer for Ionospheric Studies (IRIS), operated by the Space Plasma Environment and Radio Science (SPEARS) group, Department of Physics, Lancaster University (UK) in collaboration with the Sodankylä Geophysical Observatory. The Sodankylä Geophysical Observatory riometer chain data were provided by Antti Kero and the Sodankylä Geophysical Observatory (Finland). The GO-Canada riometer array is operated by the University of Calgary with financial support from the Canadian Space Agency. All GO-Canada riometer data are openly available from `data.phys.ucalgary.ca`. NOAA GOES particle flux data are openly available online from `https://www.ngdc.noaa.gov/stp/satellite/goes/dataaccess.html`. The authors would also like to acknowledge the openly available jLab data analysis package for Matlab (Lilly, 2017), which was used for parts of the plotting in this paper.

References

Andersson, M. E., Verronen, P. T., Marsh, D. R., Päivärinta, S.-M., & Plane, J. M. C. (2016). WACCM-D—Improved modeling of nitric acid and active chlorine during energetic particle precipitation. *Journal of Geophysical Research: Atmospheres*, *121*, 10,328–10,341. https://doi.org/10.1002/2015JD024173

Andersson, M. E., Verronen, P. T., Rodger, C. J., Clilverd, M. A., & Seppälä, A. (2014). Missing driver in the Sun-Earth connection from energetic electron precipitation impacts mesospheric ozone. *Nature Communications*, *5*, 5197. https://doi.org/10.1038/ncomms6197

Banks, P. M., & Kockarts, G. (1973). *Aeronomy, vol. A*. New York: Elsevier. https://doi.org/10.1016/C2013-0-10328-5

Baumgaertner, A. J. G., Seppälä, A., Jöckel, P., & Clilverd, M. A. (2011). Geomagnetic activity related NO_x enhancements and polar surface air temperature variability in a chemistry climate model: modulation of the NAM index. *Atmospheric Chemistry and Physics*, *11*(9), 4521–4531. https://doi.org/10.5194/acp-11-4521-2011

Browne, S., Hargreaves, J., & Honary, B. (1995). An imaging riometer for ionospheric studies. *Electronics & Communication Engineering Journal*, *7*(5), 209–217. https://doi.org/10.1049/ecej:19950505

Clilverd, M. A., Rodger, C. J., Moffat-Griffin, T., & Verronen, P. T. (2007). Improved dynamic geomagnetic rigidity cutoff modeling: Testing predictive accuracy. *Journal of Geophysical Research*, *112*, A08302. https://doi.org/10.1029/2007JA012410

Collis, P. N., & Rietveld, M. T. (1990). Mesospheric observations with the EISCAT UHF radar during polar cap absorption events: 1. Electron densities and negative ions. *Annales Geophysicae*, *8*, 809–824.

Friedrich, M., Harrich, M., Torkar, K., & Stauning, P. (2002). Quantitative measurements with wide-beam riometers. *Journal of Atmospheric and Solar-Terrestrial Physics*, *64*(3), 359–365. https://doi.org/10.1016/S1364-6826(01)00108-0

Funke, B., López-Puertas, M., Stiller, G. P., & von Clarmann, T. (2014). Mesospheric and stratospheric NO_y produced by energetic particle precipitation during 2002–2012. *Journal of Geophysical Research: Atmospheres*, *119*, 4429–4446. https://doi.org/10.1002/2013JD021404

Gillett, N. P., & Thompson, D. W. J. (2003). Simulation of recent Southern Hemisphere climate change. *Science*, *302*(5643), 273–275. https://doi.org/10.1126/science.1087440

Hargreaves, J. K., & Birch, M. J. (2005). On the relations between proton influx and D-region electron densities during the polar-cap absorption event of 28–29 October 2003. *Annales Geophysicae*, *23*(10), 3267–3276. https://doi.org/10.5194/angeo-23-3267-2005

Hargreaves, J. K., & Detrick, D. L. (2002). Application of polar cap absorption events to the calibration of riometer systems. *Radio Science*, *37*(3), 1035. https://doi.org/10.1029/2001RS002465

Hargreaves, J., Ranta, H., Ranta, A., Turunen, E., & Turunen, T. (1987). Observations of the polar cap absorption event of February 1984 by the EISCAT incoherent scatter radar. *Planetary and Space Science*, *35*(7), 947–958. https://doi.org/10.1016/0032-0633(87)90072-9

Hedin, A. E. (1991). Extension of the MSIS Thermosphere Model into the middle and lower atmosphere. *Journal of Geophysical Research*, *96*(A2), 1159–1172. https://doi.org/10.1029/90JA02125

Jackman, C. H. (2013). Ionization rates for 1963–2012 from solar proton events, Retrieved from http://solarisheppa.geomar.de/solarisheppa/sites/default/files/data/SOLARIS_Jackman_SPEs.pdf

Jackman, C. H., DeLand, M. T., Labow, G. J., Fleming, E. L., Weisenstein, D. K., Ko, M. K., et al. (2005). The influence of the several very large solar proton events in years 2000–2003 on the neutral middle atmosphere. *Advances in Space Research*, *35*(3), 445–450. https://doi.org/10.1016/j.asr.2004.09.006

Jackman, C. H., Marsh, D. R., Kinnison, D. E., Mertens, C. J., & Fleming, E. L. (2016). Atmospheric changes caused by galactic cosmic rays over the period 1960–2010. *Atmospheric Chemistry and Physics*, *16*(9), 5853–5866. https://doi.org/10.5194/acp-16-5853-2016

Jackman, C. H., Marsh, D. R., Vitt, F. M., Garcia, R. R., Randall, C. E., Fleming, E. L., & Frith, S. M. (2009). Long-term middle atmospheric influence of very large solar proton events. *Journal of Geophysical Research*, *114*, D11304. https://doi.org/10.1029/2008JD011415

Kallenrode, M.-B. (2003). Current views on impulsive and gradual solar energetic particle events. *Journal of Physics G: Nuclear Physics*, *29*, 965–981. https://doi.org/10.1088/0954-3899/29/5/316

Kavanagh, A., Marple, S., Honary, F., McCrea, I., & Senior, A. (2004). On solar protons and polar cap absorption: Constraints on an empirical relationship. *Annales Geophysicae*, *22*, 1133–1147. https://doi.org/10.5194/angeo-22-1133-2004

Kunz, A., Pan, L. L., Konopka, P., Kinnison, D. E., & Tilmes, S. (2011). Chemical and dynamical discontinuity at the extratropical tropopause based on START08 and WACCM analyses. *Journal of Geophysical Research*, *116*, D24302. https://doi.org/10.1029/2011JD016686

Lilly, J. M. (2017). jLab: A data analysis package for Matlab, v. 1.6.5, Retrieved from http://www.jmlilly.net/jmlsoft.html

Little, C. G., & Leinbach, H. (1958). Some measurements of high-latitude ionospheric absorption using extraterrestrial radio waves. *Proceedings of the IRE*, *46*(1), 334–348. https://doi.org/10.1109/JRPROC.1958.286795

Little, C. G., & Leinbach, H. (1959). The Riometer—A device for the continuous measurement of ionospheric absorption. *Proceedings of the IRE*, *47*(2), 315–320. https://doi.org/10.1109/JRPROC.1959.287299

Marsh, D. R., Garcia, R. R., Kinnison, D. E., Boville, B. A., Sassi, F., Solomon, S. C., & Matthes, K. (2007). Modeling the whole atmosphere response to solar cycle changes in radiative and geomagnetic forcing. *Journal of Geophysical Research*, *112*, D23306. https://doi.org/10.1029/2006JD008306

Matthes, K., Funke, B., Andersson, M. E., Barnard, L., Beer, J., Charbonneau, P., et al. (2017). Solar forcing for CMIP6 (v3.2). *Geoscientific Model Development*, *10*(6), 2247–2302. https://doi.org/10.5194/gmd-10-2247-2017

Nesse Tyssøy, H., & Stadsnes, J. (2015). Cutoff latitude variation during solar proton events: Causes and consequences. *Journal of Geophysical Research: Space Physics*, *120*, 553–563. https://doi.org/10.1002/2014JA020508

Nesse Tyssøy, H., Stadsnes, J., Søraas, F., & Sørbø, M. (2013). Variations in cutoff latitude during the January 2012 solar proton event and implication for the distribution of particle energy deposition. *Geophysical Research Letters*, *40*, 4149–4153. https://doi.org/10.1002/grl.50815

Randall, C. E., Harvey, V. L., Manney, G. L., Orsolini, Y., Codrescu, M., Sioris, C., et al. (2005). Stratospheric effects of energetic particle precipitation in 2003–2004. *Geophysical Research Letters*, *32*, L05802. https://doi.org/10.1029/2004GL022003

Reames, D. V. (1999). Particle acceleration at the Sun and in the heliosphere. *Space Science Reviews*, *90*(3), 413–491. https://doi.org/10.1023/A:1005105831781

Rienecker, M. M., Suarez, M. J., Gelaro, R., Todling, R., Bacmeister, J., Liu, E., et al. (2011). MERRA: NASA's Modern-Era Retrospective Analysis for Research and Applications. *Journal of Climate*, *24*(14), 3624–3648. https://doi.org/10.1175/JCLI-D-11-00015.1

Rodger, C. J., Clilverd, M. A., Seppälä, A., Thomson, N. R., Gamble, R. J., Parrot, M., et al. (2010). Radiation belt electron precipitation due to geomagnetic storms: Significance to middle atmosphere ozone chemistry. *Journal of Geophysical Research*, *115*, A11320. https://doi.org/10.1029/2010JA015599

Rodger, C. J., Clilverd, M. A., Verronen, P. T., Ulich, T., Jarvis, M. J., & Turunen, E. (2006). Dynamic geomagnetic rigidity cutoff variations during a solar proton event. *Journal of Geophysical Research*, *111*, A04222. https://doi.org/10.1029/2005JA011395

Rogers, N. C., Kero, A., Honary, F., Verronen, P. T., Warrington, E. M., & Danskin, D. W. (2016). Improving the twilight model for polar cap absorption nowcasts. *Space Weather*, *14*, 950–972. https://doi.org/10.1002/2016SW001527

Rosenberg, T. J., Detrick, D. L., Venkatesan, D., & van Bavel, G. (1991). A comparative study of imaging and broad-beam riometer measurements: The effect of spatial structure on the frequency dependence of auroral absorption. *Journal of Geophysical Research*, *96*(A10), 17,793–17,803. https://doi.org/10.1029/91JA01827

Rostoker, G., Samson, J. C., Creutzberg, F., Hughes, T. J., McDiarmid, D. R., McNamara, A. G., et al. (1995). Canopus—A ground-based instrument array for remote sensing the high latitude ionosphere during the ISTP/GGS program. *Space Science Reviews*, *71*(1), 743–760. https://doi.org/10.1007/BF00751349

Sen, H. K., & Wyller, A. A. (1960). On the generalization of the Appleton-Hartree magnetoionic formulas. *Journal of Geophysical Research*, *65*(12), 3931–3950. https://doi.org/10.1029/JZ065i012p03931

Seppälä, A., Clilverd, M. A., Beharrell, M. J., Rodger, C. J., Verronen, P. T., Andersson, M. E., & Newnham, D. A. (2015). Substorm-induced energetic electron precipitation: Impact on atmospheric chemistry. *Geophysical Research Letters*, *42*, 8172–8176. https://doi.org/10.1002/2015GL065523

Seppälä, A., Randall, C. E., Clilverd, M. A., Rozanov, E., & Rodger, C. J. (2009). Geomagnetic activity and polar surface air temperature variability. *Journal of Geophysical Research*, *114*, A10312. https://doi.org/10.1029/2008JA014029

Seppälä, A., Verronen, P. T., Kyrölä, E., Hassinen, S., Backman, L., Hauchecorne, A., et al. (2004). Solar proton events of October–November 2003: Ozone depletion in the Northern Hemisphere polar winter as seen by GOMOS/Envisat. *Geophysical Research Letters*, *31*, L19107. https://doi.org/10.1029/2004GL021042

Sinnhuber, M., Nieder, H., & Wieters, N. (2012). Energetic particle precipitation and the chemistry of the mesosphere/lower thermosphere. *Surveys in Geophysics*, *33*(6), 1281–1334. https://doi.org/10.1007/s10712-012-9201-3

Smith-Johnsen, C., Marsh, D. R., Orsolini, Y., Nesse, H., Tyssøy, K., Hendrickx, M. I., et al. (2018). Nitric oxide response to the April 2010 electron precipitation event: Using WACCM and WACCM-D with and without medium energy electrons. *Journal of Geophysical Research: Space Physics*, *123*, 5232–5245. https://doi.org/10.1029/2018JA025418

Spanswick, E., Donovan, E., & Baker, G. (2005). Pc5 modulation of high energy electron precipitation: Particle interaction regions and scattering efficiency. *Annales Geophysicae*, *23*(5), 1533–1542. https://doi.org/10.5194/angeo-23-1533-2005

Stauning, P., & Hisao, Y. (1995). Imaging riometer installation in Longyearbyen, Svalbard. (Technical report 95-12). Copenhagen: Danish Meteorological Institute.

Vainio, R., Desorgher, L., Heynderickx, D., Storini, M., Flückiger, E., Horne, R. B., et al. (2009). Dynamics of the Earth's particle radiation environment. *Space Science Reviews*, *147*(3), 187–231. https://doi.org/10.1007/s11214-009-9496-7

van de Kamp, M., Rodger, C. J., Seppälä, A., Clilverd, M. A., & Verronen, P. T. (2018). An updated model providing long-term data sets of energetic electron precipitation, including zonal dependence. *Journal of Geophysical Research: Atmospheres*, *123*, 9891–9915. https://doi.org/10.1029/2017JD028253

van de Kamp, M., Seppälä, A., Clilverd, M. A., Rodger, C. J., Verronen, P. T., & Whittaker, I. C. (2016). A model providing long-term data sets of energetic electron precipitation during geomagnetic storms. *Journal of Geophysical Research: Atmospheres*, *121*, 12,520–12,540. https://doi.org/10.1002/2015JD024212

Verronen, P. T., Andersson, M. E., Marsh, D. R., Kovács, T., & Plane, J. M. C. (2016). WACCM-D—Whole Atmosphere Community Climate Model with D-region ion chemistry. *Journal of Advances in Modeling Earth Systems*, *8*, 954–975. https://doi.org/10.1002/2015MS000592

Verronen, P. T., & Lehmann, R. (2013). Analysis and parameterisation of ionic reactions affecting middle atmospheric HO_x and NO_y during solar proton events. *Annales Geophysicae*, *31*(5), 909–956. https://doi.org/10.5194/angeo-31-909-2013

Verronen, P. T., Ulich, T., Turunen, E., & Rodger, C. J. (2006). Sunset transition of negative charge in the D-region ionosphere during high-ionization conditions. *Annales Geophysicae*, *24*(1), 187–202. https://doi.org/10.5194/angeo-24-187-2006

PAPER III

Heino, E. and Partamies, N. (2019). Observational validation of cutoff models as boundaries of solar proton event impact area. *Submitted for publication in Journal of Geophysical Research: Space Physics.*